EXPERIMENTAL STUDY OF THE SUBSONIC AERODYNAMICS
OF A BLENDED WING BODY AIR VEHICLE
WITH A FOCUS ON RAPID TECHNOLOGY ASSESSMENT

THESIS

David A. Gebbie, Second Lieutenant, USAF

AFIT/GAE/ENY/05-M09

DEPARTMENT OF THE AIR FORCE
AIR UNIVERSITY

AIR FORCE INSTITUTE OF TECHNOLOGY

Wright-Patterson Air Force Base, Ohio

APPROVED FOR PUBLIC RELEASE; DISTRIBUTION UNLIMITED

AFIT/GAE/ENY/04-M09

EXPERIMENTAL STUDY OF THE SUBSONIC AERODYNAMICS
OF A BLENDED WING BODY AIR VEHICLE
WITH A FOCUS ON RAPID TECHNOLOGY ASSESSMENT

THESIS

Presented to the Faculty

Department of Aeronautics and Astronautics

Graduate School of Engineering and Management

Air Force Institute of Technology

Air University

Air Education and Training Command

In Partial Fulfillment of the Requirements for the

Degree of Master of Science in Aeronautical Engineering

David A. Gebbie, BSME

Second Lieutenant, USAF

March 2005

AFIT/GAE/ENY/04-M09

EXPERIMENTAL STUDY OF THE SUBSONIC AERODYNAMICS
OF A BLENDED WING BODY AIR VEHICLE
WITH A FOCUS ON RAPID TECHNOLOGY ASSESSMENT

David A. Gebbie, BS
Second Lieutenant, USAF

Approved:

_____   _____
Dr. Mark F. Reeder (Chairman)   Date

_____   _____
Dr. Ralph A. Anthenien, Jr. (Member)   Date

_____   _____
Eric J. Stephen, Lt Col, USAF (Member)   Date

AFIT/GAE/ENY/04-M09

Abstract

The subsonic aerodynamic performance of a blended wing body aircraft constructed using selective laser sintering was assessed in the AFIT low-speed wind tunnel. The scaled-down model of a strike tanker aircraft consisted of a shaped fuselage and sweptback wings. The Reynolds number, based on mean wing chord, during testing was on the order of 10^5 while the Mach number ranged from 0.10 to 0.20. The model evaluation and analysis process included force and moment measurements acquired from a wind tunnel balance, pressure data measured with 8 taps located on the model's upper surface, a comparison to computational fluid dynamics (CFD) solutions acquired in a parallel study conducted by AFRL/VAAC, and global pressure sensitive paint (PSP) measurements. Paint measurements were compared to pressure tap data to ensure their accuracy. Lift and drag coefficients, as well as pitching and rolling moments were examined to determine performance characteristics, including stability attributes and aircraft stall.

One of the most interesting results was the striking difference in the force and moment measurements before and after the paint was applied to the surface. The average surface roughness, Ra, was measured with a profilometer and was found to have increased from approximately 0.3μm to 0.7μm when the paint was applied. When traditional 2-D boundary layer approaches to assessing the effect of roughness, the 0.7μm value falls well below the threshold at which one would anticipate roughness to have any effect. There is support in archival literature for the notion that roughness effects are

iv

more pronounced in a 3-D boundary layer, and the pitching moment data and the PSP data indicate that the for the painted model, there is a gradual onset of wing stall marching inward from the wingtips toward the body. By contrast, the force and, in particular, the pitching moment data suggests that the onset of wing stall is sudden across the entire wing for the unpainted case. Interestingly, the CFD data compared well with the data corresponding to the measurements of the rougher, painted model. Notably, the grid used in CFD would require at least an order of magnitude higher resolution in the boundary layer region to accurately depict the submicron roughness effects.

To my parents for their love, support, and especially their patience.

Acknowledgments

  I would like to thank first and foremost the Air Vehicles Directorate of The Air Force Research Laboratory for providing the opportunity of this thesis study. I would also like to extend my gratitude to my thesis advisor, Dr. Mark Reeder, for his efforts in support of this thesis study. He provided a professional knowledge base and a number of research contributions that were essential to the success of the project. I would like to extend my appreciation to Dr. Jim Crafton as well, who was an integral part in the setup and overall completion of the PSP testing and post-processing. I thank Dr. Charles Tyler of the Air Vehicles directorate of AFRL for bringing this project to AFIT and for supporting a new Air Force Lieutenant in such a great project, and for his contribution to the results through his expertise in wind tunnel testing and CFD modeling. In addition, I would like to thank Dr. William Braisted of UDRI, for his part in the study of rapid prototyping, which led to the creation of the aircraft model. Last, I would like to thank Mr. Dwight Gehring for his patience and know-how in the operation of the AFIT Wind Tunnel and all its extremities. Without his help, this project would not have been possible, as he was always willing and ready to fire up the tunnel to take more data.

              David A. Gebbie

Table of Contents

List of Figures

List of Tables

EXPERIMENTAL STUDY OF THE SUBSONIC AERODYNAMICS

OF A BLENDED WING BODY AIR VEHICLE

WITH A FOCUS ON RAPID TECHNOLOGY ASSESSMENT

I. Introduction

Section 1 – Background

Due to the demand for higher performance, aircraft design and evaluation process has become far more time consuming than it was a few decades ago. This lengthy time requirement is a result of more sophisticated aircraft technology such as fly-by-wire systems, as well as increased safety standards and far more thorough flight testing. On the other hand, rapid design technology has emerged as a design tool which can drastically decrease the time required for the modeling and testing of aircraft. Aircraft evaluation has traditionally been carried out using test article fabrication, wind tunnel testing, and performance prediction for scaling purposes. Rapid design approaches are vital to the preliminary aircraft design process as they allow the industrial air framer to evaluate the structural and aerodynamic characteristics of the aircraft. Three rapid design tools which are critical for the evaluation of aerodynamics are: 1) rapid prototyping, 2) computational fluid dynamic (CFD) modeling, and 3) global measurements (27).

The first of these quickly advancing technologies, rapid prototyping, is a robust, accurate, and affordable method to support aerospace research and development. The rapid prototyping process allows for inexpensive models to be fabricated, most

commonly from plastic, in a matter of hours as opposed to days or weeks, with testing available almost immediately. This allows designers to continually study new concepts with a fast return on system performance verification. Having this capability early in the design process allows changes to be made without compromising scheduling and cost. The same solid model used in rapid prototyping may also be used as a starting point for CFD simulations and the experimental ground tests (28).

Numerically predictive methods such as CFD, the second of the aforementioned specific areas of technological advances, allow designers to predict the aerodynamic performance of an aircraft in many different scenarios before a scale model even enters the picture. However, the robustness of CFD is limited by the common problem of turbulence modeling and mesh resolution necessary for a practical solution. Although a model and wind tunnel testing is often required to verify the CFD results, testing requirements are generally decreased due to the relative ease of scaling the CFD predictions (27). Another attribute that gives CFD its popularity is its ability to predict parameters such as velocity, pressure, and even temperature globally about the test article. This is in contrast to traditional measurements which typically consist of forces and moments measured with a wind tunnel balance.

In turn, measuring design parameters globally is one of the most important advances in the field of modeling and testing. It allows the designer to visualize and quantify the flow around the entire surface of a vehicle in terms of velocity and pressure. Traditional measurement techniques such as using a balance to observe orthogonal force and moment data acting about a point within the model do not always allow for precise reasoning when inconsistencies occur between two data sets. Single-point methods such

as the inclusion of pressure taps in various locations on the model surface can resolve some of these issues by allowing the comparison of individual points to the CFD results. However, the application of pressure taps to a model requires additional diagnostics and generally, cost.

A new diagnostic tool that reduces overall cost and intrusiveness associated with producing precise results in wind tunnel applications is pressure sensitive paint (PSP). The paint contains a specific chemical which changes the intensity of its luminescence, depending on the partial pressure of oxygen around the test surface. This advanced diagnostic tool is a leader in the development of global measurement techniques in the experimental environment.

Pressure sensitive paint's ability to globally map the pressure levels over an entire model surface is generally complimented by its non-intrusiveness. Including the application of a base coat, the change to the model surface is a thin layer (10-15μm) of paint (19). PSP was originally developed in the Soviet Union in the 1980's, and has continued to evolve from its earliest forms, which were not very sensitive and highly temperature dependent (5). Today's paints are much more advanced and commonly exhibit negligible temperature effects for large ranges of temperature, which can vary depending on the paint and the application environment.

Many studies have been carried out using PSP alone as well as in conjunction with other measurement techniques used for comparison. For instance, PSP has been used in high speed applications (5; 6) and low-speed applications (4; 5). Generally, low speed applications are more challenging due to the higher sensitivity required to capture relatively small changes in pressure. PSP has also been used in comparison with CFD

applications (26). However, there have been few studies that incorporate the PSP and pressure tap data with CFD simulations and traditional force and moment measurements retrieved by an internal balance, the most common method for measuring model forces (3). The intent of this study is to utilize PSP to assess aerodynamics and compare these results with those achieved using CFD.

Section 2 – Project Motivation and Goals

While each of the three elements of rapid technology assessment are useful, they grow in efficiency when they can be integrated throughout a test program. For one example, a model might be designed with pressure taps located in a region near where CFD predicts an unusual result. PSP might then be applied to the model in proximity to the pressure taps leading to improvements in turbulence models used in CFD. To this end, the Air Force Research Laboratory Air Vehicle Directorate (AFRL/VA) is optimizing the integration of test article fabrication, wind tunnel testing, and computational fluid dynamics (CFD) analysis. The primary goal of this optimization program is to develop a process by which each of these three modern, rapid-technology assessment techniques may be incorporated in a complimentary fashion. The portion of this work summarized in the following document is focused on the analysis of measurements acquired in a low speed wind tunnel for a blended wing body model built via rapid prototyping. This analysis presents results in the form of balance measured forces and moments, pressure tap measurements, and PSP data images of the model's upper surface. In addition, comparisons of these results to CFD simulations performed by AFRL/VAAC are also discussed.

The secondary objective of this experimental study is to broaden the capabilities of the Air Force Institute of Technology (AFIT) low-speed wind tunnel. The completion of a full PSP test on a wind tunnel model and the knowledge gained will benefit future students and experimental research at AFIT.

Section 3 - Outline

This section provides an overview of the chapters to follow. Chapter II provides the background of blended wing body aircraft design, as well as the rapid technology methods used in this study. Included in the chapter are the history and details of the PSP methods used along with the theoretical and experimental background of boundary layer theory in conjunction with surface roughness effects. Chapter III details the experimental set-up used to conduct this study, focusing on the wind tunnel force measurements and the PSP data acquisition method. In Chapter IV the results of the experiment are presented and analyzed. Specifically the results are broken into three main sections consisting of the angle of attack sweeps data, the surface roughness data, and the yaw angle sweeps. The first and third sections are subsequently broken into three sections for the data measured using the unpainted model, the painted model, and the comparisons of these two data sets. The unpainted model data are the force and moment measurements from the tunnel balance, while the painted model data also includes these values along with the pressure tap data and the PSP images. Finally, Chapter V includes conclusions and discusses possible applications for future research.

II. Theoretical and Experimental Background

Section 1 – Blended Wing Body Aircraft

In recent years there has been much discussion regarding a replacement for traditional cylindrical fuselage aircraft in order to achieve improved overall characteristics such as aerodynamic efficiency as well as fuel economy. One design option proposed as a successor to the current commercial/bomber/tanker aircraft configuration is the blended wing body (BWB) aircraft. In this type of aircraft, the cylindrical fuselage is replaced with an airfoil-shaped body that contributes to lift (13). This style of aircraft has received much attention and is a leading contender to replace the conventional aircraft design.

The BWB aircraft design carries with it a number of advantages over the current traditional aircraft design; the first and foremost being that the fuselage contributes to lift, thereby reducing required size and complexity of the wings and their incorporated high-lift devices. Typically, a BWB fuselage has a larger internal volume compared to cylindrical fuselages in its class, thereby giving it a wider and taller cabin, as well more space for internal fuel storage. Additionally, it allows for much thinner wings needed for transonic cruise (13). Other advantages as described by Qin et al. include the design's lower wetted area to volume ratio and lower interference drag when compared with conventional fuselage configurations (21). Katz et al. studied a variation of the BWB seen in Figure 1 below. This configuration exhibits similarity to current configurations in that the fuselage is separate from the wings; however, the fuselage is a lifting body in the shape of a NASA 410M6airfoil. Another appealing feature of the BWB and its variations

are its stall resistance at higher angles of attack. The design studied by Katz et al. exhibits vortex lift on the aft section of the fuselage at these high angles of attack. Therefore, an increase the nose-down pitching moment is produced; a characteristic that can be employed to create a stall-safe design. This stall limiting quality is seen in the slope of the lift curve, where the coefficient of lift increases beyond the point of wing stall as show in the figure below (13).
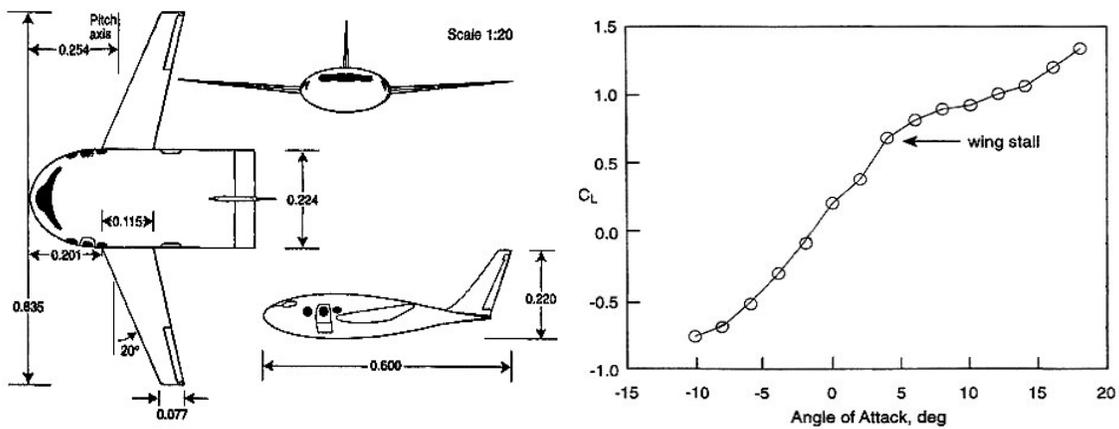
Figure 1: Lifting body aircraft design w/lift coefficient versus angle of attack plot (13).
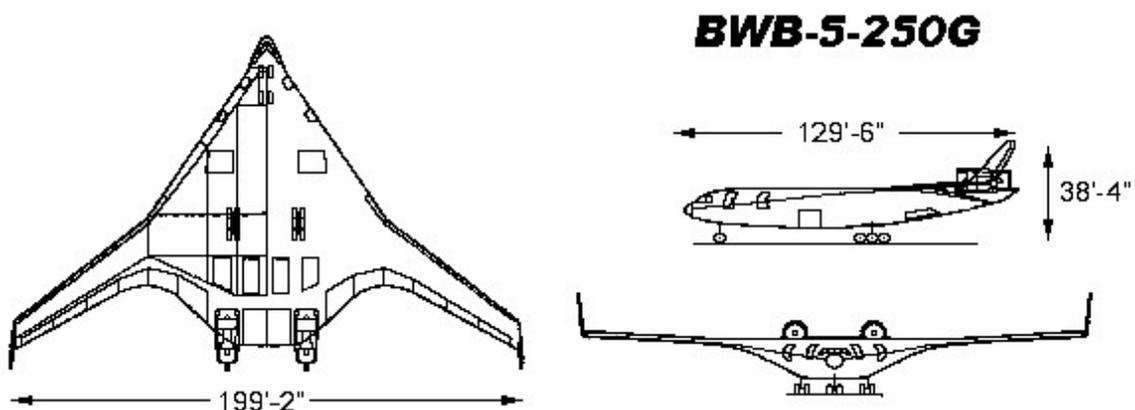
Figure 2: Blended wing body aircraft example configuration (16).

The advantages of the BWB described above have encouraged aircraft designers to establish a new airframe that meets military and commercial requirements; two examples of this new design concept are shown in Figure 2 above. The performance advantages of the BWB would allow it to be used in many military applications such as a freighter, troop transport, tanker, and stand-off bomber (16). The concept of the tanker with drastically increased fuel capacity is one of the most applicable of the potential missions of the BWB, as it could be capable of accompanying a strike force mission, which would eliminate the need for tanker assets to be in place prior to launching bombers (16). This application of the BWB, and specifically its lifting body variant, is the inspiration behind the 'strike tanker' used in this experimental study. The proprietary strike tanker characterized in the current test program was provided by an industrial air framer to AFRL.

Section 2 – Rapid Prototyping

Rapid prototyping is a major technological advantage that tremendously increases the ability of the air framer to quickly and accurately evaluate an aircraft design early in the design process. The process is also conducted based on an electronic model defining the outer surface of the vehicle, which is also used as a starting point to create the CFD mesh used in simulations (28). Fabrication of the model for testing does not end with just the outer surface defined. Many considerations such as mounting (size of sting), instrumentation (pressure taps, etc.), and structural integrity of the prototype must be incorporated into the model design before it is manufactured. Included in the current rapid prototyping processes available are stereo lithography (SLA), selective laser sintering (SLS), laser engineered net-shaping and fused deposition modeling, each

varying by product material and cost. SLS was chosen as the production method for the model in this study. The procedure by which SLS was chosen is described in Chapter III.

The rapid prototyping method known as SLS creates solid, three-dimensional objects by fusing powdered materials with a CO_2 laser (7). The laser beam is projected from a robotic arm which maneuvers over a thin layer of powder particles that has been laid down, sintering them together.   At this point the part moves down on a piston and a new layer of powder is added to the upper surface. When the procedure is repeated, the powder is sintered to the solid part below the powder on the surface.   With more repetition, each layer of powder is sintered and fused together until the part is completed. The last step of SLS involves filling the voids between all of the particles to create a fully dense, high strength part. A schematic of the SLS process is shown in Figure 3 below.
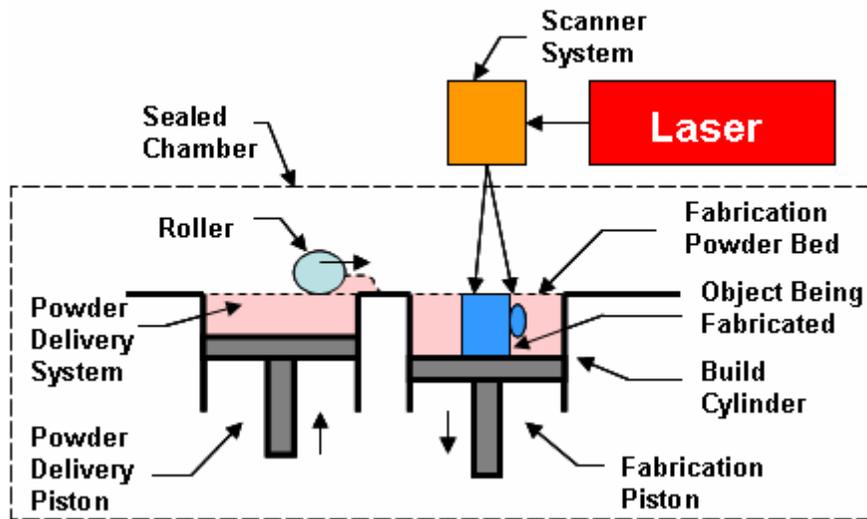
Figure 3: Selective Laser Sintering Process (25)

Although SLS is generally more expensive than other rapid prototyping methods, it has the ability to generate parts using a wide variety of materials including plastics and metals. The metallic parts created using this process typically have physical properties

similar to steel, allowing them to be machined, drilled, and polished like traditional metals (28). Figure 4 and Figure 5 below show the difference between the parts as they come out of the rapid prototyping machine and after they have been machined, assembled, and polished.

Figure 4: Left wing and forward fuselage after SLS fabrication (28).

Figure 5: Wings and forward fuselage assembly after polishing process (28).

Section 3 – Pressure Sensitive Paint

Section 3.1 – PSP Basics

Pressure sensitive paint was created in order to acquire surface pressure measurements without the limits of cost, complexity, and spatial resolution associated with the traditional measurement technique of pressure tap arrays. PSP operates as a non-intrusive pressure measurement due to its oxygen sensitive properties. It typically contains two main parts: an oxygen-sensitive luminescent molecule and a transparent oxygen-permeable binder (5; 20). Since the creation of PSP, the luminescent material and the binder have both evolved considerably in terms of pressure and temperature sensitivity, as well as response time. The earliest luminescent materials consisted of platinum octacthylporphyin (PtOEP) which used a silicone polymer binder. PtOEP typically had a luminescence sensitivity of 0.72%/psig and a response time of 2.5 sec (9). The newer PSP material platinum tetra(pentafluorophenyl) porphyrin (PtTFPP) is used with a fluoroacrylic (fluoro/isopropyl/butyl) polymer binder (FIB). This improved PtTFPP/FIB blend exhibits a pressure sensitivity of 6%/psig and a response time of 0.3 sec (19).

In the PSP process a light of known wavelength illuminates the surface of the model, causing the luminescent molecule to absorb a photon of that wavelength. This causes the molecule to rise to an elevated energy state, a process known as excitation. The molecule then returns to the ground state by releasing a photon of longer wavelength than the one absorbed by a process known as emission. In PSP, this process can take place through several mechanisms; the most common and most predominant of which are radiative decay (luminescence) and nonradiative decay through the release of heat (5).

11

Emitted photons are collected with the use of a charged-coupled device (CCD) camera after passing through a long-pass filter. Figure 6 below shows a schematic of the PSP measurement process.
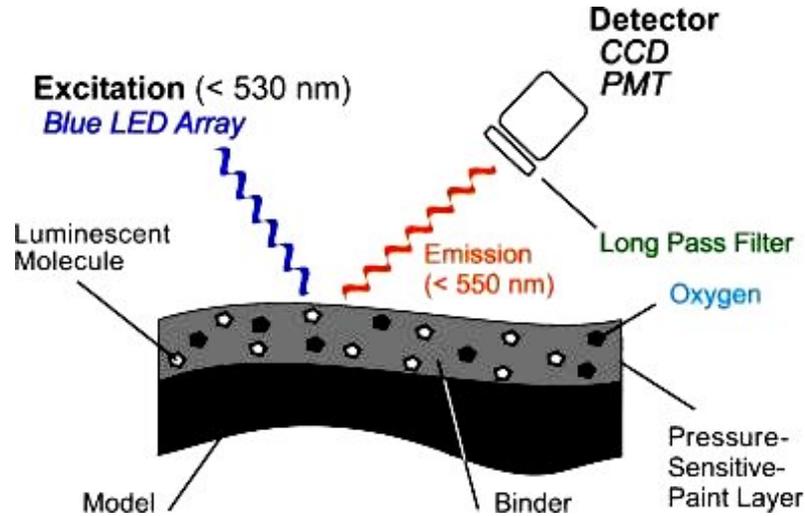
Figure 6: Schematic of PSP principle (20)

In some PSP materials oxygen interacts with the luminescent molecules in a way such that the photon emission during transition to the initial state is radiationless; this process is known as oxygen quenching (20). The rate that the molecules are quenched is directly proportional to the oxygen partial pressure, which is directly proportional to the surface pressure when air is the working fluid. A higher oxygen pressure quenches the molecule to a greater degree, which diminishes the intensity of light emission. Therefore, the PSP luminescence is inversely proportional to local surface pressure (5; 20). This recovered luminescence intensity is described by the Stern-Volmer relationship shown in Equation 1 below (15).

$$\frac{I_0}{I} = 1 + K_{SV} P_{O_2} \tag{1}$$

where I_0 is the *luminescence intensity* in the absence of O_2 (vacuum), I is the *luminescence intensity* at some *partial pressure of oxygen*, P_{O_2}, and K_{SV} is the *Stern – Volmer constant*. Since a vacuum is generally impossible to achieve in wind tunnel application, thus measuring I_0 becomes equally difficult to measure. Thus, a modified form of the Stern-Volmer equation is used wherein the vacuum calibration (I_0) is replaced with a reference standard as shown below in Equation 2.

$$\frac{I_{REF}}{I} = A(T) + B(T)\frac{P}{P_{REF}} \tag{2}$$

where I_{REF} is the *recovered luminescence intensity* at a *reference pressure*, P_{REF}. The measurement technique above is used in the two primary methods of PSP data acquisition, intensity-based and lifetime-based. The intensity-based method was chosen for use in this experimental study and is explained in detail in Chapter III.

Section 3.2 – PSP Effects

Pressure sensitive paint has been determined to have major advantages over pressure taps in the area of wind tunnel measurements and model characterization; including the most prominent that it provides excellent spatial resolution. It is also easily applied and removed from test surfaces, allowing different types of paint to be used on one application with a relatively short turnaround. Although PSP has been classified as non-intrusive, there is still the issue that once the surface of the model has been painted, it has been changed from its original form. Many studies have been performed in this area to determine the effects of PSP and other thin paint coatings on the aerodynamics of wings (1; 23; 29).

Paint coatings applied to wings can alter the airflow and become intrusive by 1) changing the actual shape of the model, for example, adding local thickness, and 2)

13

changing the surface roughness of the model, which can alter the boundary layer development, thus changing the shape of the inviscid stream surfaces (23). Schairer et al. tested a 2-D wing at high and low Reynolds numbers and found that at high Reynolds numbers, the very thin paint layers changed the pressure distributions near stall and post-stall. However, at low Reynolds numbers the paint intrusiveness was quite small and indistinct (23). Vanhoutte et al. conducted a similar low and high subsonic speed study on swept wings. The results of this study showed that on a high lift application at low Reynolds numbers a rough application of PSP influenced the flow around the leading edge, leading to the suppression of laminar bubbles. When tested at high subsonic speed, the application of a rough PSP to the model resulted in large drag penalties (29). Along with the studies mentioned above, another related study in this same area of PSP effects on aerodynamic data performed by Amer et al. concluded that the primary interference effect was due to the thickness of the paint changing the size of the model (1). The paint thickness, typically 10μm, would generally be a factor on models or wings with very small cross-sections. However, it can also affect the spaces between aerodynamic components, for example, the gaps between main wing and flaps (29). Apart from the thickness effects, most paint applications have been found to not exceed the "admissible roughness" criteria, as described by Schlichting (24), necessary for it to have an effect on the boundary layer transition, and in turn, lift and drag. The model surface roughness in conjunction with boundary layers was found to have a large impact on this experimental study; Section 4 below has been devoted entirely to this topic.

Section 4 – Boundary Layer and Surface Roughness

Sixty-five years ago, Herman Schlichting published a compilation of boundary layer theories which has greatly influenced numerous aerodynamic studies and experiments focused on laminar and turbulent boundary layers and the transitions between the two. The control of these boundary layers and more specifically, the effects of surface roughness on boundary layer transition is one topic of particular interest to this experimental study. As mentioned above, Schlichting's admissible roughness criterion is commonly used in engineering applications. It is also used in this experimental study, when classifying the effects of PSP on aerodynamic characteristics. This concept is important for an experimental aerodynamic study as it affects the amount of time and effort applied to achieving a high-quality surface finish.

The admissible roughness concept specifies the maximum height of individual roughness elements that do not cause an increase in drag when compared to a smooth wall. However, it does not apply if the boundary layer is turbulent (24). It is also important to note that its derivation does not take three-dimensional boundary layer effects into account. The first of Schlichting's admissible roughness equations is applicable at both high and low Reynolds numbers, and is defined below in Equation 3.

$$k_{adm} \leq 100 \frac{v}{U_\infty} \tag{3}$$

where the *admissible roughness*, k_{adm}, is determined based on the *kinematic viscosity*, v, and the *fluid velocity*, U_∞. Although the above equation is an acceptable method of determining admissible surface roughness, it has the potential to predict extremely small admissible roughnesses for long bodies when compared to their linear dimensions. For more practical applications, it is better to relate the surface roughness directly to the

15

article length such as a ship's hull length or an aircraft wing cord (24). Equation 4 accommodates for article length by introducing the term along with Reynolds number into Equation 3 as seen below in Equation 4.

$$k_{adm} \leq l \times \frac{100}{R_l} \tag{4}$$

where *characteristic body length*, *l*, is introduced along with *Reynolds number*, $R_l = U_\infty l / v$. This equation is used in conjunction with Figure 83 found in Appendix C: Roughness Applications (Schlichting). The diagram contains a plot of admissible roughnesses versus Reynolds number, using characteristic length as a parameter, as well as a number of typical ranges of Reynolds numbers found in similar engineering applications to those listed above. In addition, a summary of examples of these applications is shown in Table 4 in Appendix C: Roughness Applications (Schlichting), which includes admissible roughnesses compared with the parameters used to calculate them.

Boundary layer roughness also plays a large part in the process of boundary layer transition from laminar to turbulent. It has been determined that at a certain roughness height, know as the critical roughness, transition to turbulence occurs in a laminar boundary layer. This roughness causes the point of transition to move upstream, which in turn affects the drag from the wall (24). This transition relocation is responsible for either an increase or decrease in drag, depending on the shape of the article. An increase in drag occurs when the drag on the body is primarily skin friction drag, and a decrease occurs in the case where the drag is mostly form drag (24). This critical roughness parameter is given by Equation 5 below

$$k_{crit} = 15 \frac{\nu}{\upsilon_*} \tag{5}$$

where $\upsilon_* = \sqrt{\tau_0 / \rho}$ denotes the friction velocity, calculated using the *shear stress at the wall*, τ_0, and the *fluid density*, ρ. The above equations have been widely used in experimental studies to determine boundary layer characteristics through surface roughness parameters. Specific interest to this research is the surface roughness of PSP and its boundary layer transition effects.

As described in the previous section, there have been a number of studies that focused on the intrusion effects of PSP on model aerodynamics and the subsequent experimental results they produce. One such intrusion effect that has received much attention is the surface roughness of the paint. The research in this area, however, has typically been focused on high Reynolds number and high-lift wing applications, due to the more conclusive results achieved at these conditions. In addition, the majority of these tests have been performed on 2-D airfoil sections.

The study performed by Schairer et al. focused on the effects of various paint configurations applied to a supercritical wing at transonic cruise and high-lift wing at subsonic landing. The paint used in the experiments had a roughness height that ranged from 10-20μm, and an rms roughness value, Ra, that was roughly 0.5μm for unpolished paint, and 1.0μm for the polished. The experimental results showed that for both tests the paint intrusiveness was minimal (23). However, it caused an upstream shift of the shock-wave position, a critical quantity of boundary layer development, for the cruise wing at design conditions ($M = 0.8$, $\alpha = 1.75$, $R = 13.6 \times 10^6$). As for the high-lift wing tested at various angles of attacks, the study showed that the stall angle was the quantity affected

by the paint. Schairer et al. found that while the lift slope was largely unaffected, the stall angle decreased slightly upon application of the paint. A final conclusion from the study indicated that the paint thickness was not a factor and that the standard approach to computing admissible roughness per Schlichting was appropriate for predicting paint roughness effects.

In the research conducted by Amer et al. mentioned in the previous section a PSP developed by NASA Langley was used that exhibited a surface roughness smaller than that of the clean wing used in the experiments. In addition, the low-speed testing involving commercial paints showed that the discrepancies in the collected data to be within the error bounds of the wind tunnel balance measurements (1). This demonstrated that PSP effects may be mitigated if close attention is paid to the surface quality before and after paint application.

Vanhoutte et al. conducted the experiments closely related to this thesis study in that they looked at PSP effects on a 30° swept wing at low Reynolds number in addition to transonic flows over an airfoil at high subsonic freestream speeds (29). The low speed tests were performed at speeds of 25m/s, 30m/s and 35m/s, which correspond to Reynolds numbers of 3.7×10^5, 4.44×10^5, and 5.18×10^5, respectively. Several paints were used throughout the testing and one closely matched the characteristics of the paint used in this study. Its thickness was ~ 10μm, and the mean departure of the roughness profile from the reference line (roughness average), Ra, and the peak roughness height, Rt, being measured at 2.29μm and 39.47μm, respectively. The authors indicated that the paint roughness potentially influenced the behavior of the separation bubble, possibly removing it all together, and determined that the roughness may have also induced cross-

18

flow transition, which is a predominant issue in swept wing applications (29). The authors also concluded that the peak roughness height generally returns a safer indication of the surface roughness effects when compared to roughness average, another common definition for equivalent sand roughness.

A recent study performed at the United States Naval Academy focused on the surface finish of a sailboat centerboard. The experiments focused on the surface roughness effects on the lift and drag performance at low and high Reynolds numbers of 5.6×10^5 and 1.06×10^6, respectively. In each successive test, the surface was sanded with a higher grit sandpaper to improve the surface finish, which ranged in rms roughness height from 1.0μm to 11.6μm. The results of the testing showed that at both Reynolds numbers, the unsanded stabilizer exhibited better lift and drag performance than all of the sanded ones. This is shown by the increase in drag and decrease in lift as the surface finish of the stabilizer was smoothed. However, for all test performed below 12° angle of attack, there was no evidence of changes in the lift characteristics due to surface finish effects (17).

The research of micron-sized roughness and its effects on boundary layer transition in swept wing flows performed by Radeztsky et al. is of relevance to this thesis study. Comparisons are made of boundary layer transition location between three surfaces of various roughnesses: 1) a painted surface with a 9μm peak surface roughness, 2) a machine-polished surface with a 0.5μm rms finish, and 3) a hand polished surface with a 0.25μm rms finish. The tests were performed at Reynolds number on the order of 10^6, and showed that the dependence of transition on chord Reynolds number is an effect of roughness Reynolds number as opposed to unit Reynolds number (22). The most

important of the conclusions of this research is that micrometer-sized roughness can have a dramatic effect crossflow-dominated transition in swept-wing flow.

Boundary layer transition and surface roughness effects have been researched for many years; however, the vast majority of the experiment and studies performed have focused on the 2-D boundary layer theories presented by Schlichting (24). These studies on PSP have shown some effects, although minimal, for the small roughness increase due to the paint. Research performed recently has shown that roughness effects exist even at the sub-micron level, especially in swept wing flow applications. This supports the idea that surface roughness greatly influences the 3-D boundary layer effects seen in actual aircraft operations. The importance of the study of these effects is explained below.

In the case of Arrow Air Flight MF1285R, a contracted Douglas DC-8-63 full of United States Army soldiers from the 101st Airborne returning from duty in the Sinai Desert on 11 December 1985. A primary cause of the accident, which resulted in the death of the 248 soldiers and 8 flight crew members on board, was found to be an increase in wing surface roughness due to icing. According to the accident report (2), "The aircraft stalled at a higher than normal air speed after leaving ground effect." The report also states that "The performance of the aircraft after lift-off was below that expected and was consistent with the reduced aerodynamic efficiency and resultant high drag associated with wing ice contamination." The above conclusions of the Canadian Aviation Safety Board are prime examples of the conditions that can occur as stated in the United States FAA published Advisory Circulatory (AC) 20 -117. The following excerpt of the accident report discusses the aerodynamic effects of icing on aircraft wings as defined by the FAA.

AC 20-117 identifies that the effects of ice formation on an aircraft are wide ranging, unpredictable, and dependent upon individual aircraft design. It states that wind tunnel and flight tests indicate that when ice, frost, or snow, having a thickness and surface roughness similar to medium or coarse sandpaper, accumulates on the leading edge and upper surface of a wing, wing lift can be reduced by as much as 30 percent and drag can be increased by 40 percent.

These changes in lift and drag will significantly increase stall speed, reduce controllability, and alter aircraft flight characteristics. It identifies surface roughness as the primary influence in the decrease in lift and increase in drag and emphasizes that take-off not be attempted unless it has been ascertained that all critical components of the aircraft are free of adhering snow, frost, or other ice formations.

The aerodynamic effects of surface roughness described above have been closely researched over many years, and in this case, the accident that occurred simply provides further motivation for the continued study of these important characteristics.

III. Experimental Set-up and Procedure

Section 1 – Rapid Prototyping

The rapid prototyping process of the strike tanker used in this experimental study began with a detailed electronic model, as seen in Figure 7 below, provided to the University of Dayton Research Institute (UDRI), which was the lead organization for the rapid prototype.
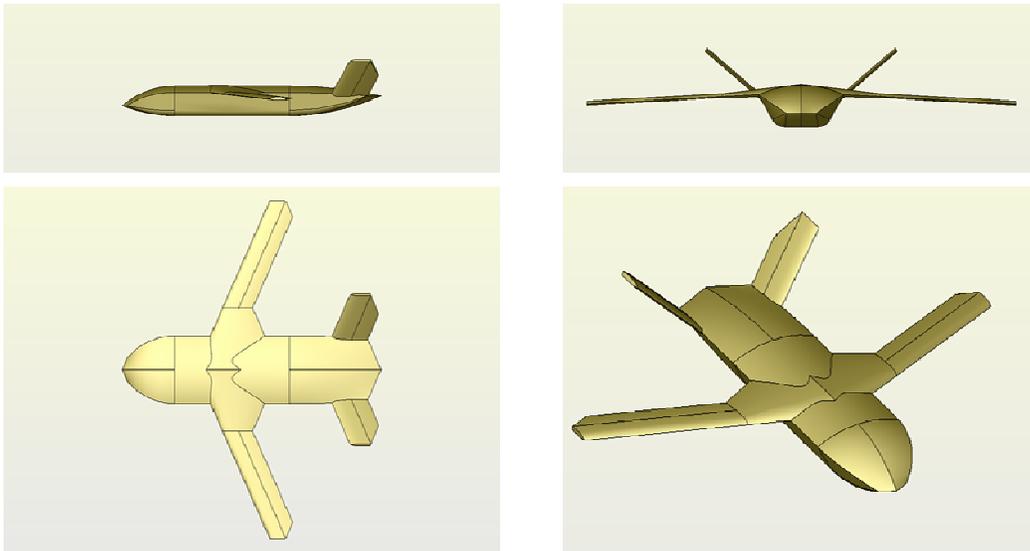
Figure 7: Strike Tanker geometry.

Before the model was created, the issues of mounting, instrumentation, and which fabrication material and technique to be used were addressed (28). The matter of mounting the model within the wind tunnel was the first step as the aerodynamic interference was minimized by creating a cavity in the model in order to mount it to the wind tunnel's balance adaptor and sting apparatus. The balance diameter is 0.5 inches

and the clearance hole in the model is 1.00 inches. The model was designed so that its balance mounting point was at its center of gravity. The aerodynamic force and moment computations were covered by the balance adaptor instrumentation. However, in order to verify the CFD data, as well as the PSP data that would be taken on the model, a set of 8 pressure taps were designed into the upper surface of the model; 4 on each side near the wing-body junction as indicated in Figure 9 below. Each corresponding internal hole was connected to an Endevco pressure transducer via Tygon tubing.

The final step in the rapid prototyping process performed by AFRL and UDRI was to select a material to use for the fabrication of the strike tanker. This process was facilitated with the use of CFD to predict the wing pressure distribution, due to its thin cross section, at Mach 0.2 and 20° angle of attack for both the SLA and SLS model configurations (28). Finite element models were then used to map the CFD results. The determining factor for the technique used was decided based primarily on the deflection analysis. The deflection of the SLA wing was determined to be 0.25 inches, and as shown in Figure 8 below, the maximum deflection of the SLS wing was 0.004 inches. See Appendix B: Additional CFD Solutions for Rapid Prototyping for the wing pressure loading and wing stress solutions also used in the fabrication selection process.

Figure 8: SLS wing deflection (in) at Mach 0.2, 20° angle of attack (28).

The combined restrictions of the wind tunnel dimensions and balance range limited the wingspan of the model to 20.125 inches, which left the model at 1/72 scale. However, the limitations of current SLS equipment capped the maximum part size at 10 inches by 10 inches by 10 inches. The strike tanker model was subsequently fabricated in 6 pieces: forward and aft fuselage, left and right wings, and left and right tail fins. This component breakup is shown in Figure 8 below. Figure 4 in Chapter 2 shows two of the parts immediately after the SLS fabrication process.

The completion of the fabrication process was followed by the machining of the parts and the assembly of the model. The machining operation performed on the model included boring the balance adaptor hole, and drilling and tapping the holes used to attach the model sections. Once it was fully assembled, the surface was polished, and silicone rubber was used to fill seams between the parts. The completed model is shown mounted on the balance in the wind tunnel in Figure 9 below. The strike tanker model used had a 20.125 inch wingspan with a 25 degree rearward sweep angle while the spilt v-tail had an

24

overall span of 9 inches with the same sweep angle as the wing. The body of the strike

tanker was 4 inches wide with an overall length of 16 inches with wing and tail chord

lengths of 1.69 inches and 2.14 inches, respectively.
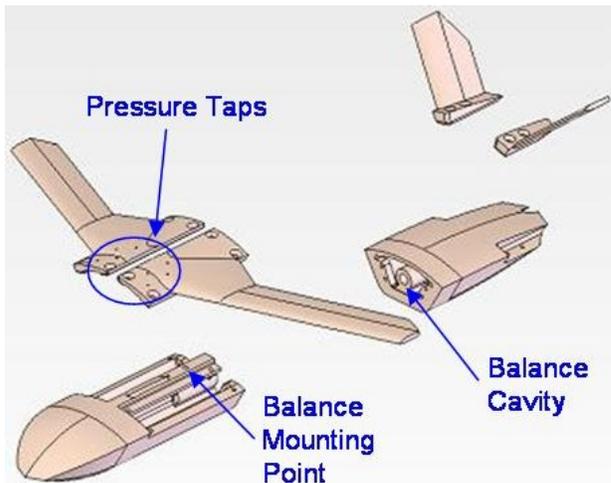
Figure 9: Strike Tanker rapid
prototyping part breakout.

Figure 10: Completed strike tanker
mounted in wind tunnel.

Section 2 – CFD Computations

The computational sciences branch of the Air Vehicles Directorate

(AFRL/VAAC) took the lead role in the CFD study of the strike tanker.   The CFD code

used in calculating the three-dimensional solutions was a full Navier-Stokes code

implementing the Spalart-Allmaras turbulence model (11). The code is an unstructured,

cell-centered, finite volume, Godunov-type solver that uses least-squares gradient

reconstruction and limiting for second-order spatial accuracy, and first order, point-

implicit time interpretation (27). The grid, shown below in Figure 11, consisted of

501,300 cells: 372,472 tetrahedral and 128,828 prisms to achieve a viscous boundary

layer with full effects. An example of a full model pressure distribution achieved with

the CFD code using the described grid is shown in Figure 12 below. As noted in Section 1 above, preliminary CFD results were utilized to predict RP model fabrication. The pressure data computed from the configuration was the primary focus of its use in this experimental study as it was used as a comparison to the force and moment data taken from the tunnel.
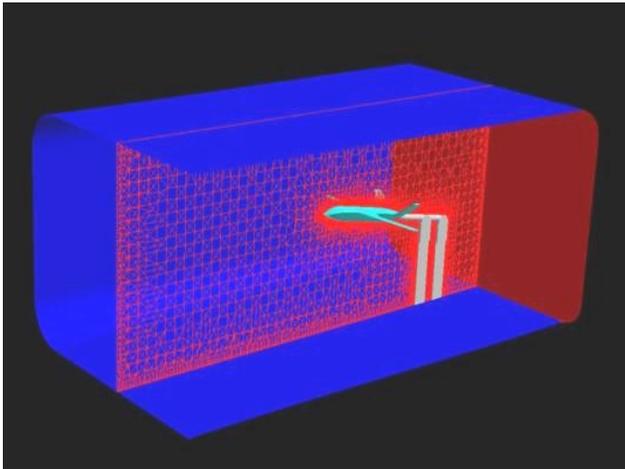
Figure 11: Strike Tanker CFD grid.
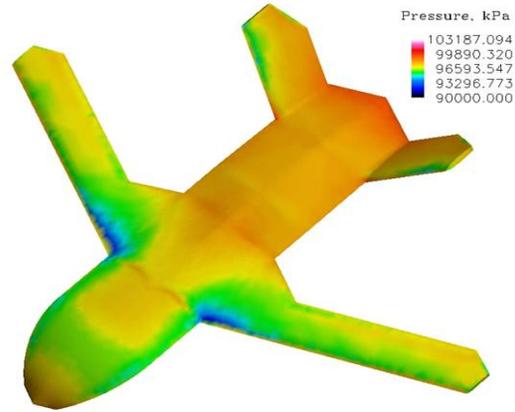
Figure 12: Example CFD pressure distribution.

Section 3 – Wind Tunnel

Section 3.1 – Equipment

The largest and most essential piece of equipment used in this experimental study was the AFIT low-speed wind tunnel. The tunnel was acquired as part of an expansion in 2001 from the New York Blower Company, the fabricator of the tunnel itself, along with the ACF/PLR Class IV fan. The Premium Efficiency (EQP III) fan motor was produced by Toshiba, and the Adjustable Frequency Tunnel Controller was manufactured by

Siemens (13710). The basic specifications of the fan motor and controller are shown in Table 1 below.

Table 1: Fan Motor and Controller Specifications (10).

SPECIFICATIONS	
FAN MOTOR	CONTROLLER
3 phase induction	
4 Poles	
60 Hz	
230/460 Volts	460 Volts
444/222 Amps	315 Amps
200 Brake Horsepower	250 max HP
1785 RPM Operating Speed	
150 mph - Theoretical Max.	
148 mph - Tested Max.	

The tunnel is an Eiffel-type, open circuit configuration with a closed test section. The tunnel fan pulls ambient air from the room first through the 122 inch wide by 111 inch tall by 70 inch deep intake plenum which contains a ¼ inch aluminum honeycomb flow-straightener and steel mesh anti-turbulence screens. The intake apparatus ensures that the flow consists of well-defined laminar streamlines. As the flow passes the last anti turbulence screen, it travels through the convergent section, which is 95.5 inches long and has a contraction ratio of 9.5:1. Figure 12 below shows the intake plenum and the convergent section of the wind tunnel with appropriate dimensions. Additional details of the wind tunnel are given by DeLuca (2004).
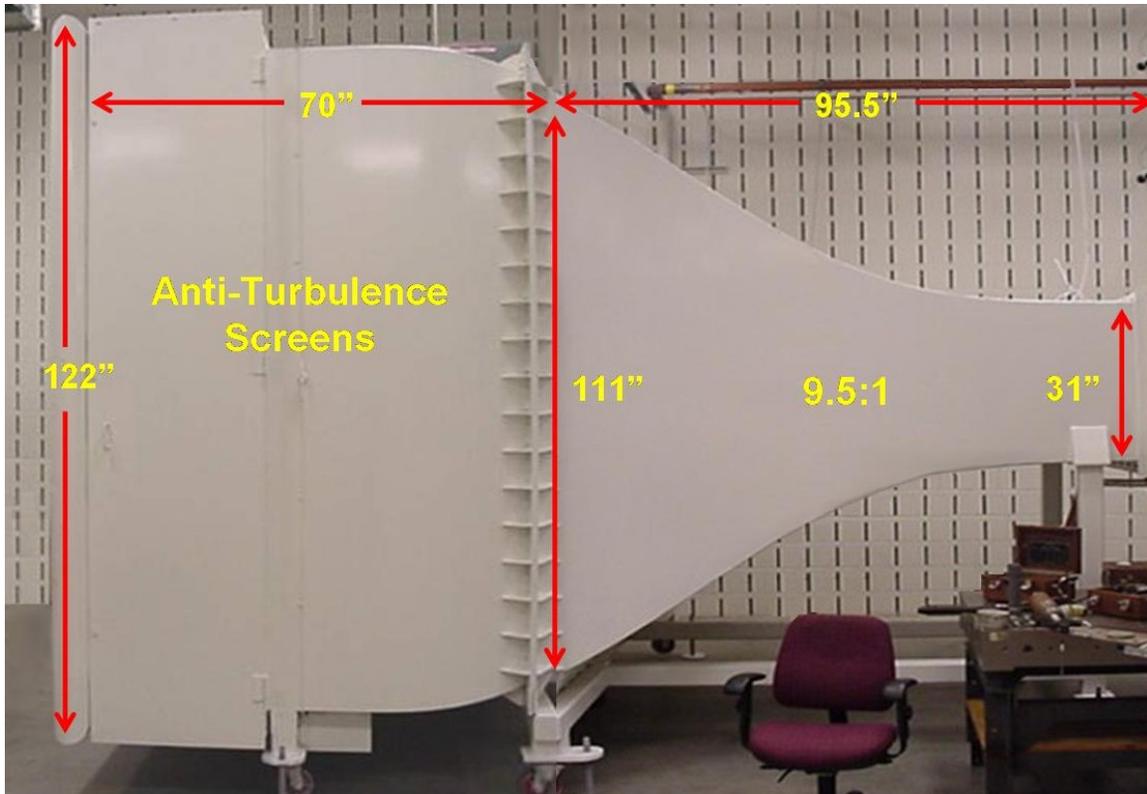
Figure 13: Wind tunnel intake and convergent section (10).

After the flow passes through the convergent section, it enters the 31.5 inch high by 44 inch wide by 72 inch long test section. The strike tanker span-to-tunnel width ratio (*b/w*) of 0.45 falls well under the acceptable ratio according to Barlow et al. ($b/w \le 0.8$). The test section is octagonal in shape, to relieve corner interference effects. The side doors and top panel of the test section are plexiglass, with the doors providing convenient access to the sting and test articles while the top panel is removable to accommodate various testing equipment (i.e. a hot-wire anemometry traversing system). The model support sting enters the test section through a slot in the traverse plate at the bottom of the test section. The sting traverse system allows for angle of attack measurements from -25 degrees to +25 degrees, as well as sideslip angles from -20 degrees to +20 degrees. The

sting mounted balance used to collect the force and moment data for the strike tanker was an Able Corporation Series D, MKII nominal 100-lb$_f$, six-component internal strain gage balance, accurate to 0.25% of full capacity. The capacity specifications of the strain gage rosettes are listed below in Table 2, followed by Figure 13, which shows the test section and all of its components.

Table 2: Able Mark VI strain gage specifications.

0.50 Able Mark VI Balance Specifications	
Normal Force - Total	100 lbf ± 0.25%
Side Force- Total	50 lbf ± 0.25%
Axial Force	50 lbf ± 0.25%
Pitching Moment	52.5 in-lb ± 0.25%
Rolling moment	15 in-lb ± 0.25%
Yawing moment	25.5 in-lb ± 0.25%
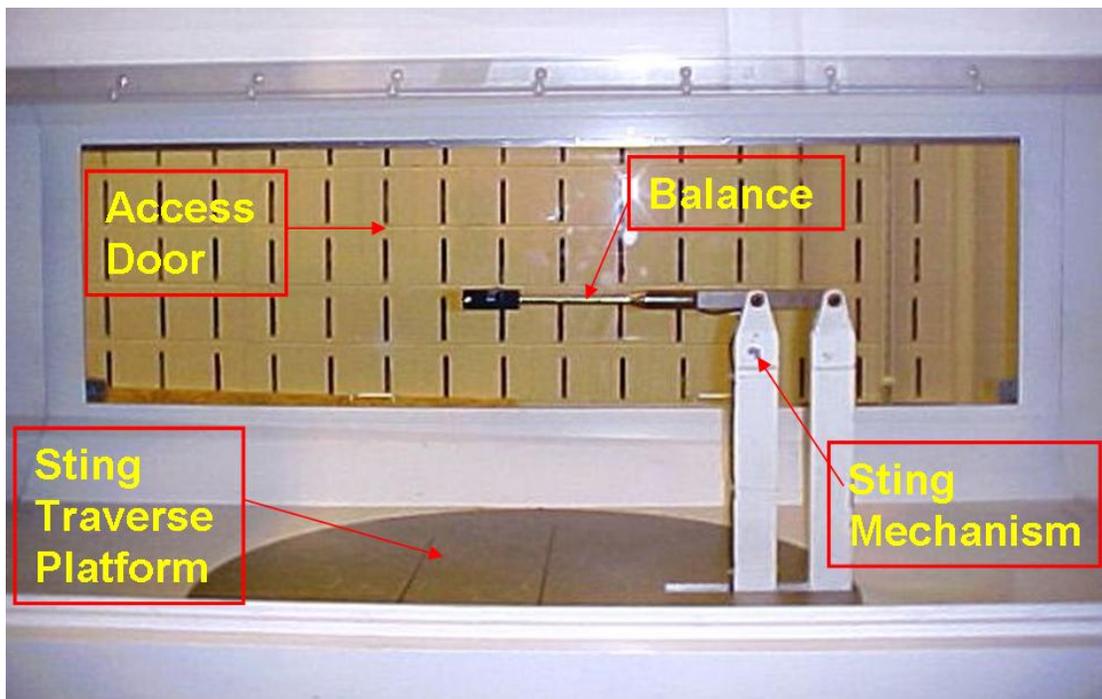
Figure 14: Wind tunnel test section and components.

As the flow continues past the model it carries through the diffuser, which contains a model catcher in the case of catastrophic component failure. At this point it goes through the fan and is directed 90 degrees upward toward the ceiling where it is then exhausted. A schematic of the entire wind tunnel is shown in Figure 15 below.
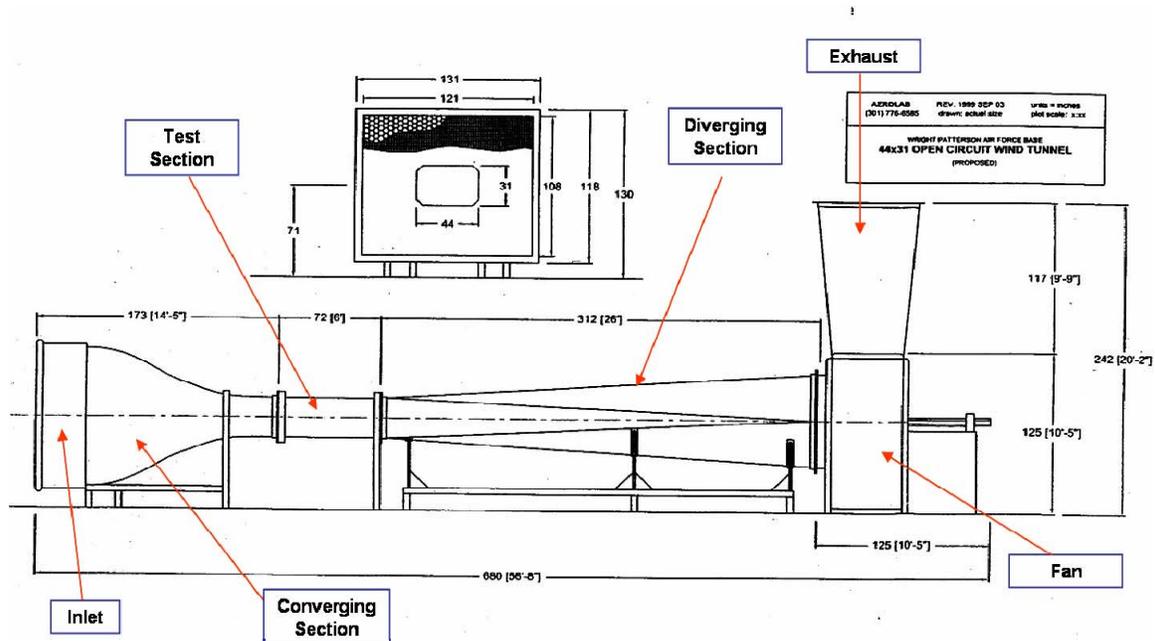
Figure 15: AFIT wind tunnel schematic (27).

Section 3.2 – Procedure

The first step in the wind tunnel testing was to calibrate the balance by attaching known static weights and adjusting the calibration constants in the data collection software. This ensures that the loads registered on the data acquisition system matched the weights attached to the balance sensors. Upon installation in the tunnel, the balance was calibrated and linearized. Weights were applied to each sensor and the output voltage was checked for agreement as the loads were increased in a linear fashion. All measured tunnel parameters including tunnel speed, angle of attack and angle of yaw

were controlled by a computer enabled data acquisition system. The program used for this process was the LabView Virtual Instrument interface. Although the computer system showed and recorded the necessary data for the experiments, analog backups verified the key parameters using a pressure transducer and pitot-static tube for the tunnel speed. The angle and attack and angle of yaw were monitored using sting-mounted optical encoders.

The six-components of the internal strain gage balance measure data and store it in the form of two force components (N_1 & N_2), two side force components (S_1 & S_2), an axial force component (A_1), and a roll moment (L_1). Each of the six sensors is a single axis, strain gage rosette to which voltage is continuously applied. As the voltage is applied to the rosette, the resistance is measured across a wire filament such that an added load produces a strain, and a corresponding elongation, in the wire that relates to an increase in resistance. The change in resistance is equated to a strain based on the output voltage produced, and subsequently related to a force using a series of calibration equations.

The conventional wind tunnel coordinate axis system used by Barlow et al. (3) was utilized and applied to the AFIT wind tunnel as shown in Figure 16 below. The figure indicates the positive wind axes are as they apply to the balance used in this experimental study.
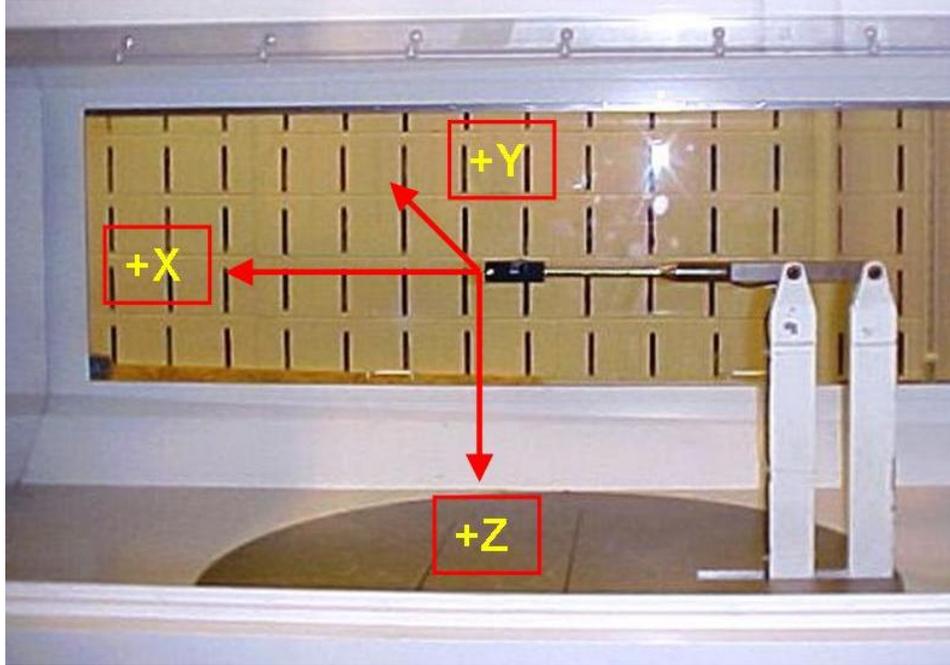
Figure 16: Wind tunnel coordinate system.

With all of the preliminary setup of the wind tunnel completed, the strike tanker was mounted to the balance and sting using a pair of vertical 2-56 set screws located at its center of gravity. Figure 17 and 17 below show the strike tanker as it was mounted in the tunnel for the pre-PSP testing.

Figure 17: Strike Tanker mounted in AFIT wind tunnel – front views.
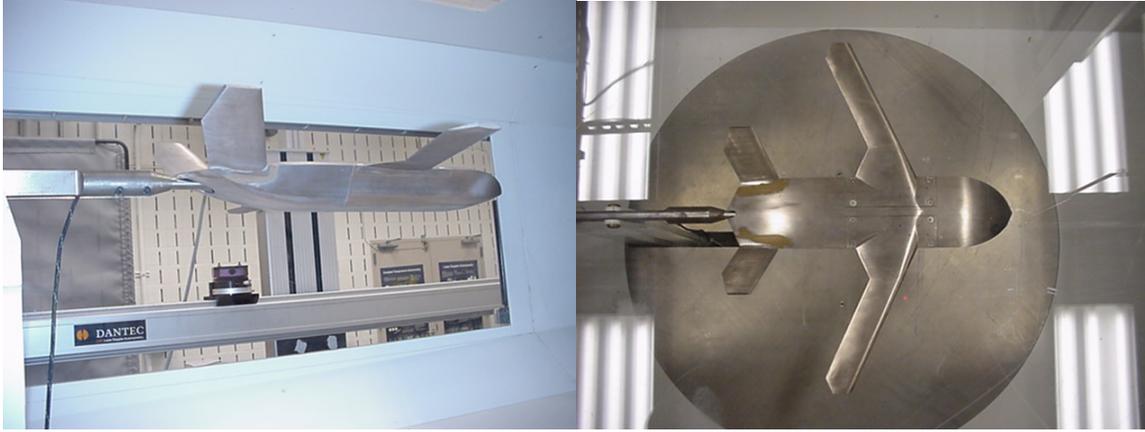
Figure 18: Strike tanker mounted in AFIT wind tunnel – rear and top views.

The initial testing of the strike tanker covered a wide range of test conditions; however, the only data acquired was the force and moment data, as opposed to later tests, which acquired up to three types of data at once. The data acquisition system described above was used for all of the strike tanker tests, including the first set of runs which consisted of angle of attack sweeps from -10 degrees to +25 degrees in one degree increments at speeds of 60 mph, 90 mph, 110 mph, 130 mph, and 145 mph. In addition, two angle of attack sweeps with the same range and increment were performed at yaw angles of +10 degrees and +20 degrees at 110 mph. For each of the experimental runs, a set of wind off data, otherwise known as a tare, was taken in order to zero the balance at each angle of attack. This allowed for the forces of the model itself on the sting to be removed in the ensuing data analysis.

The second set of data acquired occurred a few months after the initial runs, with another data acquisition method subsequently added. In between the data acquisition periods, 8 Endevco pressure transducers (5.0 psig max.) were connected to the taps

described in Section 1 were successfully tested and calibrated. The tap locations and respective nomenclature is shown in Figure 19 below.
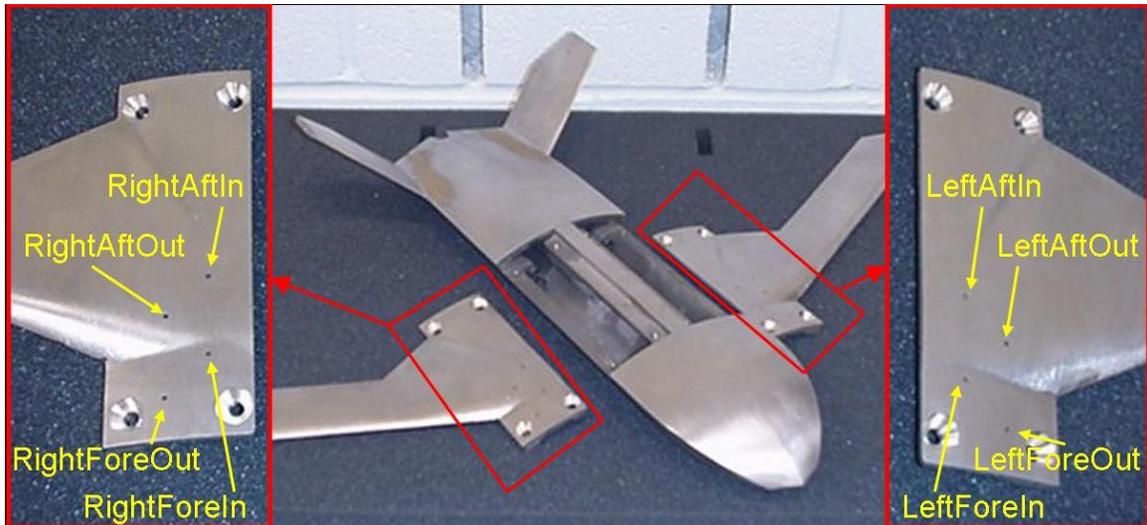
Figure 19: Pressure tap locations and nomenclature.

With the wind tunnel set up and ready to acquire pressure tap data in addition to the force and moment data taken in the previous runs, the testing began with angle of attack sweeps from -2 degrees to +16 degrees in 2 degree increments at 90 mph for varied yaw angles from 0 to +16 in 2 degree increments. The same set of test runs was repeated for a tunnel speed of 130 mph, with tare runs as described above being performed before the wind on tests. Although the pressure tap and force and moment data acquisition continued for the PSP runs discussed in the following section, the primary focus for those tests was on the PSP measurements. Therefore, the test matrix for those data sets will be discussed in the Section 4 Procedure.

Section 3.3 – Data Analysis

The data analysis for the force and moment data acquired from the wind tunnel balance began with the simple bookkeeping of each of the data output files using

Microsoft Excel®. In the initial cases the tare runs were not recorded in separate files due to the number of various speeds being tested, and the balance being zeroed before each run. This required that the data files be split in two; one file containing the wind off data for a given speed, and one containing the wind on data for the same speed. The data acquisition program was set up to store the data on the control computer as a tab-delimited text file at the rate of approximately 2 data points per second (2 Hz sampling rate). For each of the experimental runs, except in the case of the PSP runs, data was collected for approximately 10 seconds at each angle of attack. This resulted in approximately 600 data points for the initial tests encompassing 35 different angles of attack, and 200 points for the second set of test covering 10 angles of attack.

The number of runs tested produced a large amount of data that required reduction before it could be used for aerodynamic calculations. Therefore, a routine was written using MATLAB® to allow the above mentioned split files to be directly read into the data analysis program. The code began by reading in the tare file and stepping through the column containing the angle of attack values. It stepped through the data row by row, grouping like angles of attack together into a matrix. When a change in the angle of attack was reached, a single composite line of data representing $[U_\infty, \alpha, \beta, N_1, N_2, S_1, S_2, A_1, \ell]$ for each test point was calculated by averaging all of the previously grouped data by column, and this average for the given angle of attack was then placed into another separate matrix. The routine continued through the data, averaging all of the acquired data for each angle of attack. Once each angle of attack was averaged, the final matrix consisted of one data point for each angle of attack, with all other corresponding values averaged as well. This set of data was then ready to be used

by the aerodynamic properties calculator. In order for the process to work properly, the tare data and test data must be in the same form, so the exact same code was used for each of the two files that were formed from the original data acquisition output.

The occurrence of spurious data points that may have occurred in transition between tested angles of attack and those caused by model vibrations required that checks be written into the program to exclude them. Depending on the number of data points for each angle of attack, the first few points at each angle of attack were also excluded to ensure there were not transition vibration effects that could affect the data. This procedure led to a drastic reduction in the time required for the processing of the data before the analysis could occur. This additional program was subsequently added to the analysis program written for the AFIT low speed wind tunnel, allowing future studies the opportunity to quickly process the data and ultimately visualize wind tunnel model performance in a matter of minutes.

As mentioned the new routine was added to the MATLAB® program described in Reference 10 and used to reduce all of the test files. The full program was used to calculate all of the aerodynamic properties for the strike tanker model. However, before all of the values were calculated, a lengthy process was carried out in order to characterize the testing conditions of the wind tunnel. The first step in the process was the calculation of all of the physical test conditions such as speed of sound, Mach number, and Reynolds number based on air speed and tunnel temperature and pressure. The next step was to define all of the model and tunnel interference and blockage characteristics. These values are all based on model and test section size parameters and were taken from standard figures in Ref. 3. Once these values were determined, the

36

physical aerodynamic characteristics of the model such as chord length, wing area, and body volume were input along with the balance interactions necessary for evaluating the measured forces. At this point the model's longitudinal stability characteristics were calculated based on the method outlined in Ref. 18, and subsequently all corrections were applied to the aerodynamic properties to produce the final values for inspection. The results were exported to Excel® and all of the aerodynamic properties were plotted according to standard aerodynamic practice. The procedure described above is discussed in detail in Ref. 10, and the program used can be seen in Appendix D: **MATLAB Code for Balance Data Reduction**.

Section 4 – Pressure Sensitive Paint System

Section 4.1 – Equipment

The PSP setup in this experimental study was quite elaborate, due to the number of components that had to function properly at the same time in order to measure pressure distribution. The most important of the component in the experiment was the paint itself, which was the Bi-Luminophore PSP from Innovative Scientific Solutions Inc. (ISSI). This paint was used due to its low temperature sensitivity and its ability to provide compensation for the model displacement relative to the excitation light source, as well as the instability of the light source itself (12). The Bi-Luminophore PSP is very similar to Uni-FIB, a single layer paint composed of PtTFPP that uses a FIB binder; however, it uses a reference probe in addition to the signal probe. The bi-luminophore paint exhibits a pressure sensitivity of 6%/psig and a response time of 0.3 sec and its emission spectrum ranges from 500 nm to 800 nm with a peak at 650 nm with 460 nm illumination at 20 degrees Celsius. The light sources used to illuminate the model for the strike tanker test

37

condition were in the form of an array of 4 of ISSI's 2 inch blue LED light sources emitting the at a wavelength of 405 nm.

The intensity images of the PSP during testing were captured using one of two lenses mounted to a 14-bit Cooke PCO Series 1600 CCD camera linked up with ISSI's image acquisition software, OMS Acquire. Because of the low speed environment of the strike tanker testing and the possibilities for model fluctuation the bi-luminophore paint was used. This type of paint requires that two images be taken at each test condition. The use of a filter wheel is therefore necessary to capture the images separately under the same illumination conditions. The filter wheel used contained a 645-nm long pass filter for the signal probe and a 550 ± 40-nm band-pass filter for the reference probe.

In addition to all of the PSP equipment used for the last set of experimental tests, all of the previously discussed wind tunnel equipment including the force and moment balance and pressure tap system was used. The pressure tap equipment of special importance as it was used as a reference for comparison against the PSP data.

Section 4.2 – Procedure

Although the PSP calibration process was carried out well in advance of the actual wind tunnel testing, it is an integral part of the overall process. The equipment and procedure used for calibration of a binary pressure-sensitive paint is quite similar to that used for single component paint systems. Due to the ability of the bi-luminophore PSP to hold a calibration over an extended period of time, this process was carried out prior to the model being painted. According to the ISSI website, Ref. 19, the paint has a shelf life of approximately one year, and the photo degradation of the luminescence molecules during testing ~ 1%/hr.

38

The calibration process is a vital step in PSP experiment success. This process was performed by ISSI and is discussed below. First, a pressure-sensitive paint calibration chamber was used to control the temperature and pressures to which the paint was exposed. A 4 cm by 4 cm aluminum coupon was painted with the binary pressure sensitive paint, seated onto a Peltier thermo-electric cooler and mounted inside the calibration chamber. A Ruska pressure controller was used to control the calibration chamber while the temperature of the sample was controlled using an Omega temperature controller. The sample was then illuminated using an ISSI LM-2 Lamp, this lamp uses an array of 76 blue LED's to produce excitation at 405 ± 10 nm. Once the illumination source reached nominal operating condition, the sample was imaged through a filter wheel onto a PCO Series 1600 CCD camera. The filter wheel used contained a 645-nm long pass filter for the signal probe and a 550 ± 40-nm band-pass filter for the reference probe (12).

The calibration was started by recording the luminescence of the signal and reference probes at the reference condition of 298 K and 14.70 psia. The temperature and pressure within the chamber were then varied over a range of temperatures and pressures and the luminescence from each probe was recorded at each condition and the wind on and wind off ratio was computed and plotted versus pressure (12). The calibrations for this binary paint (BF405) are shown in Figure 20 below. As can be seen this paint exhibits good pressure sensitivity (4.5% per psi) with very little temperature sensitivity (less than 0.03 % per K). Since the paint had been previously calibrated, it was not detrimental to the model's paint coating to mount it on the wind tunnel sting to prepare it for testing. The only precautions necessary were in handling the model since the bi-

luminophore paint is very brittle and has the potential to be scraped off with a fingernail. In order to prevent paint degradation, the lights in the wind tunnel room were left off when setup was not taking place. Figure 21 below shows the painted model mounted in the wind tunnel.
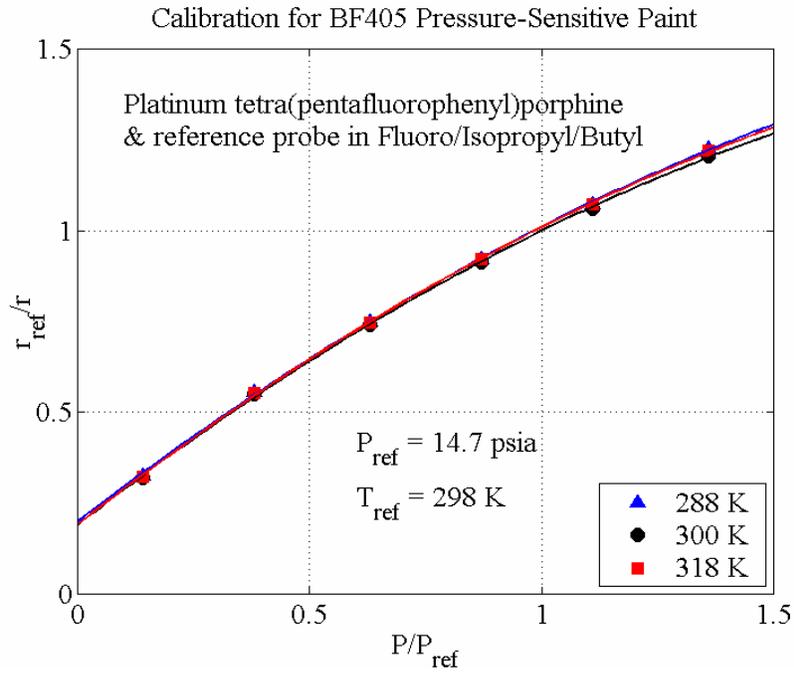
Figure 20: ISSI Binary FIB (BF405) PSP calibration chart (12).
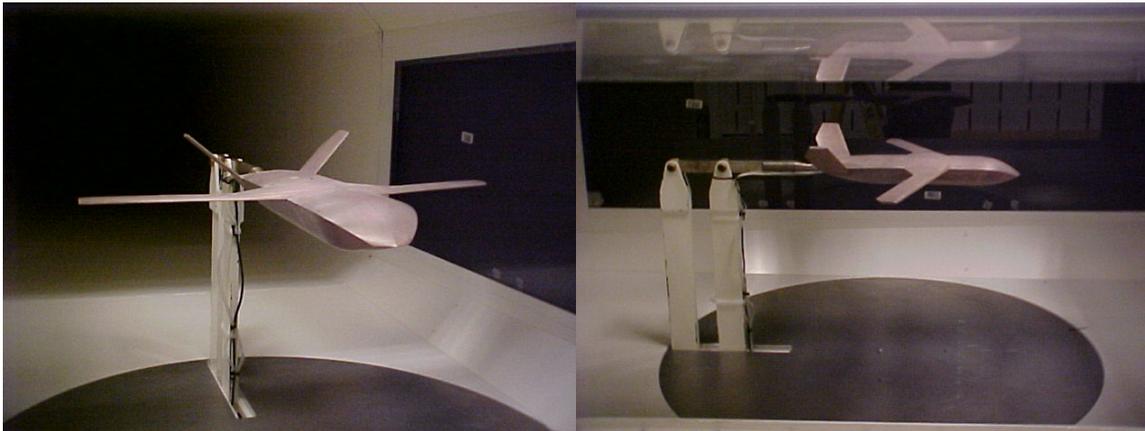
Figure 21: Strike Tanker model mounted in wind tunnel with PSP.

Two basic configurations of the equipment described in Section 4.1 were used based on the specific conditions being tested. The test conditions run utilizing the configuration in Figure 22 below included angle of attack sweeps from 0 to 20 degrees in 2 degree increments for the model full view at speeds of 110 mph and 145 mph. This data set was then repeated with a closer view of the wing and forward fuselage, and a yaw angle sweep from -12 degrees to +12 degrees in 4 degree increments. The camera was equipped with the 16 mm lens with the f-stop set to 5.6 in order to slightly reduce the amount of light allowed into camera. This lens was used for the full view test, as well as the yaw sweep test. The light sources for the above tests were grouped in order to achieve better resolution on the wings, leaving 3 of them mounted aft of the test section aimed towards the tunnel inlet, while the 4th was mounted at the front of the test section to light up the forward fuselage.

For the full view tests, the binning of the data acquisition program was set to 2, effectively reducing the overall resolution of the camera from 1200 x 1600 pixels to 600 x 800 pixels. Basically, the pixels on the camera were summed up in a 2x2 block. When the images are binned by 2, approximately 100,000 photons are collected per pixel, improving the low speed data by reducing the effect of camera shot noise. This setting also allows the data to be collected much faster with much smaller file sizes, increasing the overall number of available tests. The faster data collection also reduces the drift in the data due to photo-degradation and sedimentation, as they are a function of time. The exposure time was accordingly set to 500ms for the full view tests. At each individual test point in the runs described above, the acquisition system effectively returned 5 data images for each filter, giving a total of 10 for each angle of attack or yaw. Within each of

41

the 10 data sets, 20 images of the above mentioned exposure times were averaged together. The method by which the 10 data sets were processed is explained in further detail in the following section.
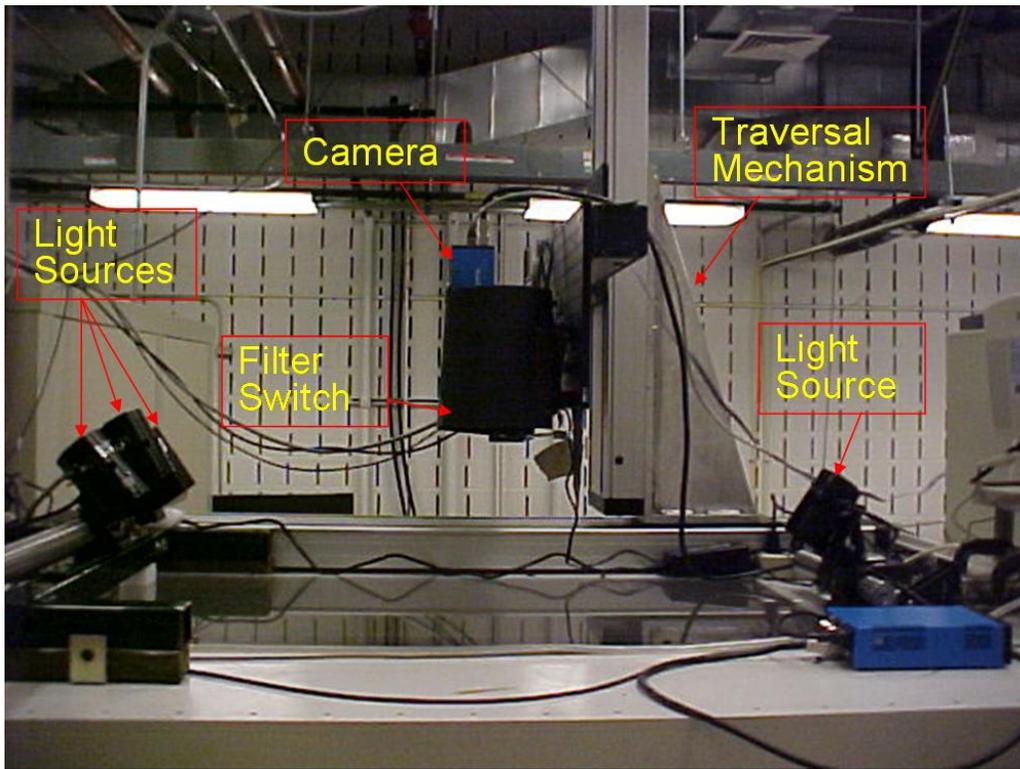
Figure 22: Experimental setup of PSP full view, half view, and yaw runs.

Once testing was completed on the conditions described above, the camera lens was removed and replaced with a 35 mm lens with the f-stop again set to 5.6. This lens allowed the camera to zoom in on just the left wing of the model. The tests performed using this focused lens measured data at the angles of attack in the stall regions as determined from the force and moment data measured in the first set of wind tunnel tests. The alpha sweeps for the 110 mph case covered angles of 14 degrees to 18 degrees, while the alpha run for the 145 mph test measured at angles between 5 degrees and 9 degrees.

For the focused tests, the binning of the data acquisition program was decreased from 2 to 1 to give better spatial resolution and the exposure time was subsequently increased from the 500ms used for the full view tests to 2000 ms to assist in this process. The experimental setup for these runs resembles the first tests, so the used of Figure 23 below is to assist in visualizing the setup from above the test section.
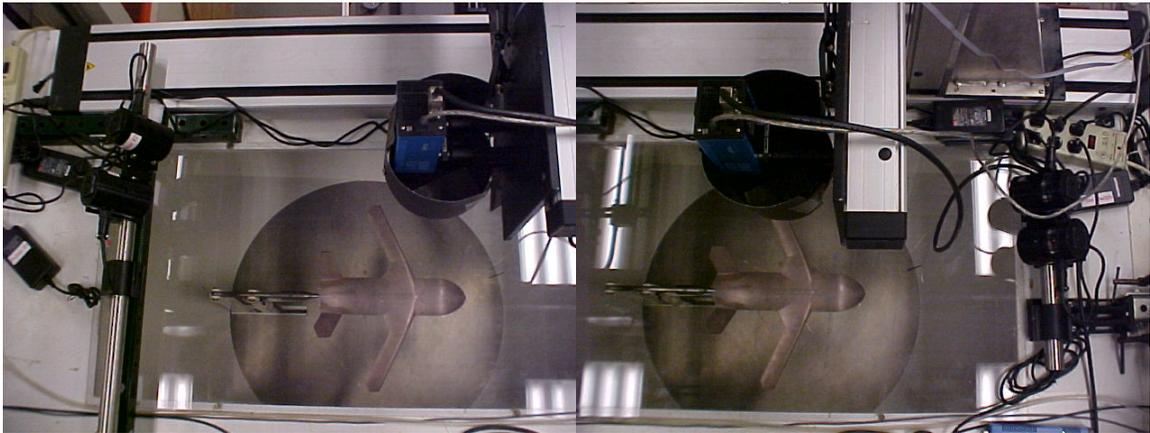
Figure 23: Experimental setup of PSP wing focused runs.

Section 4.3 – Data Analysis

The PSP method used in this study is known as the intensity-based method. The bi-luminophore PSP used in the experiments is typically an excellent paint to use in conjunction with this method. The analysis began with the reference image that was acquired at ambient pressures, also known as a "wind-off" image. In addition, a "dark", or background, image (PSP lighting system off) was taken to characterize the ambient light in the room with all systems off. These images along with those acquired during testing conditions, or "wind-on" images, were processed using ISSI's OMS Lite Version 1.0 software in order to obtain surface pressure plots.

Before the pressure distributions were calculated, however, the acquired images were aligned through the use of marker points on the model. These marker points were placed on various locations of interest on the model (i.e. leading and trailing edges). Subsequently, the 30+ marker points were pinpointed in all 4 images at each angle of attack in order to achieve the best resolution in the pressure data. Once the image markers were set, the images were aligned with the option of various filtering and smoothing methods. For all tested cases, a Gaussian filter was used on the images to help reduce rms noise, with the maximum half width of the filter set to 10 pixels in the x- and y-directions. The limits on the low pass filter were set to 0.7 and 1.3 for the minimum and maximum image values, respectively. These set limits determine the values to be thrown out before the data is smoothed. The size of the filter discussed above simply determines how much the data is smeared in the filtering process. For a bigger filter, the data is smeared more. The data smearing only becomes an issue where sharp changes in pressure gradients occur, as in the case of a shock wave. The corresponding calibration coefficients of the paint were then combined with the "dark", "wind-off", and "wind-on" images and the test conditions were set. Once the global pressures were calculated, the output data was saved into a format exportable to MATLAB in order to properly format the images and apply pressure offsets as determined from the pressure tap data.

Section 5 – Surface Roughness Measurements

The final measurements made in this experimental study were those of the surface roughness of the model with and without paint. Although the PSP covered the entire surface of the model during the tests performed for this thesis, a small area of unpainted model surface became exposed when the skin friction tape applied by ISSI after the PSP

testing was removed. This allowed for the painted and unpainted model surface roughness measurements to be taken at the same time without stripping any paint using harsh chemicals. Figure 22 below shows the locations of the various roughness tests performed on the model fuselage.
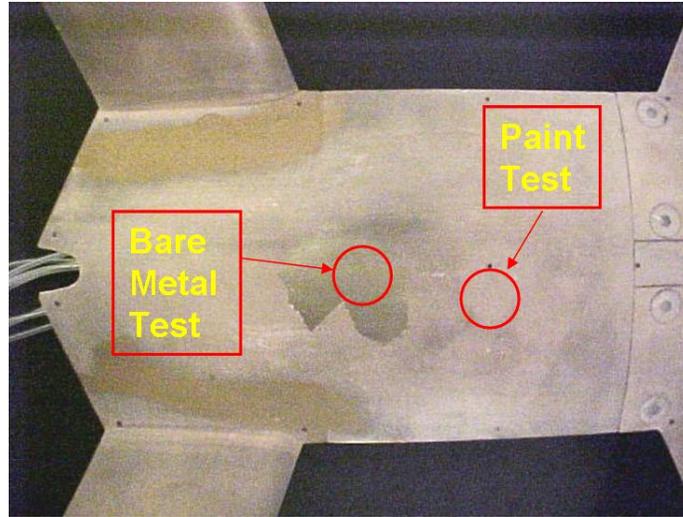
Figure 24: Fuselage surface roughness test locations.

The system used to measure the surface roughness parameters was a Taylor Form Talysurf Series 2 50i using a 60mm arm with a diamond stylus that provided 16nm resolution. This testing apparatus is illustrated in Figure 21 below. The process of obtaining the measurements was quite simple. The model was placed on the test stand, the stylus pointer was then adjusted to a location a few millimeters above the model using the built in traversal system. Once the stylus was correctly aligned to the chosen test area, the system began a measurement over a 6mm length. The stylus automatically lowered to the contact point and then traversed the 6mm toward the rear of the model. Once the measurement was complete, plots were produced that showed the various

roughness parameters such as rms roughness height, Ra, and peak roughness height, Rt. The test described was repeated on the metal to consistency, and was performed at locations on the fuselage and wing to verify equivalent paint roughness at different locations.

Figure 25: Surface roughness measurement setup and equipment.

IV. Results

Section 1 – Angle of Attack Sweeps

This experimental study focused primarily on characterizing a strike tanker using the tools of rapid design and assessment. The lift and drag characteristics of the strike tanker model were measured using a six-component balance, pressure taps, and PSP measurements. Angle of attack sweeps were used for the majority of the tests. The alpha sweeps provided the baseline for the lift and drag characteristics as well as the pitching moment data. Other stability characteristics were determined using yaw angle sweeps and corresponding PSP measurements; however, the data is somewhat limited.

Section 1.1 – Force and Moment Data

Section 1.1.1 – Unpainted Model

The first and one of the most important set of tests performed was the alpha sweeps with the unpainted model. The resulting force and moment measurements allowed for the initial characterization of the model through the use of the five figures below. They not only show the behavior of the model in its original form, but also give insight into what test conditions would provide the most insight for future experimental runs. The first figure and the one that ultimately determined the test path in this study is the lift coefficient versus angle of attack comparison for the test speeds of 60, 90, 110, 130, and 145 mph. These air speeds correspond to Reynolds number, based on wing chord, ranging from 0.74×10^5 to 1.79×10^5. As seen in Figure 26 below, there are obvious stall events that occur for each of the test speeds with the exception of 60 mph. The stall events, however, were not predicted by initial CFD runs. At pre-stall angles of

attack the slope of the lift curve is generally the same for all speeds; however, as the speed increases, the stall events occur at smaller and smaller angles of attack. The data also show that for each stall event, the overall decrease in the lift coefficient becomes smaller as the speed increases, which also leads to the post-stall lift being higher at the higher test speeds. Notably, the lift coefficient declines abruptly due to the wing stall, however, the lift curve continues to rise due to the lifting properties of the aircraft body.

Lift Coefficient Vs. Angle of Attack - Unpainted Model
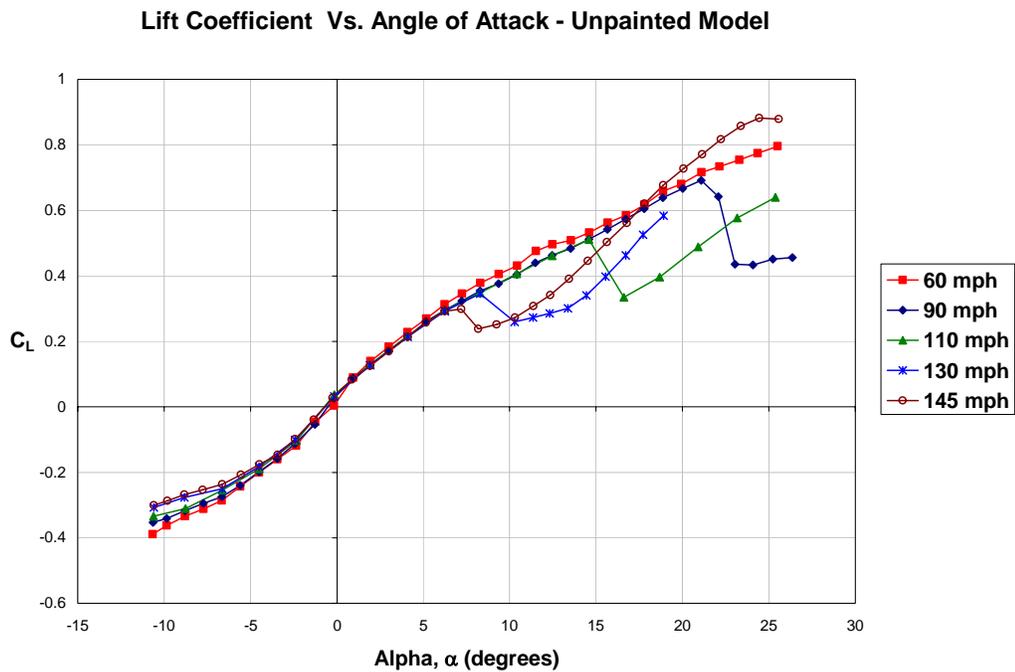
Figure 26: Unpainted model lift at 60, 90, 110, 130, and 145 mph.

The unpainted strike tanker drag characteristics shown in Figure 27 below are best explained by the changes in total drag due to variations in the skin friction drag, the induced drag, and the form drag. As with the C_L, the C_D vs. α data for all speeds collapses before the stall events occur, and at each stall event the drag decreases abruptly; however, its is a smaller decrease in drag at the stall event as the air speed increases. The

48

alignment of the data at angles of attack near zero is due to the of skin friction drag on the model, which is followed by an increase in the induced drag and thus C_D, as the angle of attack increases. As boundary layer separation begins, the form drag is also added to the total drag, which in turn continues the positive drag slope. However, as the wings stall the drag abruptly decreases due to the drop in induced drag, forming a dip in the drag curve. As the angle of attack increases, the form drag increases, allowing the overall drag coefficient to maintain a positive slope, as. It is also noted that the post-stall drag is higher for higher air speeds, although the overall slopes of the curves remain similar.

Drag Coefficient Vs. Angle of Attack - Unpainted Model
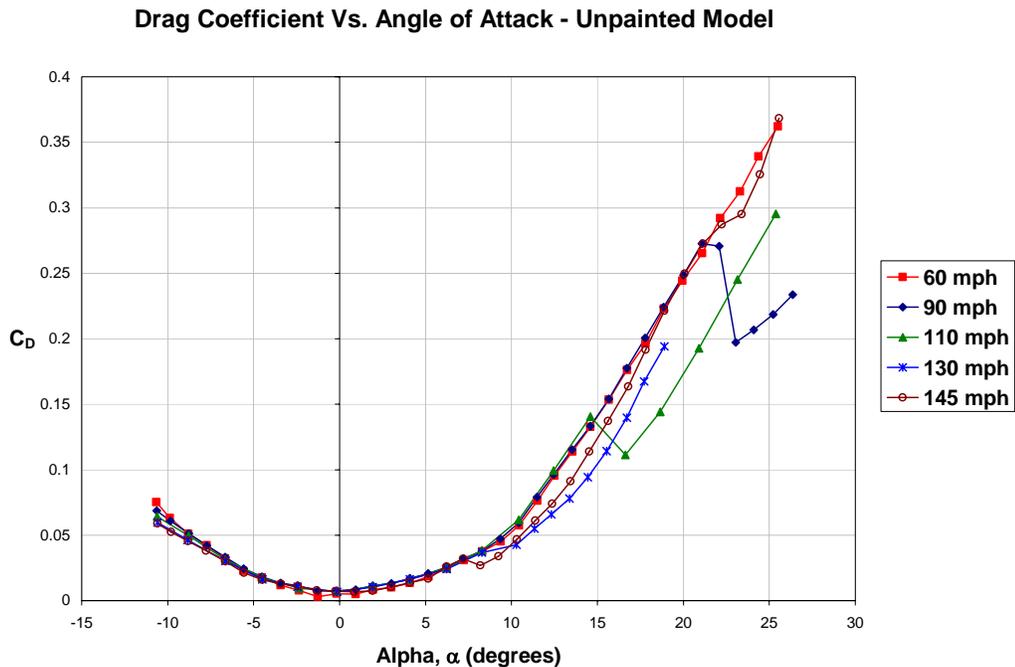
Figure 27: Unpainted model drag at 60, 90, 110, 130, and 145 mph.

The two graphs that follow are critical in defining the lift and drag efficiency and how they relate to each other over the course of each experimental run. Figure 28 below presents the same data in the form of a drag polar of the model for each speed. Similar

49

characteristics are seen as those in the lift and drag versus angle of attack graphs. The drag polars agree quite well until the stall event occurs, at which point the drag and the lift drop, forming a trough of efficiency completely different from that of pre-stall. It is noted that within the stall regions the decrease in C_L is more substantial than the accompanying reduction in C_D. For example, in the 110 mph test, C_L experiences a decrease of approximately 35%, while drop in C_D is only about 20%. This can be attributed to the loss of the induced drag from the wing lift, which in the case of the strike tanker, is smaller than the overall form drag from the lifting body.

Lift Coefficient Vs. Drag Coefficient - Unpainted Model
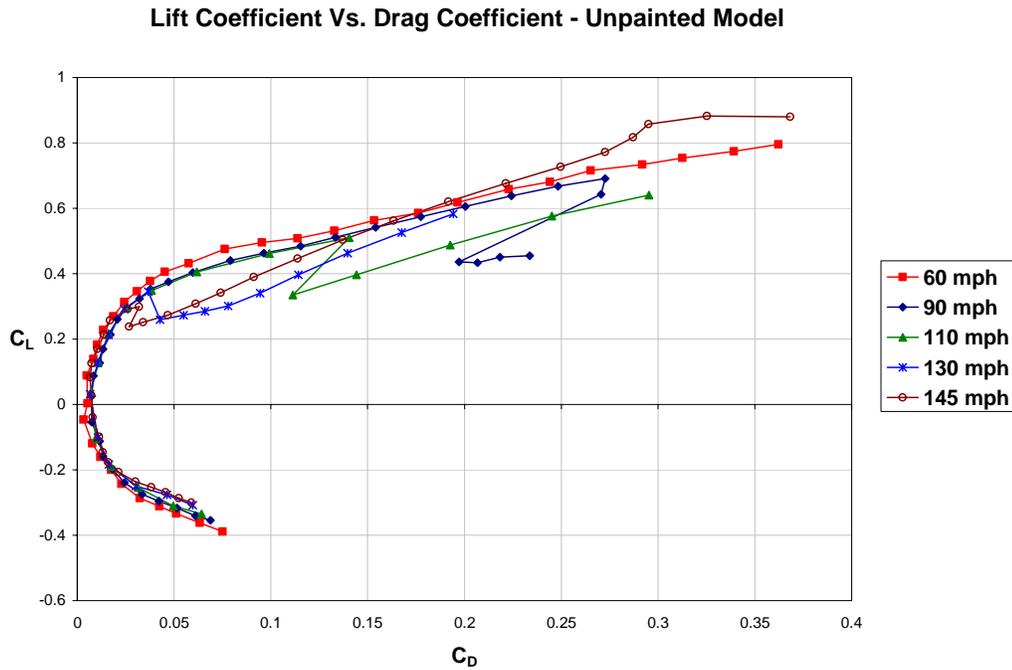
Figure 28: Unpainted model drag polar at 60, 90, 110, 130, and 145 mph.

Figure 29 below shows the efficiency in terms of lift-to-drag ratio versus angle of attack. As air speed increases, the lift-to-drag ratios are higher at low angles of attack; however, the ratios tend to collapse at higher angles. However, the 110 mph and 130

mph case exhibit a nearly equal ratio throughout the entire range of angles, and the 60

mph case shows that its lift-to-drag efficiency at low angles of attack is even higher than

that of the 145 mph case. The discrepancies in the lift-to-drag ratios below are evidence

of the limitations of the data resolution when small angles of attack are combined with

even smaller drag coefficients. These limitations are more prominent at the lower speed,

as shown by the 60 mph data below.
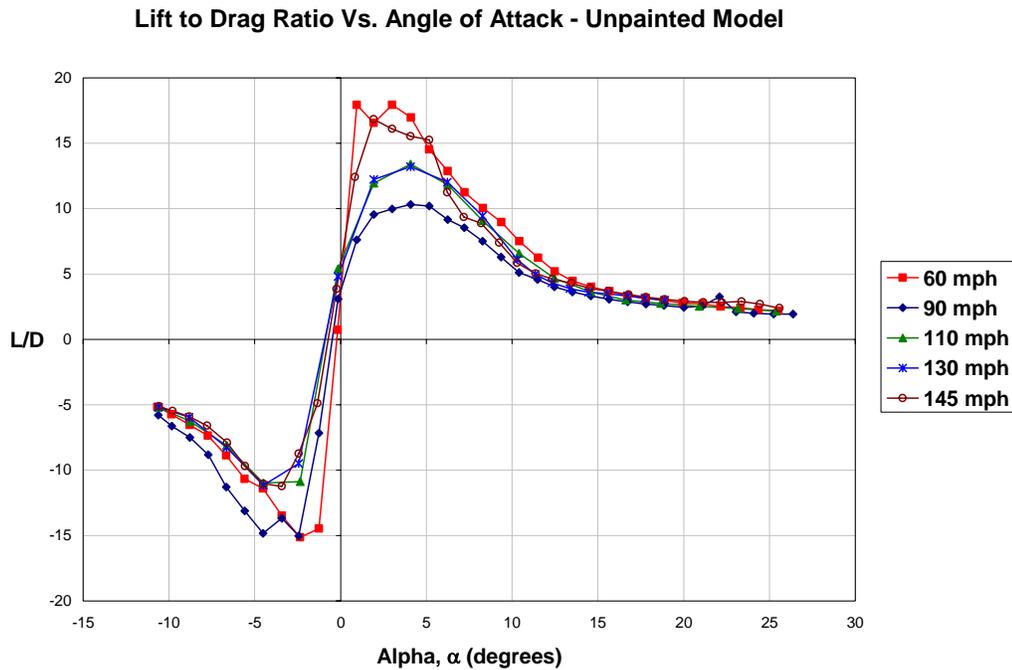
Figure 29: Unpainted model lift-to-drag ratio at 60, 90, 110, 130, and 145 mph.

As discussed, the figure above shows the differences in resolution at low and high

angles of attack. The measurement errors of the balance based on the tolerances given in

Table 2 are exhibited as a worst-case scenario shown in Figure 30 below. The errors in

the lift-to-drag ratio as determined represent the limits of the balance measurements of

the lift and drag forces for the 90 mph and 145 mph tests of the unpainted model. As

seen, the error is much larger at lower angles of attack due to the resolution of the balance measurements for small drag forces. As the angle of attack increases, the error decreases to the point where it becomes negligible above 12 degrees. Also noted is that the errors in the 90 mph data are higher than those seen for the 145 mph tests. Again, this is due to the higher drag forces measured as air speed increases, allowing better overall resolution of the lift-to-drag ratio.
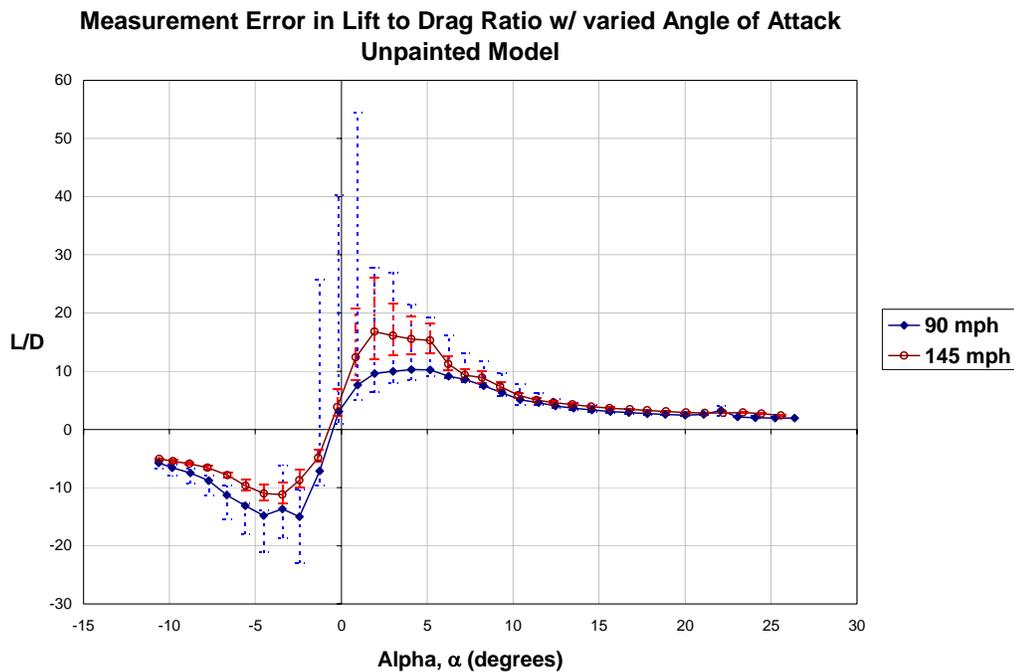
Figure 30: Balance error in lift-to-drag ratios at 90 mph and 145 mph.

The final graph used to analyze the initial force and moment data taken on the unpainted model compares the pitching moment coefficients for each air speed. The trends exhibited in Figure 31 below are very similar to those shown in the lift data, in that it is a mirror image. The pitching moment coefficient data, however, presents a different type of information, with the same overall result. Pitching moment coefficients are a

measure of the aircraft stability and as in the lift and drag data, a large, abrupt increase is seen at the stall event. The post-stall data returns to a steadily decreasing slope slightly lower than that seen before stall. The increase in C_M seen at the stall event corresponds to a decrease in longitudinal stability. This instability is of importance in that it largely decreases the controllability of the aircraft and in turn the overall flying properties.

Pitching Moment Coefficient Vs. Angle of Attack - Unpainted Model
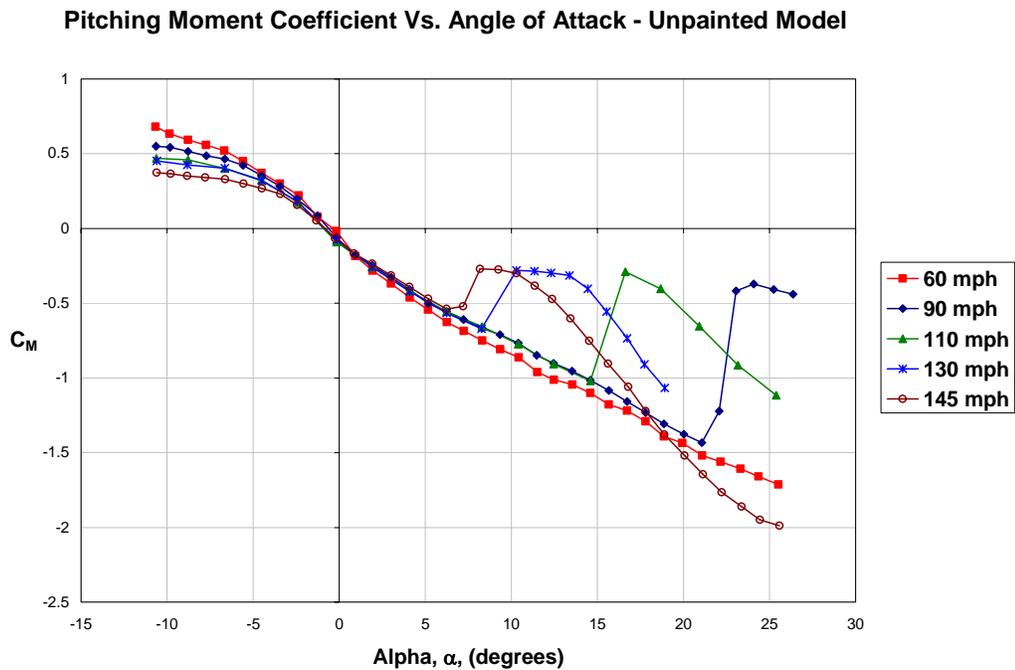
Figure 31: Unpainted model pitching moment at 60, 90, 110, 130, and 145 mph.

The following two plots are presented in order to show the repeatability of the unpainted force and moment data measured by the wind tunnel balance during test performed on days separated by three months. As seen in Figure 32, the lift and drag coefficient agreement for the 90 mph tests is quite excellent, as is the case for the 130 mph tests, with lift and drag data shown in Figure 33 below.

Lift and Drag Coefficients Vs. Angle of Attack
90 mph
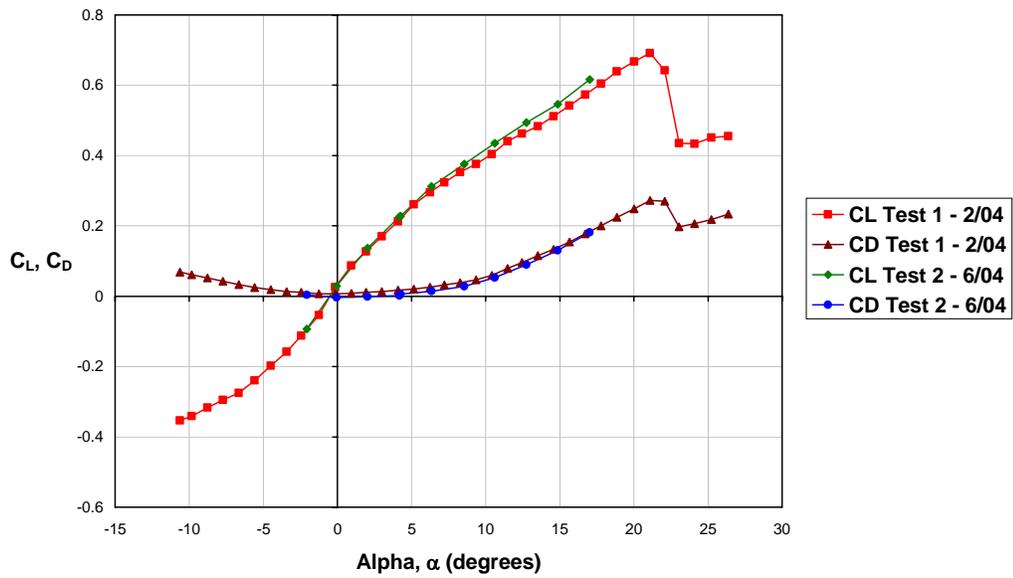
Figure 32: Unpainted model lift and drag for 2 separate tests at 90 mph.

Lift and Drag Coefficients Vs. Angle of Attack
130 mph
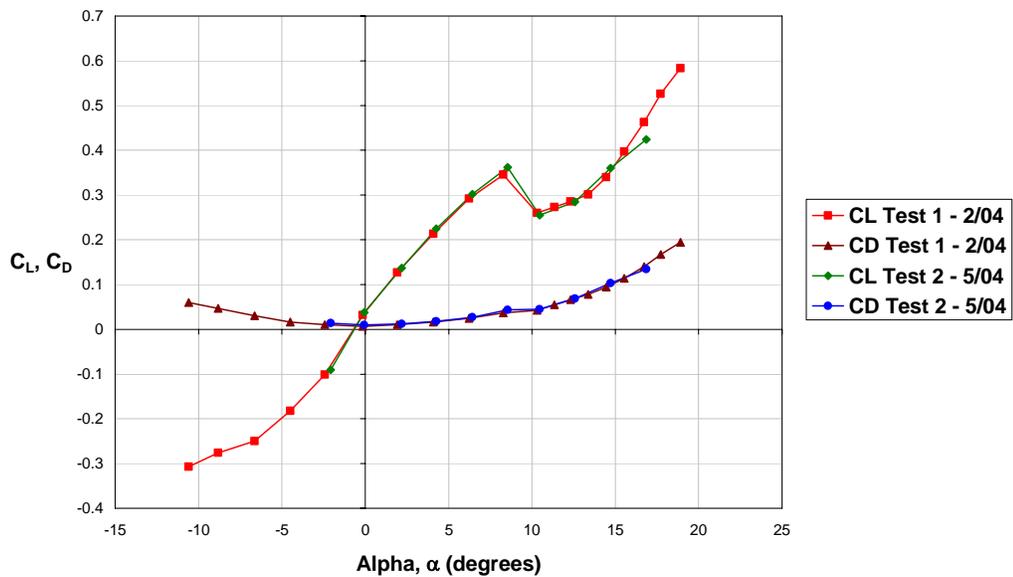
Figure 33: Unpainted model lift and drag for 2 separate tests at 130 mph.

In addition to the data shown above, a final set of alpha sweeps were carried out as the paint was gradually removed from the model in order to clarify the abrupt stall event. The paint was removed methodically in order to determine the effect that the paint had on each particular model component. As shown below in Figure 34, there is little variation in the drag coefficients for all the various data sets, except for the drag curve from data acquired in February 2004. However, the most prominent of the data are the lift curves of the data taken as the paint was removed. As seen the three curves are in between those of the unpainted model and painted model (12/9/04) lift curves. Also noted is that the lift curve exhibited a closer relation to the original unpainted model data as paint was removed, with the largest difference seen after the paint was removed from the tail sections. The actual unpainted model surface is somewhat unattainable due to the application of the paint, even though it was removed using acetone. Even the acetone may have affected the finish; thus, further research into the paint effects is necessary.
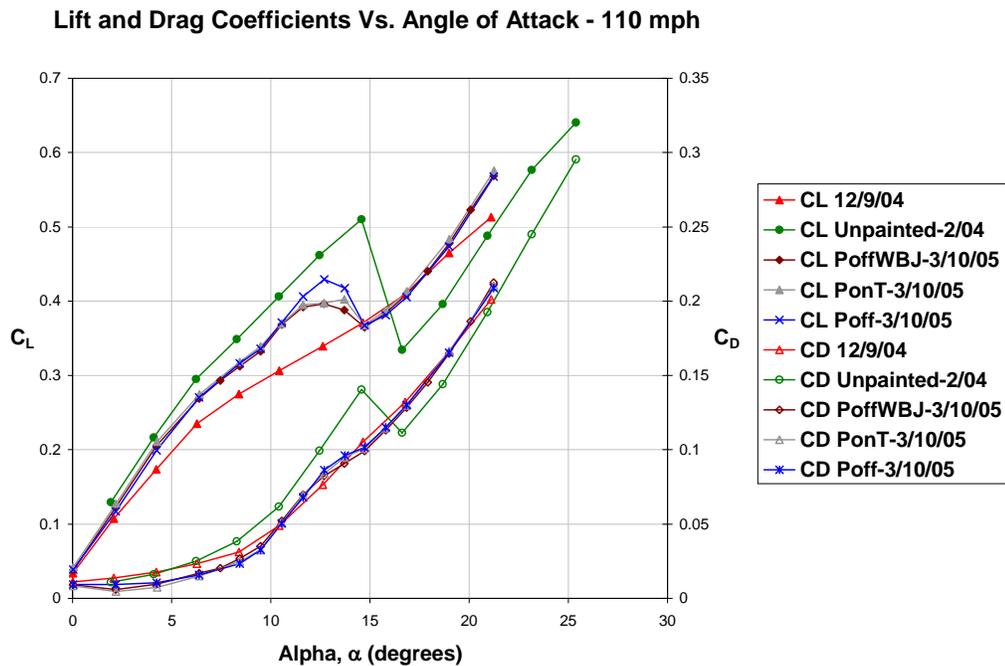
Figure 34: Lift and drag coefficient comparisons of painted and unpainted models.

55

Section 1.1.2 – Painted Model

The balance measured force and moment data for the unpainted strike tanker model showed some unusual stall events that were not predicted by CFD. Since one of the overarching goals of this research is to utilize global measurements to improve CFD, it was decided to focus the majority of PSP tests on the alpha runs to learn more about this stall event. Therefore, the same type of force and moment data was collected for the painted model during the PSP testing. The two speeds tested were chosen for use in comparison with CFD for the 110 mph case, and in order to achieve maximum PSP visualization for the 145 mph case. For each case, as determined from the data on the unpainted model, two additional runs focused on the range of angles of attack where the stall events occurred.

Lift Coefficient Vs. Angle of Attack - Painted Model
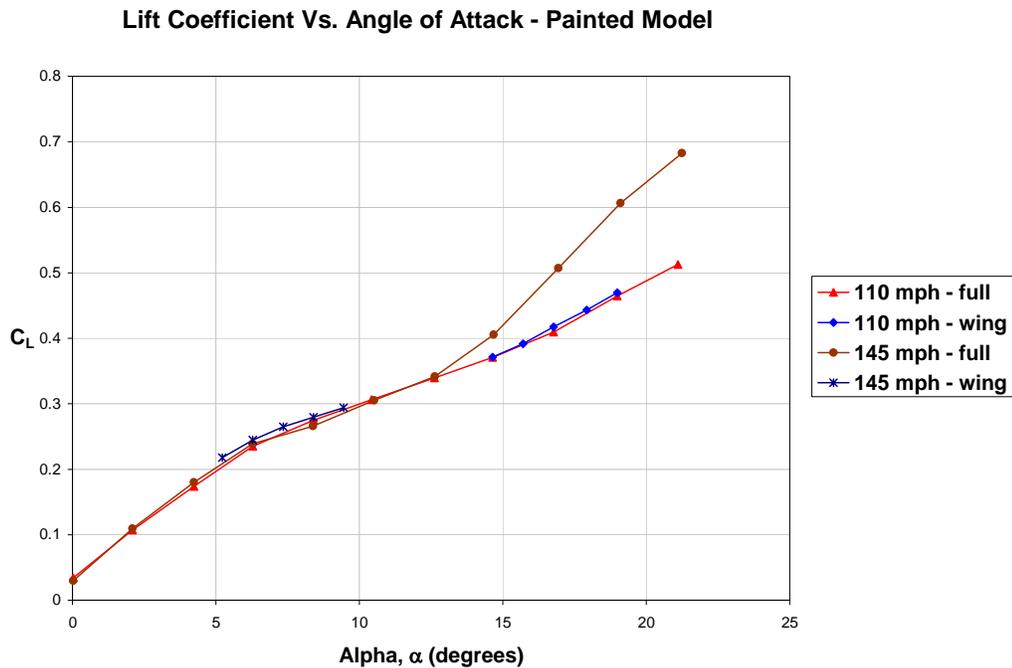
Figure 35: Painted model lift coefficients at 110 and 145 mph.

The lift coefficient data of the painted model is represented in Figure 35 above. Two separate sets of data were collected on the same day at each air speed with the second run focused on a smaller range of alpha, near the stall region associated with the unpainted model. The focused test runs agree quite well with the full alpha sweeps. As seen, the lift slopes follow the same trend until approximately 12 degrees, at which point the 110 mph case continues its current trend while the slope of the 145 mph increases. The results were surprising in that there was no evidence of the stall event which was the most prominent feature of the tests performed on the unpainted model. Aside from being surprising, this result was also inconvenient in that the PSP was applied in order to shed light on the event which it apparently suppressed.

The drag characteristics of the painted model show slightly more than the lift characteristics described above. Again both cases follow the same general trend until the 15 degree point where the 110 mph slope continues and the 145 mph data shows an increase in drag as found at the higher angles of attack. As seen in Figure 36 below, the full and focused 110 mph data agree, while the full sweep 145 mph case contains a small anomaly in the drag coefficient at about 8 degrees. However, the focused data does not show any abnormal trends, indicating that this point is likely a spurious data point.

The next graph relating the lift and drag efficiency for the painted model exhibits the very same trends as the figures above. Figure 37 below shows the test case drag polars, and again the slopes are similar for both cases. When they separate in this graph however, a slight slope difference can be seen in the 110 mph case at the first point of the focused run, which is 14 degrees. This agrees with the general trends seen in the above graphs although the slope change is more evident in the figure below.

57

Drag Coefficient Vs. Angle of Attack - Painted Model
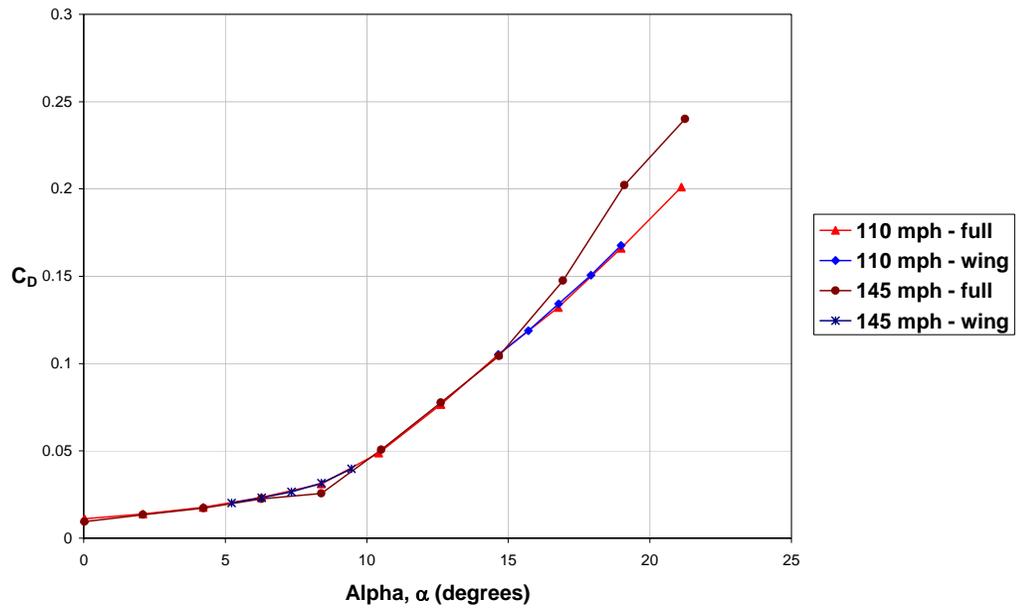
Figure 36: Painted model drag coefficients at 110 and 145 mph.

Lift Coefficient Vs. Drag Coefficient - Painted Model
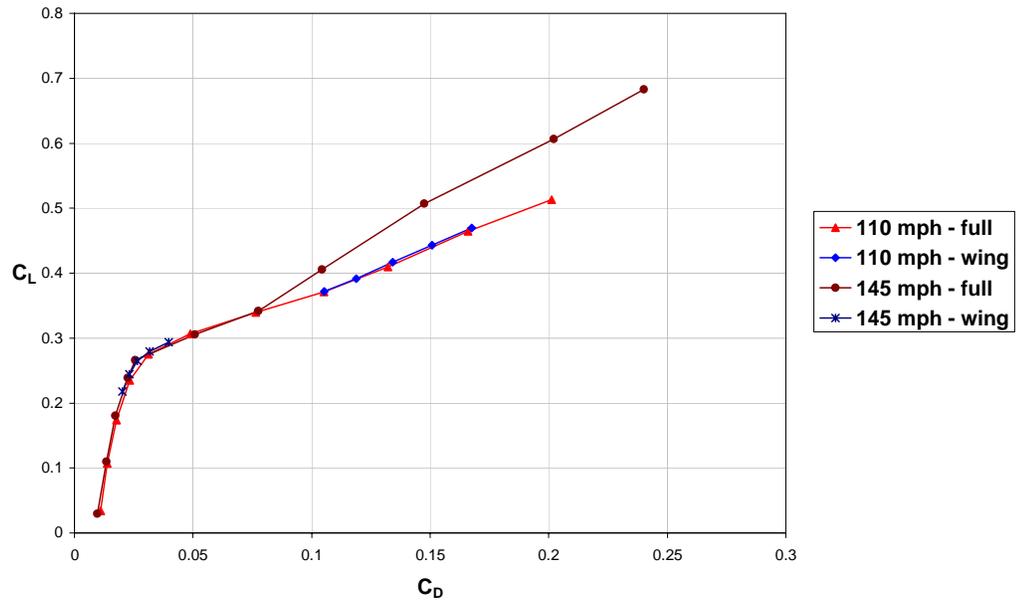
Figure 37: Painted model drag polar at 110 and 145 mph.

The lift-to-drag ratio data is given in Figure 38. For both the 110 mph and the 145 mph runs, L/D peaks between $\alpha = 4°$ and $\alpha = 6°$. The maximum value of L/D was approximately 10.5 for the 145 mph case and 10.0 for the 110 mph case. The data presented in the graph for the full 145 mph case shows a bump in the peak of the low angle of attack data, while the focused data simply follows the trend of the 110 mph case. This indicates that it is likely a spurious data point, along with the fact that the lift-to-drag ratio would not increase in the region of stall, but decrease accordingly.

Lift to Drag Ratio Vs. Angle of Attack - Painted Model
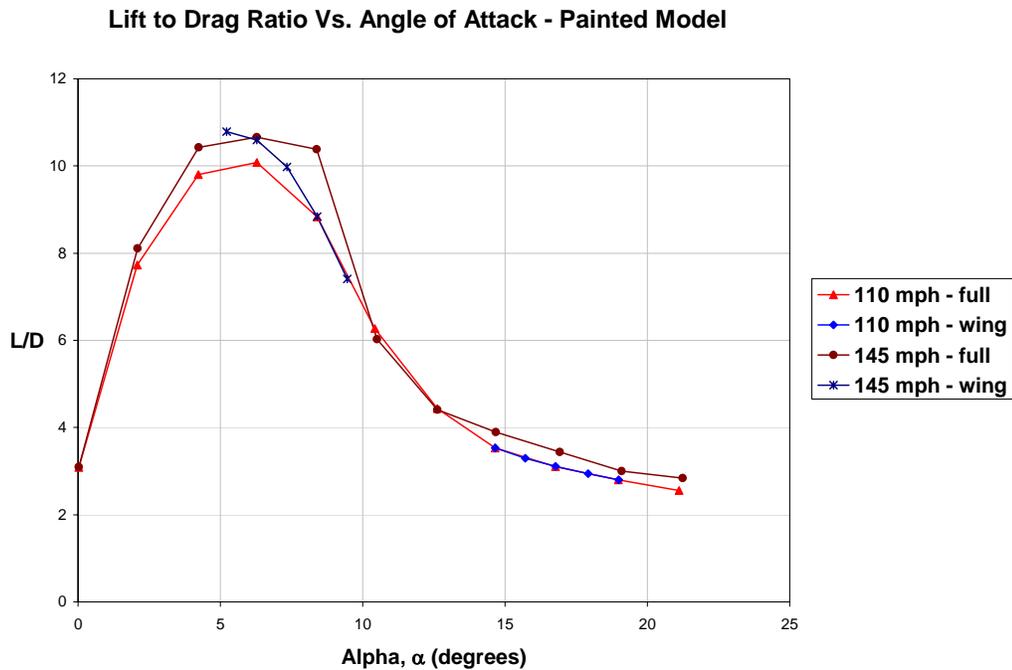
Figure 38: Painted model lift-to-drag ratio at 110 and 145 mph.

The pitching moment coefficients about the center of gravity for the painted model, as they vary with angle of attack, are shown in Figure 39 below. The agreement between full and focused test cases was not quite as good for this moment data, but remained within 10% for the 145 mph case, and 3% for the 110 mph case. The C_M data

for the two air speeds essentially overlap up to $\alpha = 12°$. For larger values of α however, C_M declines more rapidly for the higher air speed. Despite the issue of repeatability between the full and focused alpha sweep data, the overall longitudinal stability of the painted model is far better than that of the unpainted model. This is based on the steady slope of the pitching moment curve seen below, with absolutely no evidence of the previously measured stall event and its abrupt nose-up pitching moment increase.

Pitching Moment Coefficient Vs. Angle of Attack
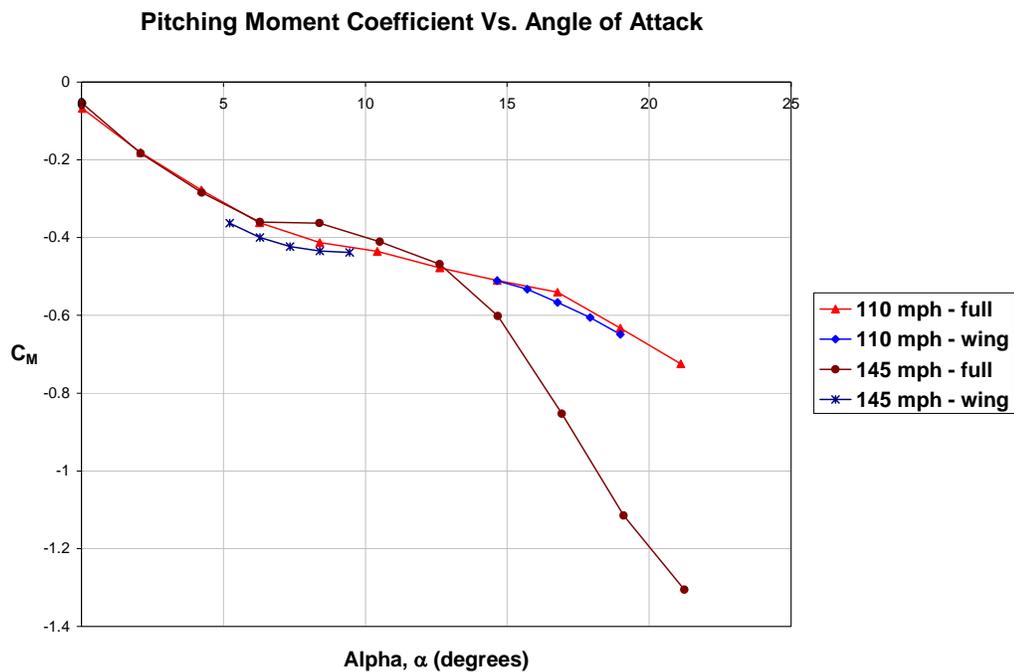
Figure 39: Painted model pitching moment at 110 and 145 mph.

Section 1.1.3 – Comparisons

The following section focuses on the differences between the unpainted and painted force and moment data based on the test speeds. The same five graph types shown above are used for comparisons in this section with the 110 mph figures including additional data from CFD calculations. Comparing the unpainted and painted model

force and moment data in terms of lift and drag characteristics is vital to determining not only the accuracy of the results, but also the effect that the PSP has on the aerodynamics of the strike tanker model. The 110 mph case contains CFD data, attained as discussed in Chapter 3, added for further comparison. Figure 40 below shows the lift characteristics for the 110 mph case and reveals the drastic difference between the unpainted and painted model lift. The abrupt stall condition that occurs in the lift of the unpainted model is the most prominent difference. Although the results indicate that the lift is on average 22% lower for the painted model up to the stall point, the lift slope stays relatively constant while the lift of the unpainted model experiences the abrupt stall event. In turn, the large decrease in lift produced by the stall causes the post-stall lift of the painted model to be 20% higher than that of the unpainted model. Notably, the CFD results agree very closely with the painted model data, for both the turbulent and laminar flow cases.

Lift Coefficient Vs. Angle of Attack - 110 mph
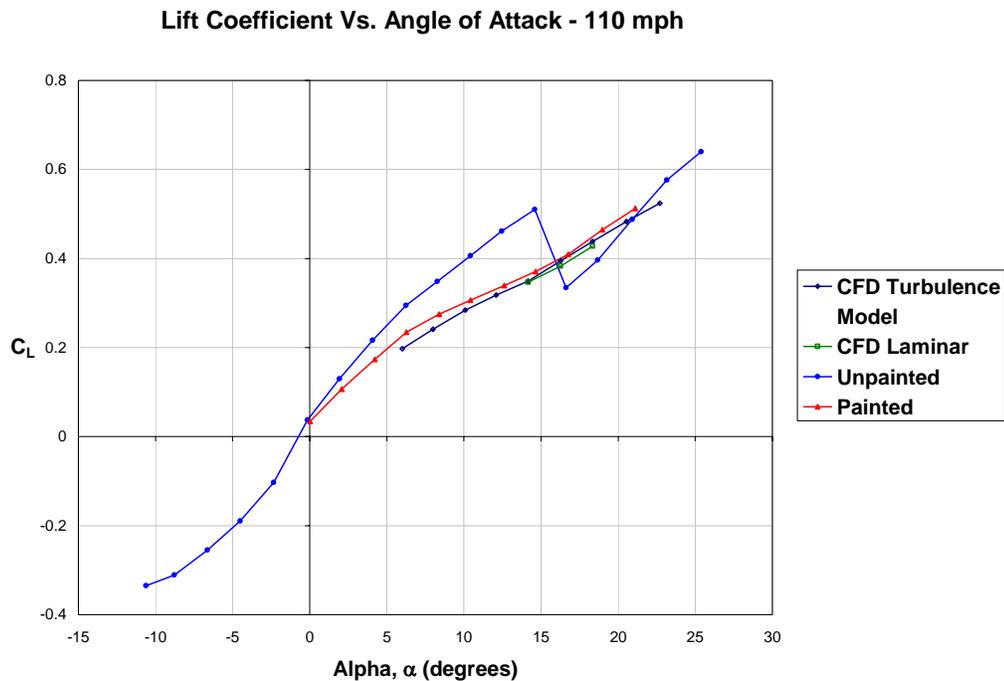
Figure 40: Painted/unpainted model lift comparison at 110 mph, with CFD.

Similar characteristics are seen in the drag coefficient. As seen in Figure 41 below, the drag coefficient of the painted model is lower at small angles of attacks than the unpainted model and higher at angles of attack above where the stall event. However, because of the unpainted model's abrupt decrease in drag due to an apparent reduction of induced drag, and the fact that the painted model has a steady drag curve, the two converge once again above 20 degrees angle of attack. Also evident is the CFD agreement with the painted model data, although the CFD predictions for both the turbulent model and laminar simulations are slightly higher at low angles of attack and lower at higher angles of attack.

Drag Coefficient Vs. Angle of Attack - 110 mph
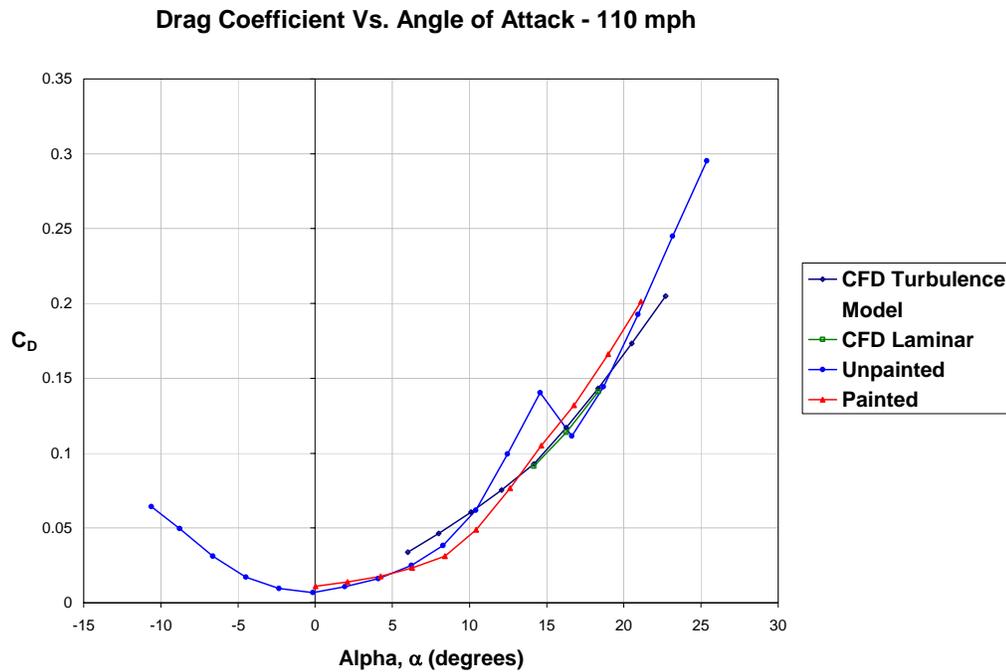
Figure 41: Painted/unpainted model drag comparison at 110 mph, with CFD.

The drag polar and lift-to-drag ratios comparing the unpainted and painted cases are given in Figure 42 and Figure 43 below. The representation of the unpainted model

data shows two obvious areas of efficiency in the stall area as seen in Figure 42 below. The painted data follow as it did in previous figures as it agrees with the unpainted data at first with a 60% increase in the minimum drag due to an increase in skin friction drag. The painted model data then follows a generally constant slope while less efficient, and crosses over to become more efficient than the unpainted model when it reaches the stall point. Once again, the CFD data is in agreement with the painted model lift and drag measurements although there is a minimal variation at the lower lift and drag values due to the resolution limitations of the smaller drag measurements.

Lift Coefficient Vs. Drag Coefficient - 110 mph
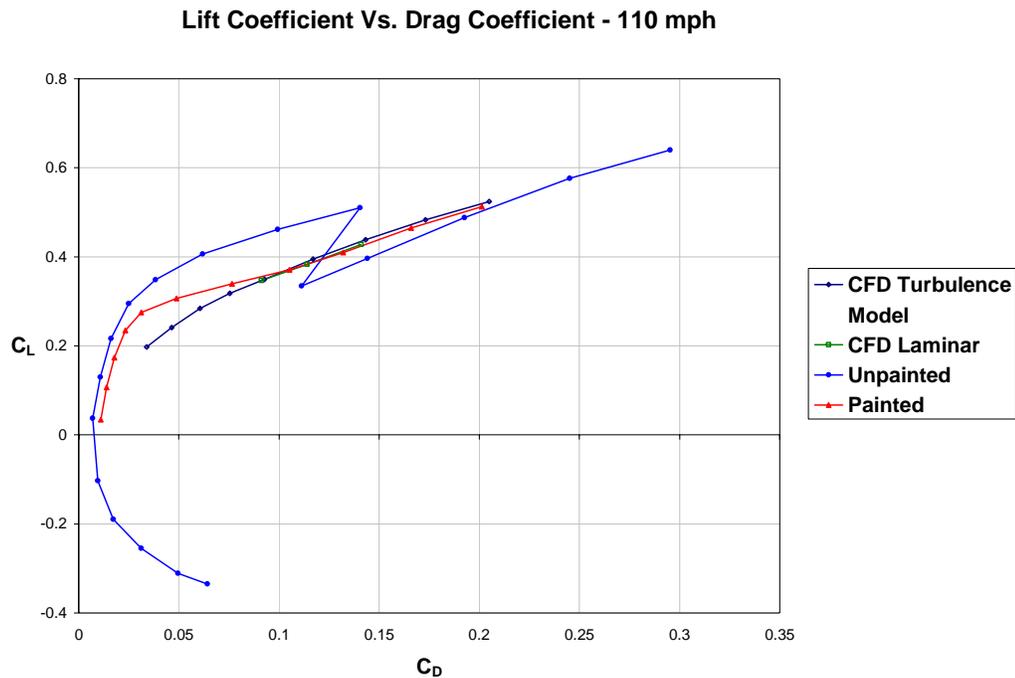
Figure 42: Painted/unpainted model drag polar comparison at 110 mph, with CFD.

As seen in Figure 43 below, the peak efficiency of the painted model at low angles of attack is 24% lower than that of the painted model. It is also noted that the maximum L/D for the unpainted model occurs at an angle of attack of 4 degrees, while

the painted model maximum L/D occurs just above 5 degrees. At angles above 8 degrees, there is much agreement between the two, and although the turbulent CFD results do not match prior to 12 degrees angle of attack, there is close agreement beyond this point. The discrepancies between the CFD data and the balance data are due to the resolution of the balance measurements of the drag forces at low angles of attack. At these lower angles. The measured drag forces are quite small, and there is potentially more error in these values. The CFD measurements were all carried out at the same resolution without accounting for the balance and sting effects seen in the wind tunnel.

Lift to Drag Ratio Vs. Angle of Attack - 110 mph
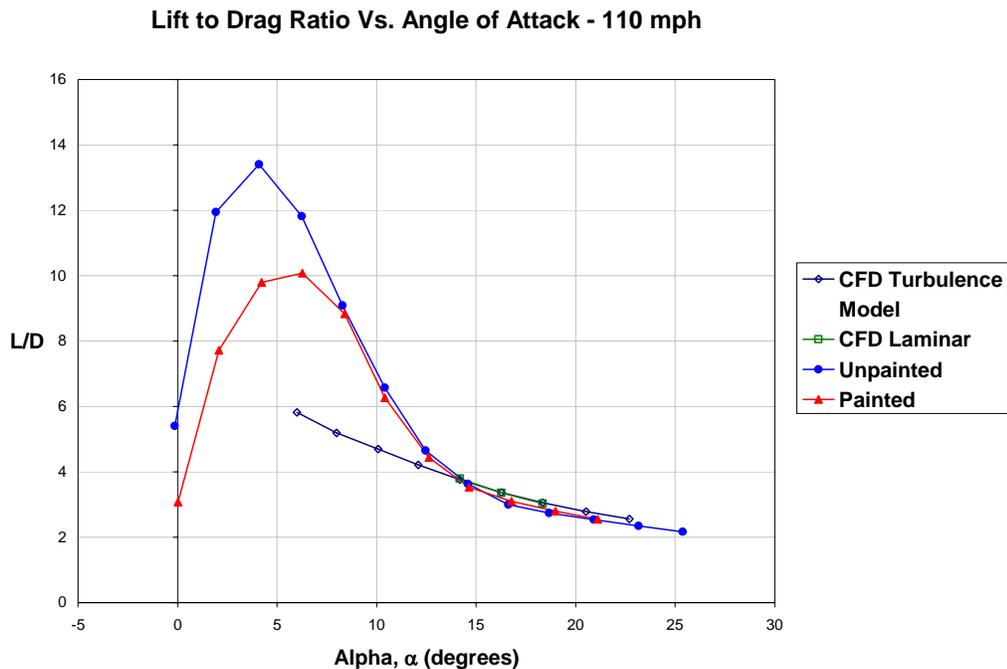
Figure 43: Painted/unpainted model lift-to-drag ratio comparison at 110 mph, with CFD.

Although no CFD pitching moment data was available, it does not detract from Figure 44, below, as it compares the painted and unpainted coefficients at 110 mph. This graph is also quite distinct in showing that there is a stability issue for the unpainted

model in the abrupt stall region. As seen in below, the slope of the C_M vs. α curve for the

painted model is generally constant as it deviates from the unpainted data well prior to

the stall region and continues through it to join the data again in the post-stall region.

This evidence further emphasizes the differences seen in the aerodynamic characteristics

of the painted and unpainted models. Specifically, the pitching moment stability was

drastically improved by the addition of the paint. This change is evident in the removal

of the sharp increase in the pitching moment at 15 degrees between the two models. The

steady slope of the painted model also shows the improvement in longitudinal stability.
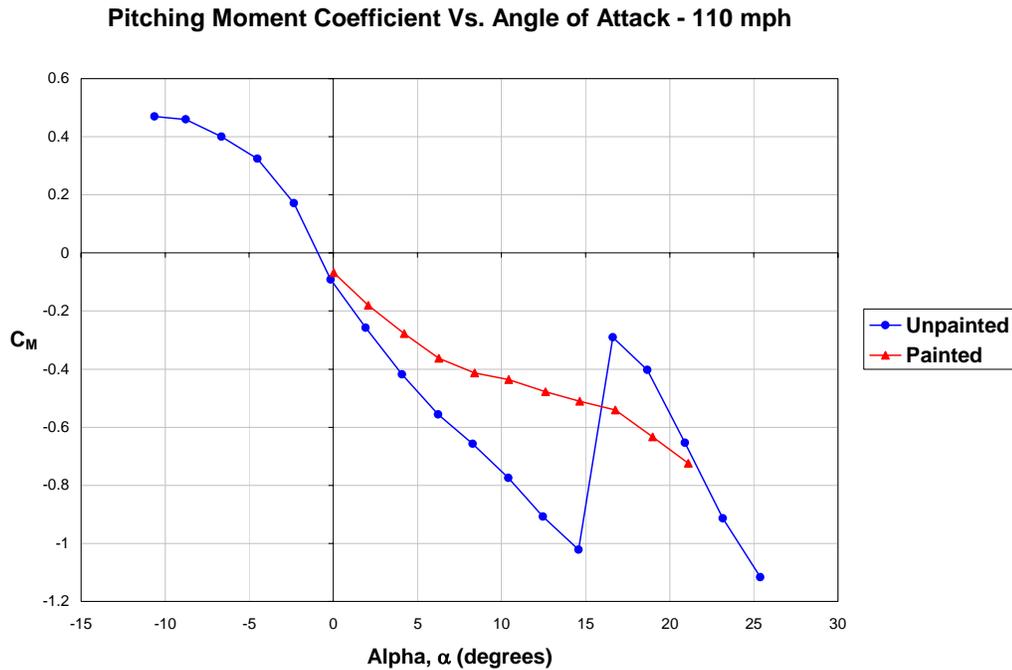
Figure 44: Painted/unpainted model pitching moment comparison at 110 mph.

The differences in the two models as mentioned above is seen in the data for the

test performed at 145 mph just as it was evident in the 110 mph data. The same grouping

of five figures will illustrate these differences, starting with the lift characteristics shown

in Figure 45 below. As seen, the painted model does not experience the sudden stall that the unpainted model does, but however sees a slight decrease in the lift curve slope during the region of stall, and then a slight increase nearly returning it to its original slope. The 110 mph cases showed that the painted curve exhibited slightly lower lift prior to stall and higher values after. In the 145 mph tests the pre-stall lift was only 15% lower on average. However, in this case the lift of the painted model is about 10% lower than that of the unpainted model throughout the majority of the post-stall region.

Lift Coefficient Vs. Angle of Attack - 145 mph
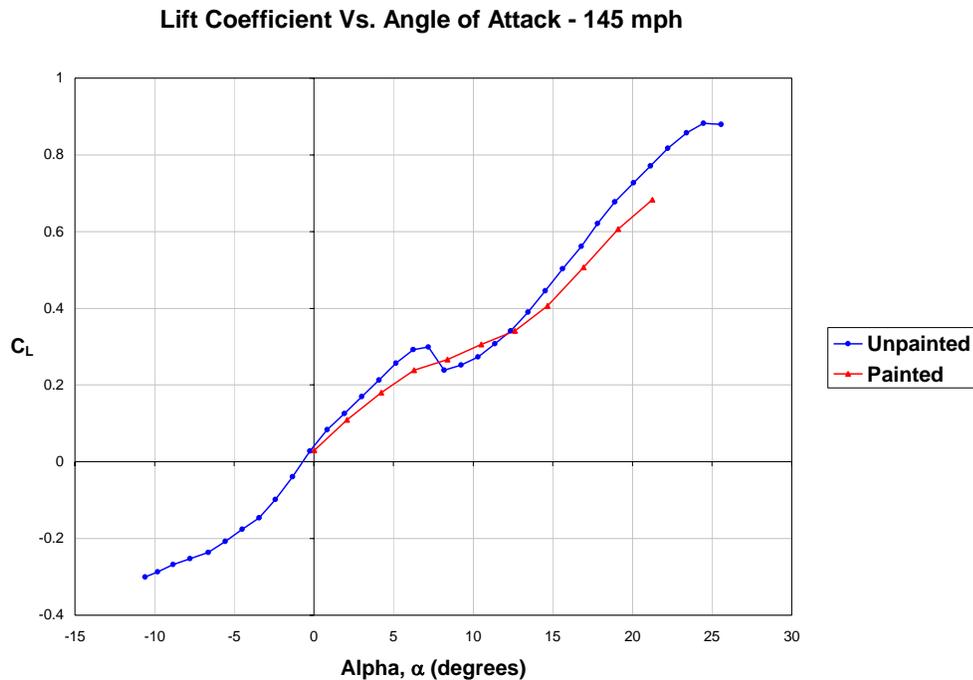
Figure 45: Painted/unpainted model lift comparison at 145 mph.

In all of the like cases, the trends found in the lift data occur in the drag data as well, with this 145 mph case being no exception. As seen in Figure 46 below, the painted model drag is slightly higher at first with a steady slope, and during the region of the unpainted model stall, the slope slightly decreases. Then again, the slope increases after

the stall region, and agrees with the unpainted drag until about 12 degrees angle of attack, at which point the drag curve continues to increase with a similar slope just under the values calculated.

Drag Coefficient Vs. Angle of Attack - 145 mph
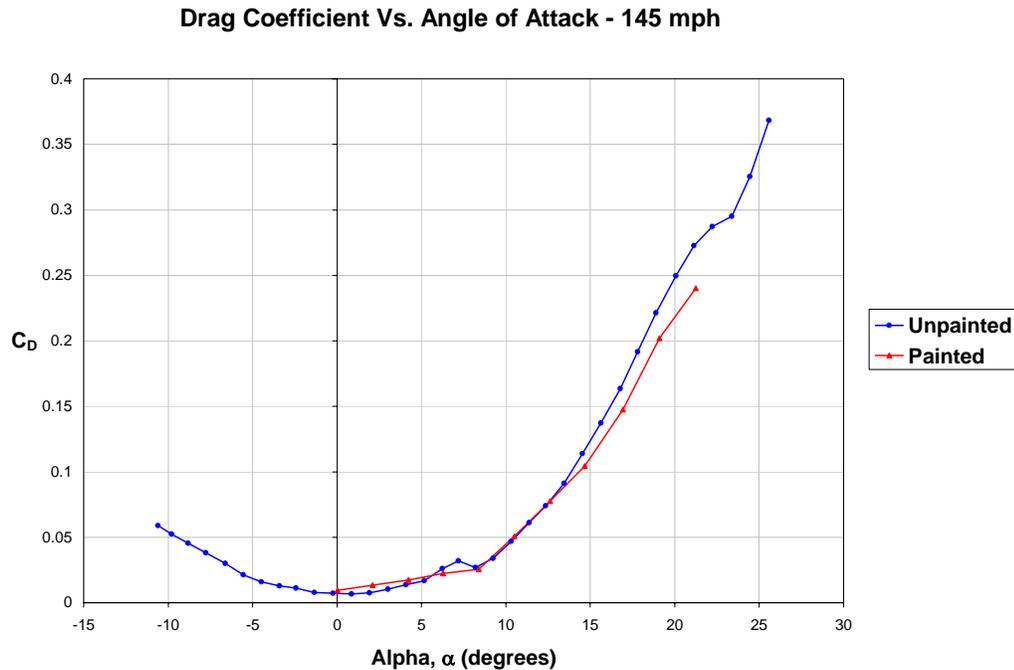
Figure 46: Painted/unpainted model drag comparison at 145 mph.

The data comparisons of lift and drag and their efficiency for the 145 mph case reveal similar trends to the 110 mph test as seen in Figure 47 below. There is a 50% increase in the minimum drag of the painted model over the unpainted due to the apparent increase of skin friction drag caused by the application of the PSP. Although the painted model is slightly less efficient than the painted model in the pre-stall region as in the 110 mph case, the post-stall efficiency is only higher for a moment before it drops below that of the unpainted model as seen in the post-stall region of the lift curve.

Lift Coefficient Vs. Drag Coefficient - 145 mph
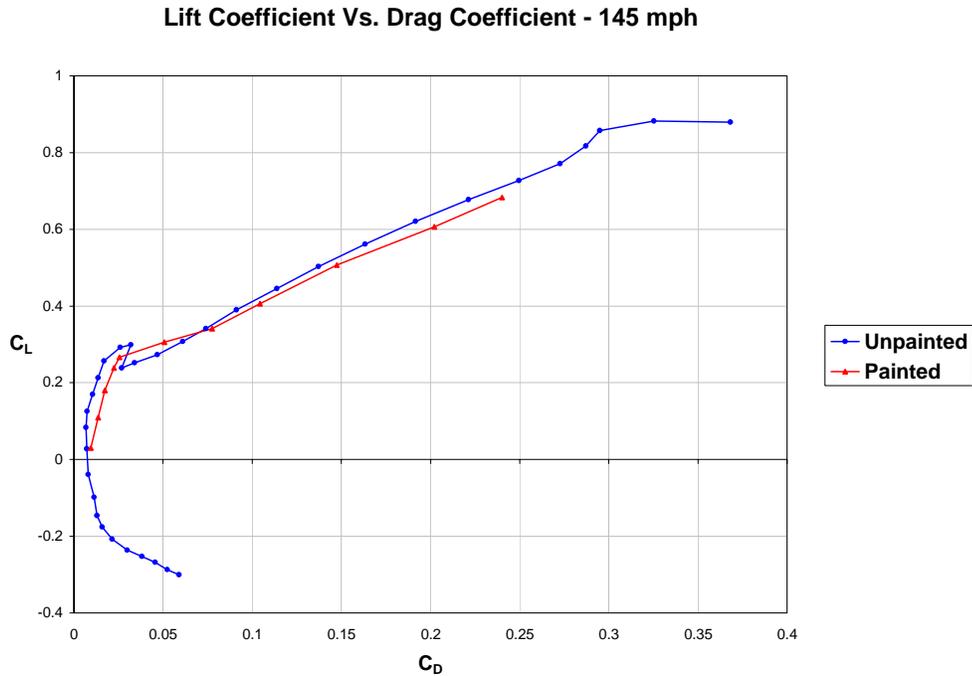
Figure 47: Painted/unpainted model drag polar comparison at 145 mph.

The next two figures show the same trends found in the 110 mph comparison. For the lift-to-drag ratio comparison in Figure 48, painted model exhibits a 37% decrease in the peak lift-to-drag ratio from that of the unpainted model at low angles of attack. Again, an angle of attack shift for the peak lift-to-drag ratio was seen between the painted and unpainted models. In this case, the unpainted model ratio peaked at 2 degrees angle of attack while the painted model ratio peaked at 6 degrees. The two curves align above an angle of attack of 10 degrees for this case as well. Figure 49 below shows that in the case of the pitching moment coefficient, the painted model data has a more constant slope than the unpainted model. The data for the 145 mph case follows previous trends in that the more stable pitching moment improves overall stability of the aircraft shown by the steady slope of the pitching moment coefficient for the painted model.

Lift to Drag Ratio Vs. Angle of Attack - 145 mph
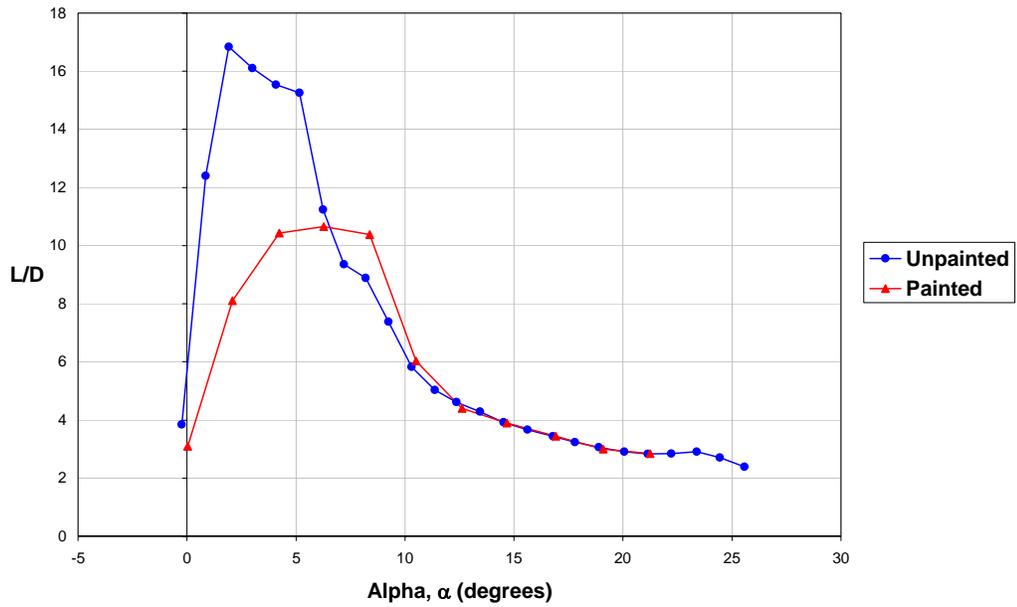
Figure 48: Painted/unpainted model lift-to-drag ratio comparison at 145 mph.

Pitching Moment Coefficient Vs. Angle of Attack - 145 mph
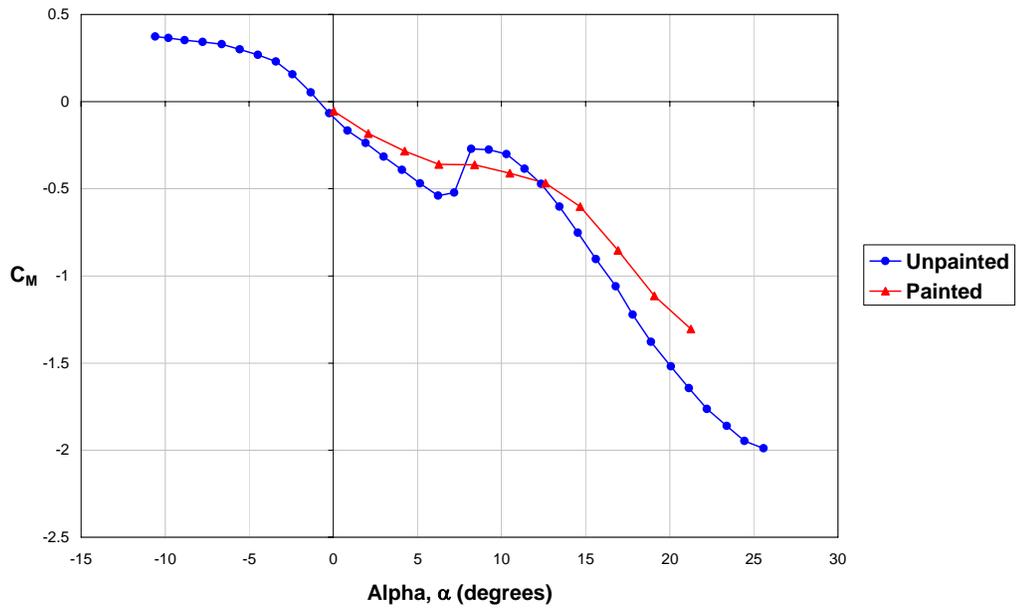
Figure 49: Painted/unpainted model pitching moment comparison at 145 mph**.**

Section 1.2 – Pressure Data

The following sections contain images of the PSP measurements obtained using the method described in Chapter III above, as well as the corresponding pressure tap data recorded during the PSP tests. The PSP data, reflected in the form of the images shown for each angle of attacked was obtained and processed using the procedure described in Chapter III. A final correction was applied using the data collected from pressure taps within the field of view. More details related to the pressure tap readings and their comparisons to the PSP data for determining the correction are given after the presentation of the PSP data itself.

Section 1.2.1 – Pressure Sensitive Paint Images

The PSP testing began with the 110 mph full view images from 0 to 20 degrees angle of attack, and then the 110 mph wing view images focusing on the stall region between 14 and 18 degrees. Figure 50 and Figure 51 below show the 110 mph full view images created after the necessary pressure tap correction was applied. It is quite evident that the trends seen in the painted model data above are shown in the images. The overall pressure on the strike tanker body is shown to stay relatively constant throughout the angle of attack range, with a slight decrease in pressure at the higher angles. The focus is placed on the wings of the model as the changes in angle of attack modify the pressure distribution. The figures show that at 4 degrees angle of attack a transition line forms just behind the leading edge of the wing. This low pressure region becomes more defined up to 10 degrees when the low pressure begins to fade back into the wing-body junction. At 12 degrees, the thin region is gone and the only existing low pressure is on the junction, while the wings begin to stall, as shown by the even coloration at the ends.

70
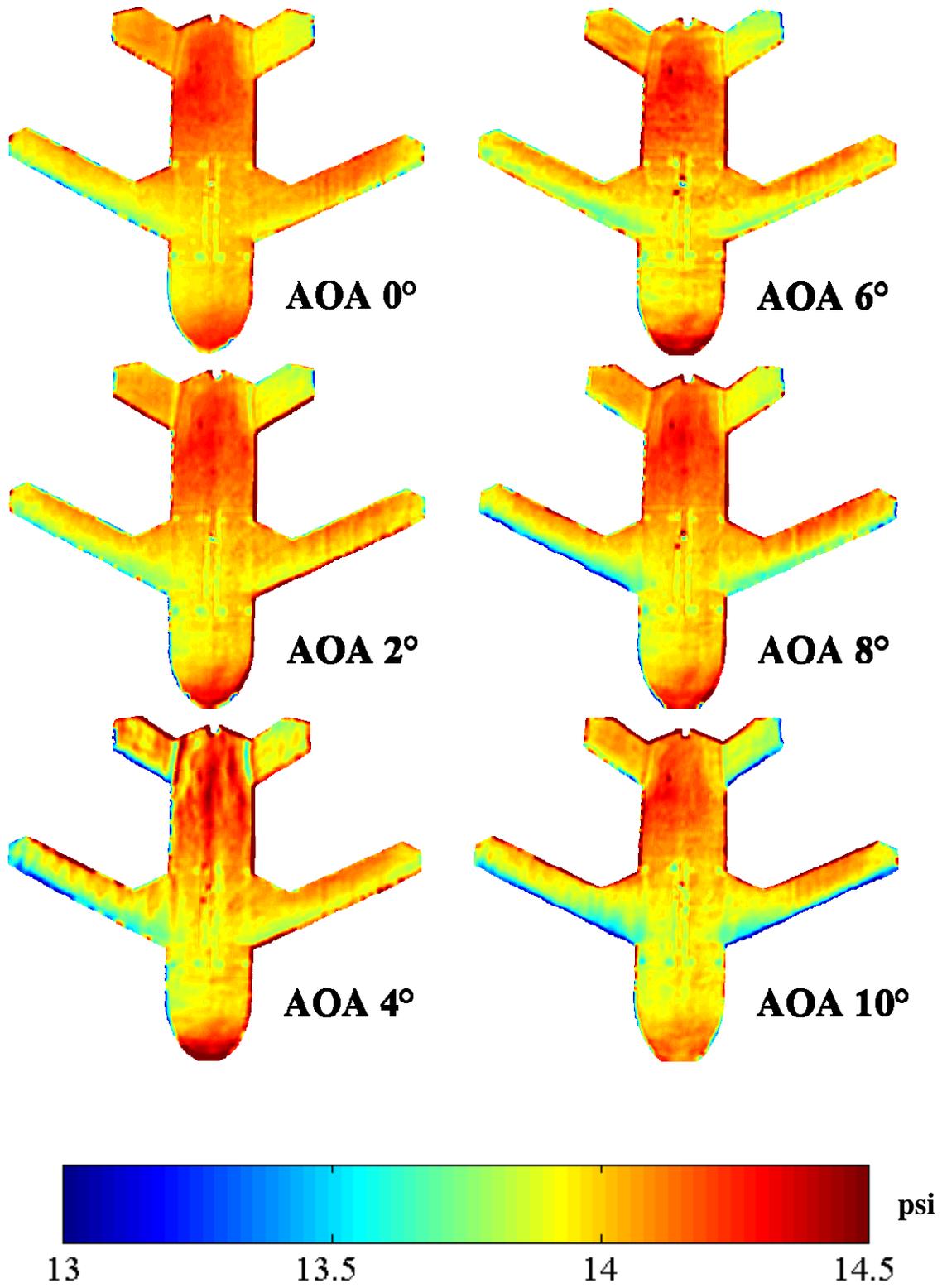
Figure 50: Full view PSP images for 0 to 10 degrees angle of attack at 110 mph.
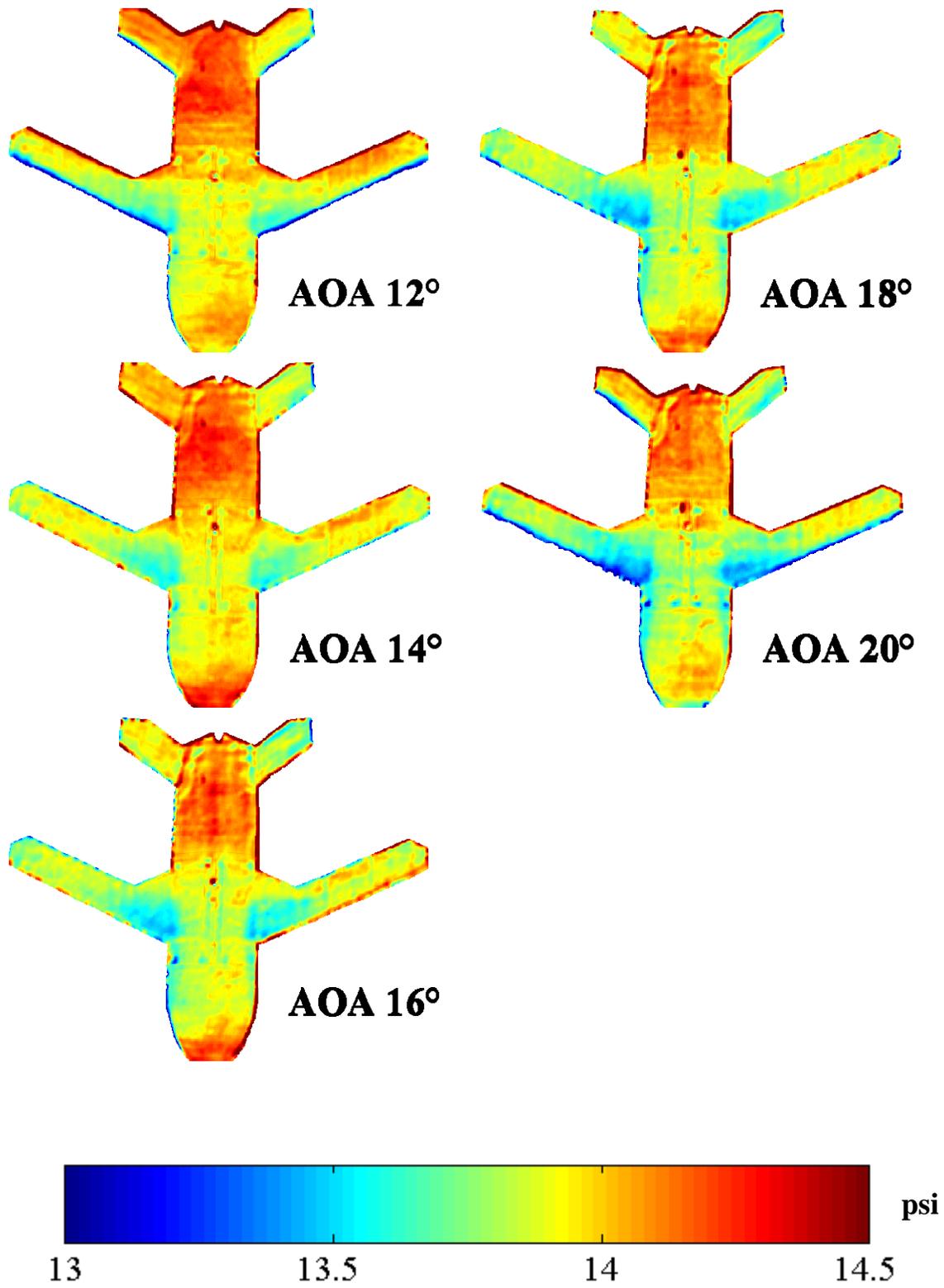
Figure 51: Full view PSP images for 12 to 20 degrees angle of attack at 110 mph.

The low pressure region near the wing-body junction becomes more defined as the angle of attack increases up to 20 degrees. At 16 degrees this pressure begins to decrease as well, through 20 degrees as will be seen in the pressure tap data following this section. The data of Figure 51 show a gradual increase in the pressure on the model wing with less and less variation across the span until it reaches a peak. At this point the pressure on the body starts to decrease around the wing-body junction, which corresponds to the gradual increase in lift through the stall region and beyond. The images agree quite well with the painted model force and moment data in that there is no evidence of an abrupt stall as seen on the unpainted model.

The force and moment data returned by the unpainted model runs sparked interest into the stall region, which lead to the investigation of this region using a close up view of just the model wing. The pressure contours of this particular experiment are shown below in Figure 52. Unfortunately there was a significant amount of interference picked up by the camera that was caused by the reflection of light off the camera. The evidence of this interference is shown by the arc and half circles of different shades in the middle of the wing. Outside the region of interference, the images still gave a reasonable representation of the same effects seen in the full view images. The images show that for the 14 and 15 degree cases, the wing pressure distribution is distinctly higher than that at the wing body junction. As the angle increases from 15 to 18 degrees, the overall pressure decreases, with the low pressure region becoming the most defined at 18 degrees angle of attack. This overall pressure decrease as mentioned above will also be reflected by the pressure tap data.

73

AOA 14°

AOA 17°

AOA 15°

AOA 18°

AOA 16°

psi

13   13.5   14   14.5
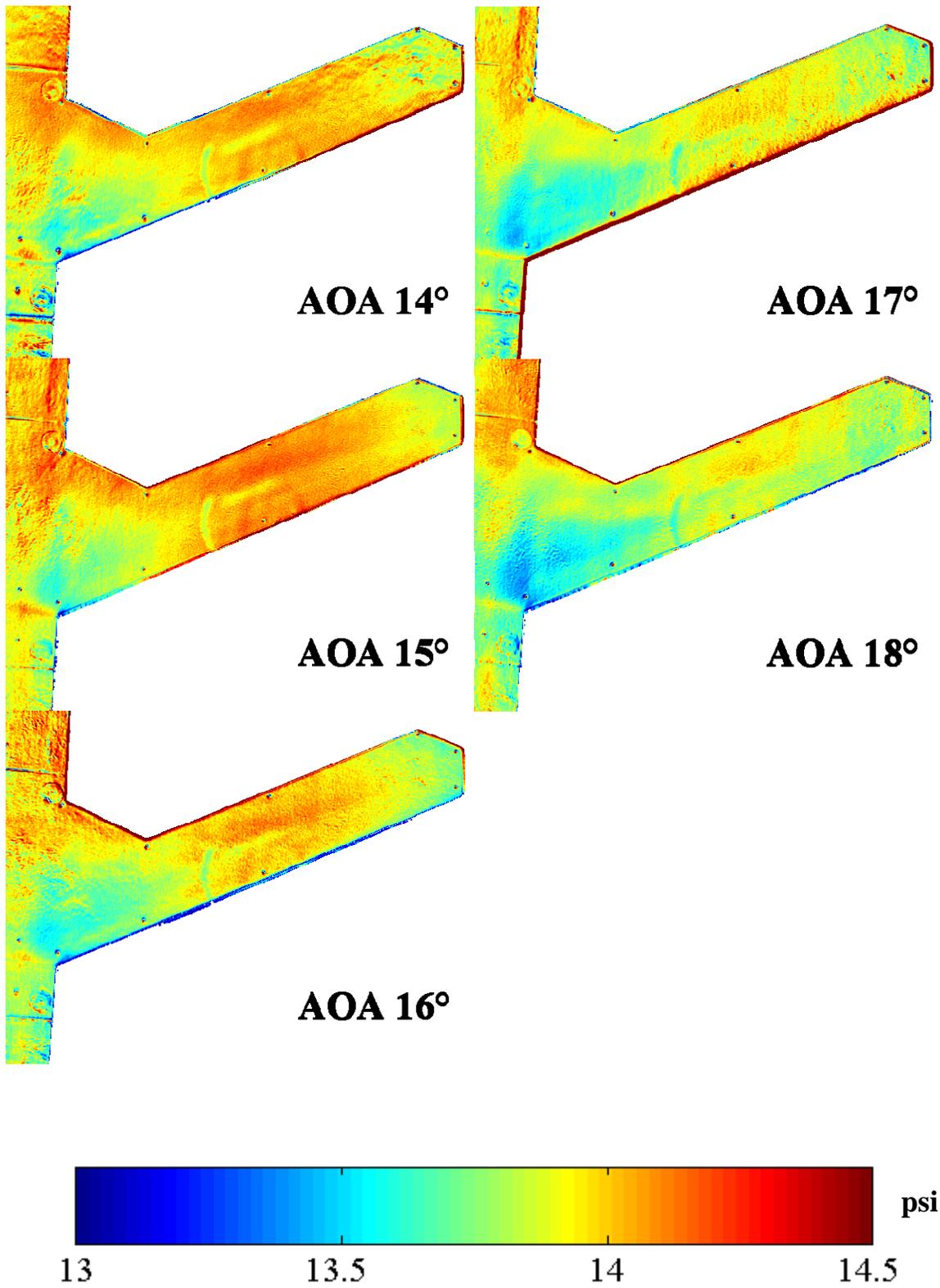
Figure 52: Wing view PSP images for 14 to 18 degrees angle of attack at 110 mph.

The PSP tests at 145 mph showed similar results to those at 110 mph, but yielded better results due to the increased air speed. The full view images were taken in the same 0 to 20 degree angle of attack range, however, for the 145 mph wing view images, the range of angles was set to 5 to 9 degrees to capture the stall region for that test speed. The PSP full view images of the 145 mph tests are shown below in Figure 53 and Figure 54. As for the 110 mph case, the trends seen in the force and moment data are seen in the PSP images as well, in that there are no abrupt changes, like a stall event, in the pressure distributions or in the lift curve slope. At $\alpha = 0°$, the distribution is relatively even across the entire model. In this case, for $\alpha = 2°$, a low pressure region forms just aft of the leading edge of the wing. As seen, the chordwise width of this region decreases gradually up to 10 degrees, and is absent after 12 degrees. At $\alpha = 8°$ a low pressure region is evident on the wing-body junction and expands in the aft direction and towards the center of the body as α increases to 20 degrees. This inward pressure shift is also evident in the pressure tap data presented in Section 1.2.2 below. Also shown by the images is what looks to be a vortex generation and subsequent low pressure line on either side of the aircraft nose, ahead of the wing.

Again, preliminary data lead to the investigation of the wing with close up PSP images shown in Figure 55 below. As in the 110 mph wing view case, the 145 mph test showed some interference caused by light reflection into the camera. Although there was less interference, a few discrepancies still exist in the image. For instance, images show a slight increase in overall pressure from 5 to 6 degrees; however, a gradual decrease occurs from 6 to 9 degrees. The low pressure line on the wing also diminishes and the low pressure region begins to form the at the wing-body junction in the $\alpha = 9°$ image.
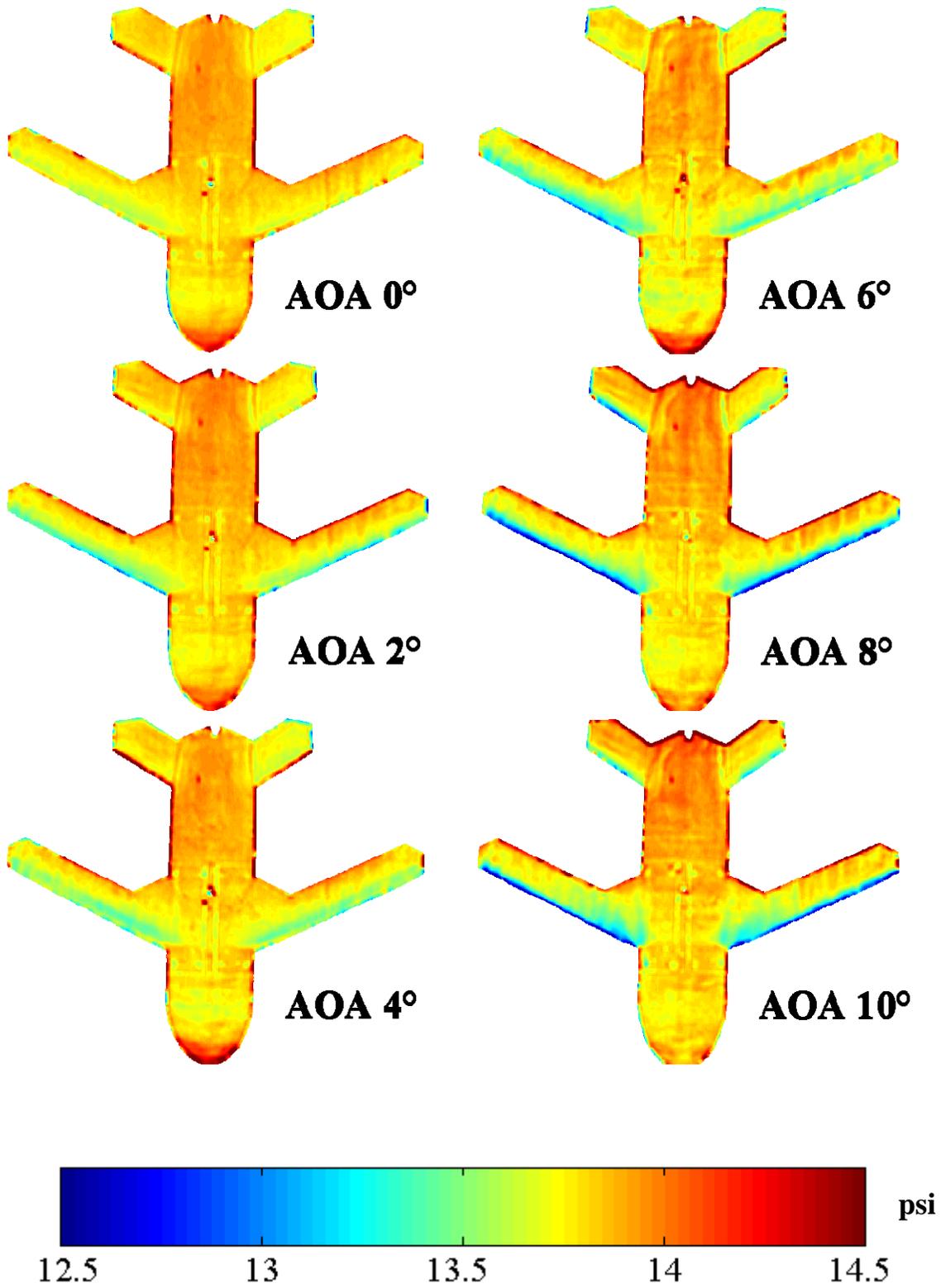
Figure 53: Full view PSP images for 0 to 10 degrees angle of attack at 145 mph.
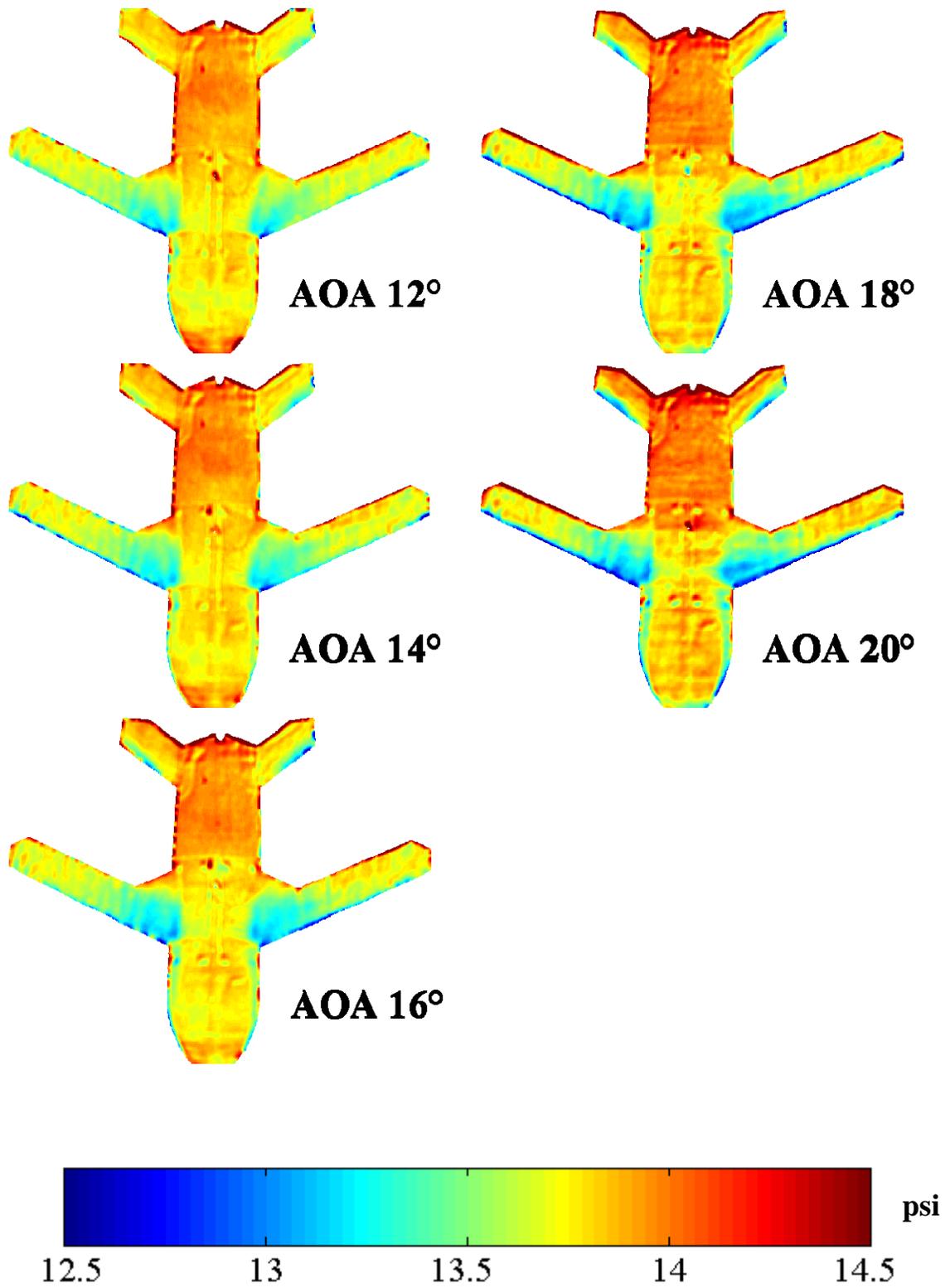
Figure 54: Full view PSP images for 12 to 20 degrees angle of attack at 145 mph.
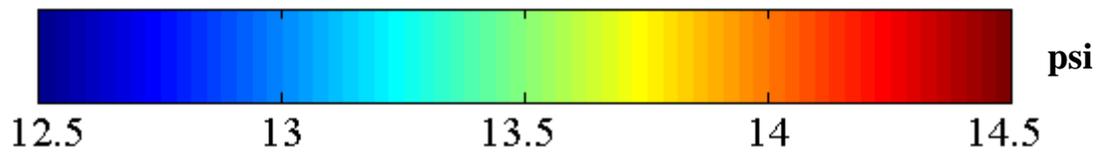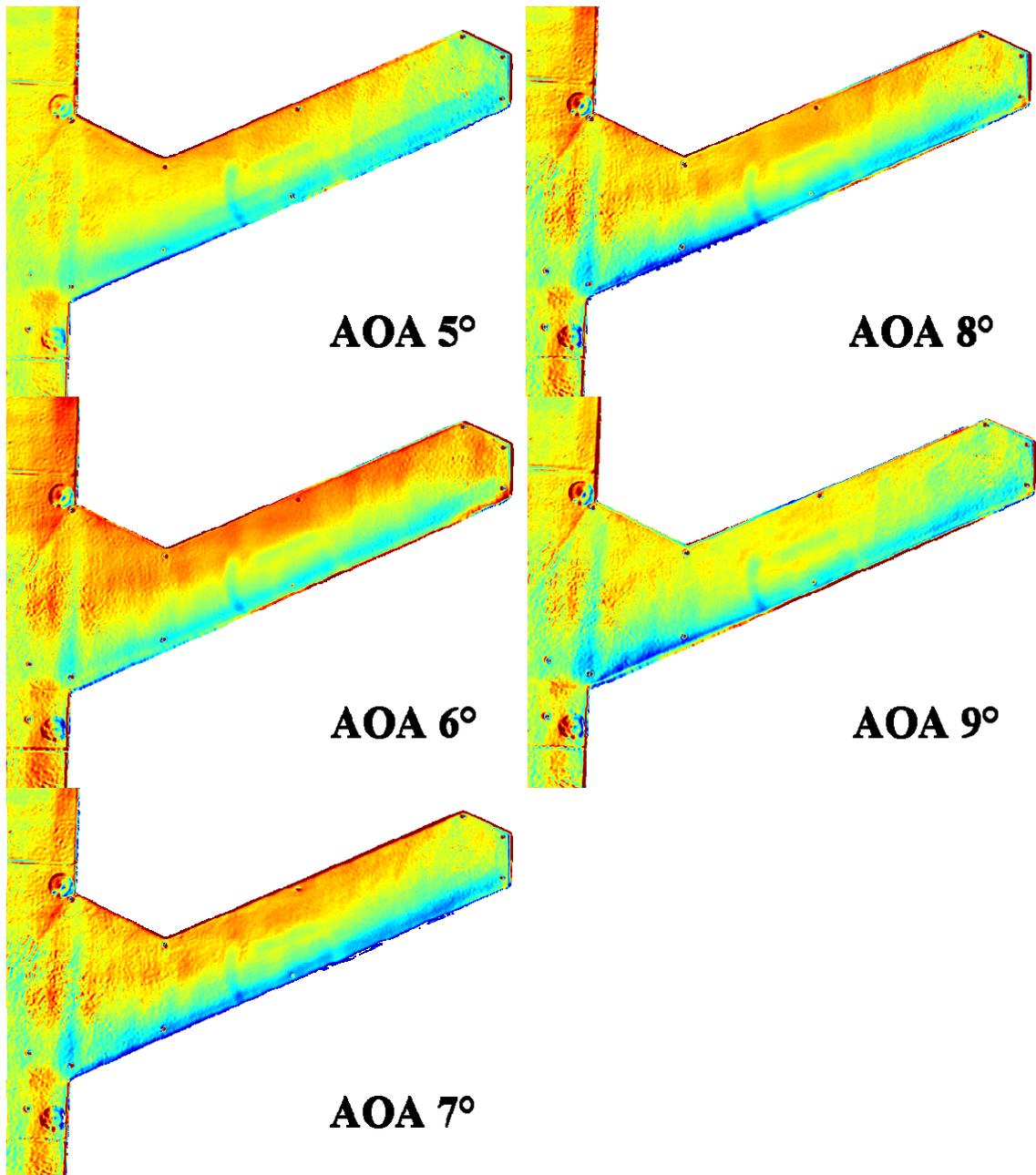
Figure 55: Wing view PSP images for 5 to 9 degrees angle of attack at 145 mph.

Section 1.2.2 – Pressure Tap Data and Comparisons

The strike tanker prototype was constructed with eight pressure taps built in, and these provided the important information necessary for the verification of the PSP data and the application of an in-situ calibration to each image. All of the pressure readings discussed are in units of psia. The system itself measured gage pressure; however the values were brought to absolute pressure by adding the atmospheric pressure on test day, in order to correlate with the PSP data. The first set of pressure tap data was taken during the full view 110 mph test. As shown in Figure 56 below, the range of values across all of the taps for any given angle of attack was less than 0.2 psi. These values were used as the actual values to which the values from the PSP images were compared. The legend shows which side of the model each tap was on and its location in respect to the center of the model. Symmetry existed with a 0.2% difference between the right and left taps.

Absolute Pressure Vs. Angle of Attack
Tap Reading - 110 mph
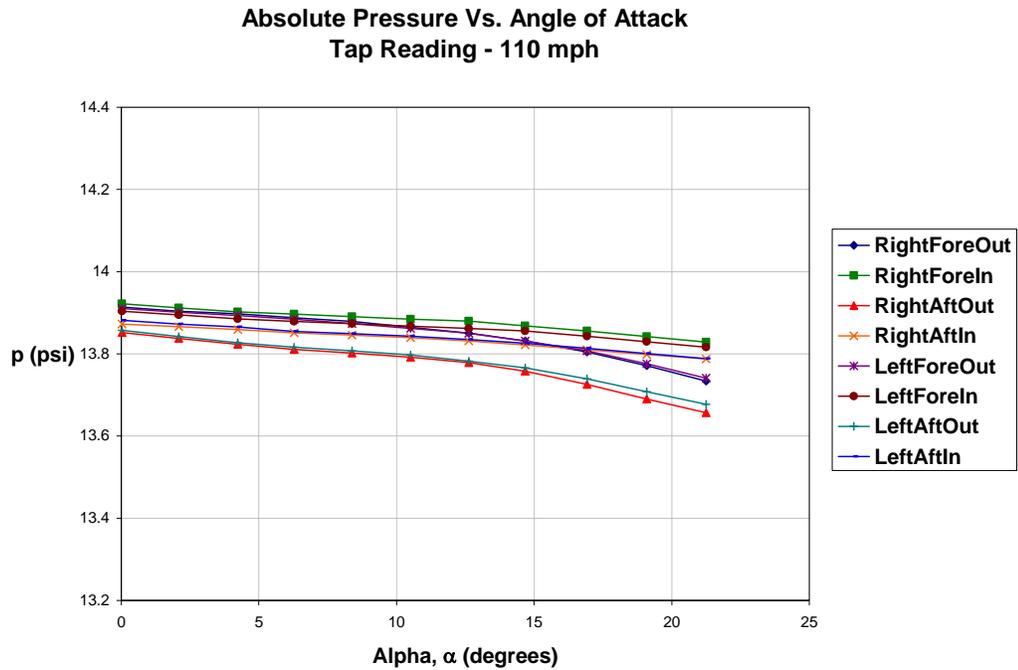
Figure 56: Pressure tap readings for the painted model at 110 mph.

Absolute Pressure Vs. Angle of Attack
PSP Reading - 110 mph
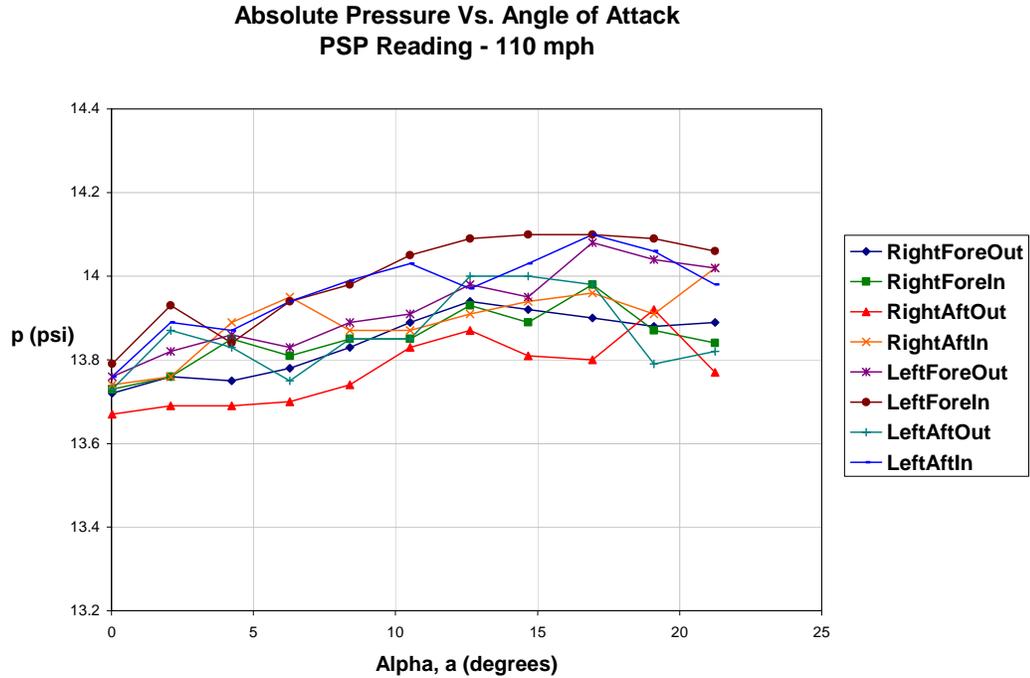
Figure 57: Pressure readings from PSP data at 110 mph.

The uncorrected PSP data measured in the proximity of each tap location for the full view 110 mph test are shown in Figure 57 above. As seen in the figure, all of the values fall within a range of 0.4 psi; however, the trend of these values is increasing. This is contrary to the tap data, which shows a decrease as angle of attack increases. The reason for this trend is unclear, though possible reasons include changes in background light levels as the model is repositioned, as well as photo-degradation of the paint. However, the latter is not viable due to the short testing times. Due to the fluctuations in the data within the range, the two most consistent data sets, RightForeOut and LeftForeOut, were chosen and the offsets from the pressure tap data were averaged to form a standard shift for the entire PSP test. A different shift value for each angle of attack was determined and the shift curve can be found in Figure 60 below.

The pressure tap data for the full view 145 mph test case exhibited a similar trend with a pressure range across all taps of less than 0.2 psi at 0 degrees angle of attack, and 0.25 psi at 20 degrees shown in Figure 58 below. As in the 110 mph test, symmetry was exhibited with a 0.3% difference between the right and left sets of taps.

Absolute Pressure Vs. Angle of Attack
Tap Reading - 145 mph
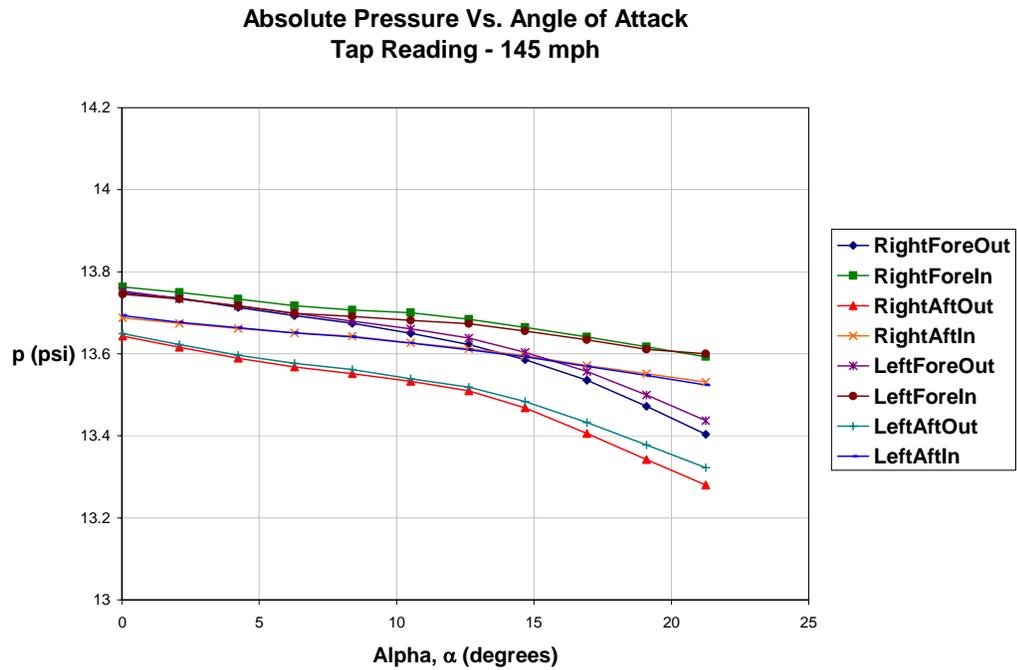
Figure 58: Pressure tap readings for the painted model at 145 mph.

The PSP data sets for the full view 145 mph test exhibit the same trend as the 110 mph case, again with slightly lower values. The values are shown in Figure 59 above and as seen, all of the values fall within a range of 0.4 psi. Because the trend of these values is increasing and the tap data decreases as angle of attack increases, a shift is needed again to correct the PSP data. As with the 110 mph data, many of the points exhibit large fluctuations within the range, therefore the RightForeIn point was chosen and the offsets

from the pressure tap data were used to form a standard shift for the entire PSP test. This

approach based on an in-situ calibration is common (6; 26).
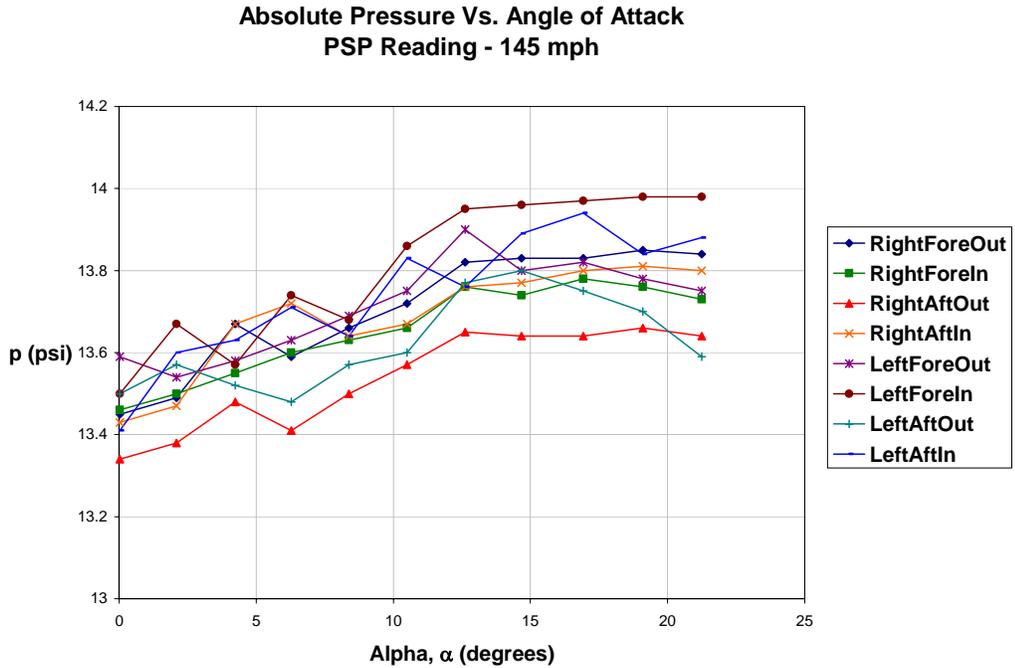
Figure 59: Pressure readings from PSP data at 145 mph.

The shift curves of the 145 mph data and the 110 mph data exhibit similarities

that show the accuracy of the PSP over two tests and are shown in Figure 60 below.

Although the PSP image pressure values are increasing, they actually start lower than the

tap measured values. Therefore, as seen below the shift starts as a positive shift and

continues with a negative slope to end up with a value to shift the images down.
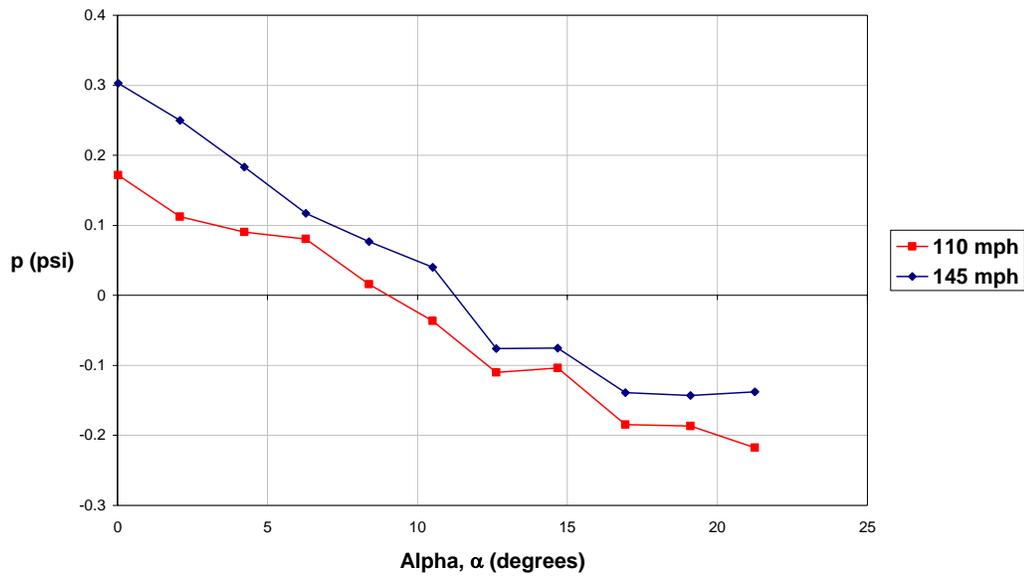
Figure 60: Pressure shift applied to correct PSP images.

The PSP images for the wing view test cases only contained two pressure taps. Therefore, the two left outside taps were used to correct the PSP data sets. As shown in Figure 61 above for the 110 mph test and Figure 62 below for the 145 mph test, the two different taps follow nearly identical trends with equal values between them for the tap and PSP measured pressures. The measured differences were then averaged for each of the tests in order to produce the shift needed to adjust the PSP images. In each of the figures, the shift was applied to the measured PSP data, and the corrected values, denoted by the underscore - c, plotted against the tap measured pressures.
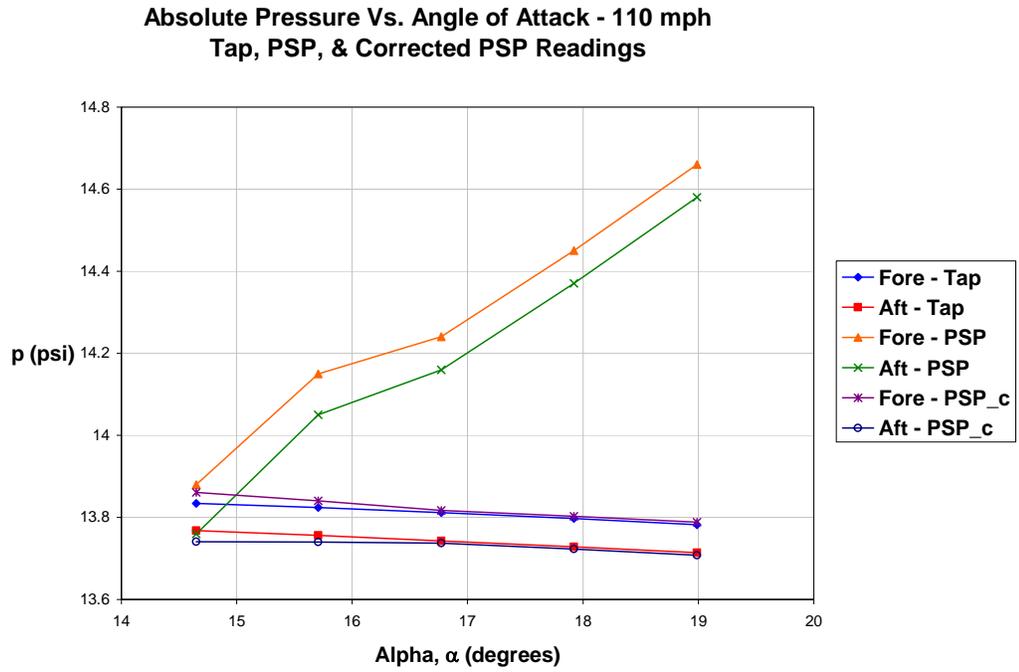
Figure 61: Tap & PSP pressure readings with corrected PSP values at 110 mph.
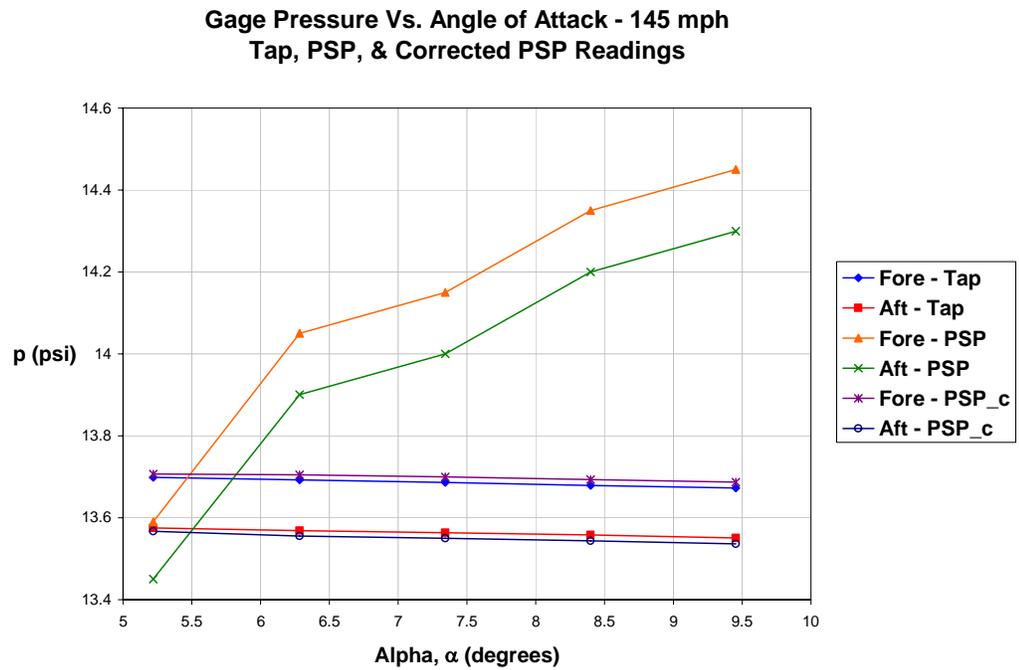
Figure 62: Tap & PSP pressure readings with corrected PSP values at 145 mph.

Section 2 – Surface Roughness Measurements

Many factors can influence wind tunnel test results from one run to another. One change, the application of paint, made to the strike tanker model has been used as a classification for different tests in previous sections. The application of the PSP to the model changed its characteristics, in particular, its surface finish. After all PSP tests were concluded, a small patch of paint was removed from the model using acetone in order to return the model surface to its original polished condition. A profilometer described in Chapter III, was used to measure the roughness of the unpainted region; these results are shown in Figure 63 below. A peak surface roughness (Rt) of 3.26µm was measured and the overall distribution of the roughness, measured over a test distance of 6mm, returned a mean rms roughness (Ra) of 0.32µm.
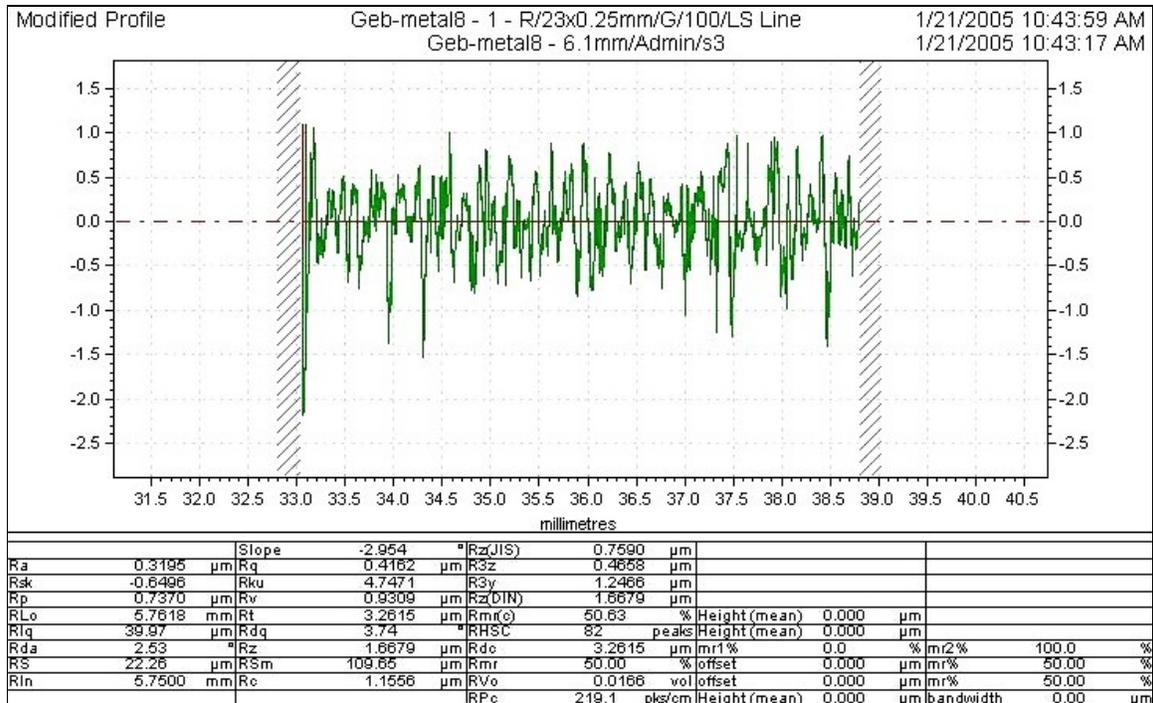
Figure 63: Unpainted metal surface roughness measurement.

In order to get an accurate and consistent measure of the paint roughness, measurements were taken in several spots. The two measurements of most importance were the center fuselage paint roughness and the wing paint roughness as shown below in Figure 64 and Figure 65, respectively. The Rt measured on the body was 6.814µm while the Ra was measured at 0.66µm. Similar results were seen for the roughness measured on the wing which returned an Ra of 0.62µm and an Rt of 6.51µm. Several additional profiles returned average values for Ra and Rt of 0.68µm and 6.98µm, respectively. Since two separate measurements at different locations on the painted model gave the same result, it was determined that the overall surface roughness was effectively doubled with the addition of the PSP. It should also be noted that the roughness data in Figure 63 through Figure 66 are given in different scales.
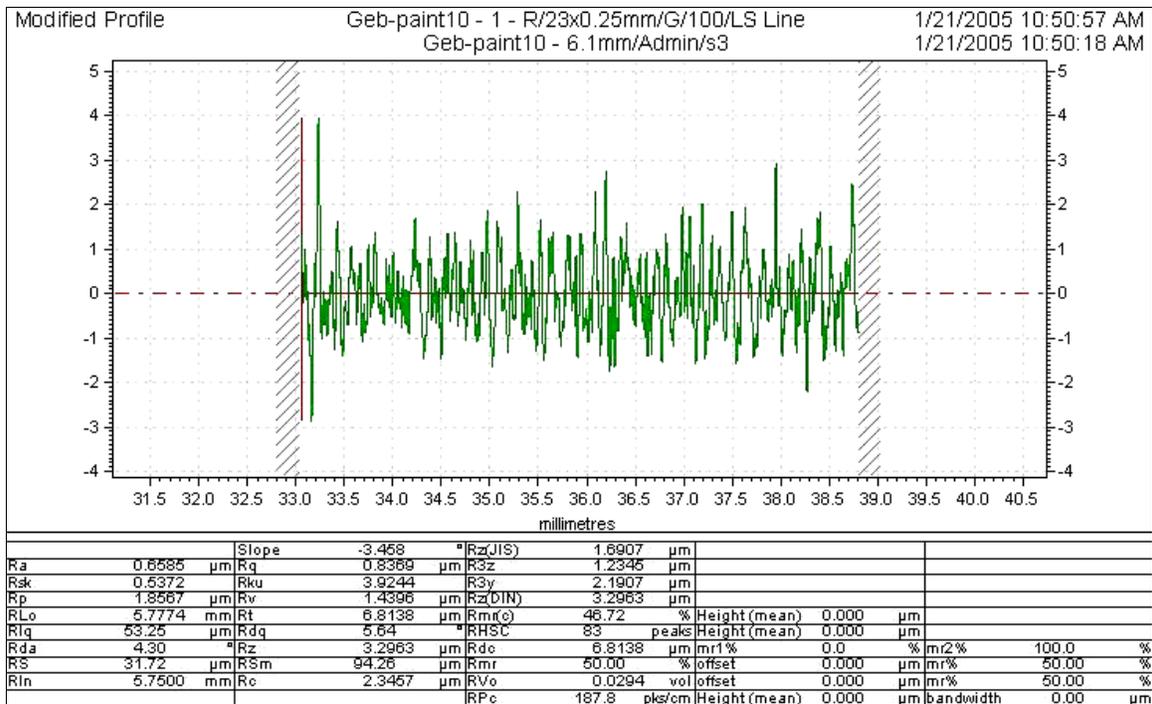
Figure 64: Painted body surface roughness measurement.

86
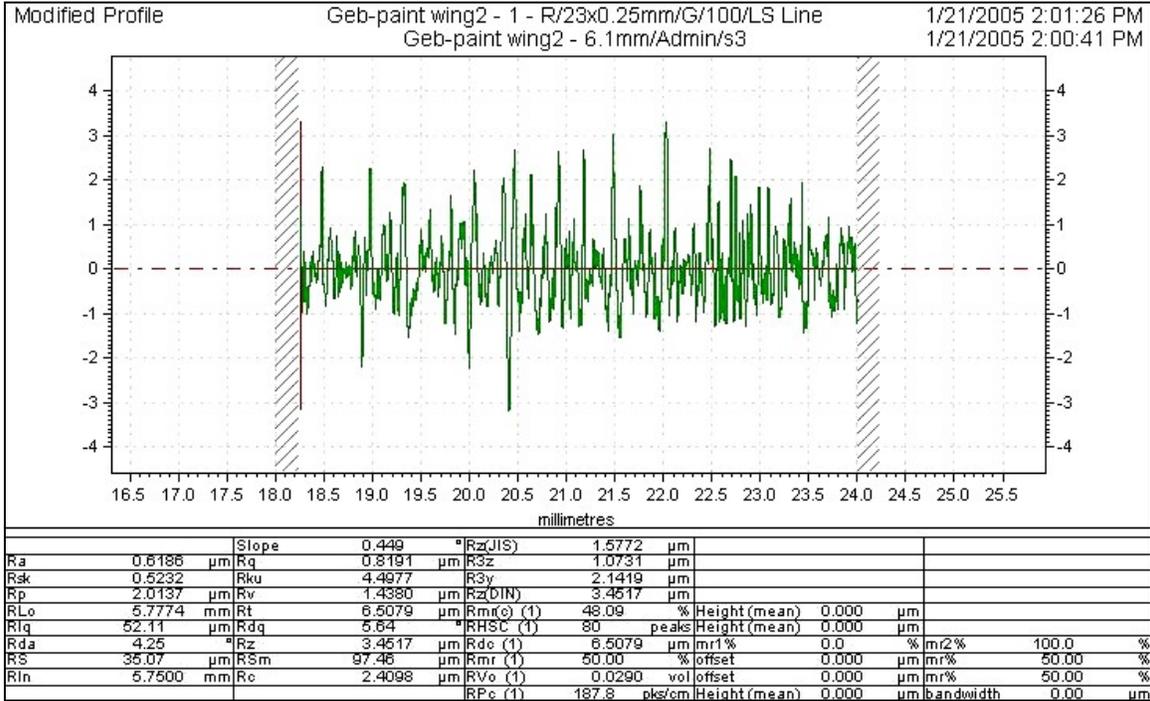
Figure 65: Painted wing surface roughness measurement.
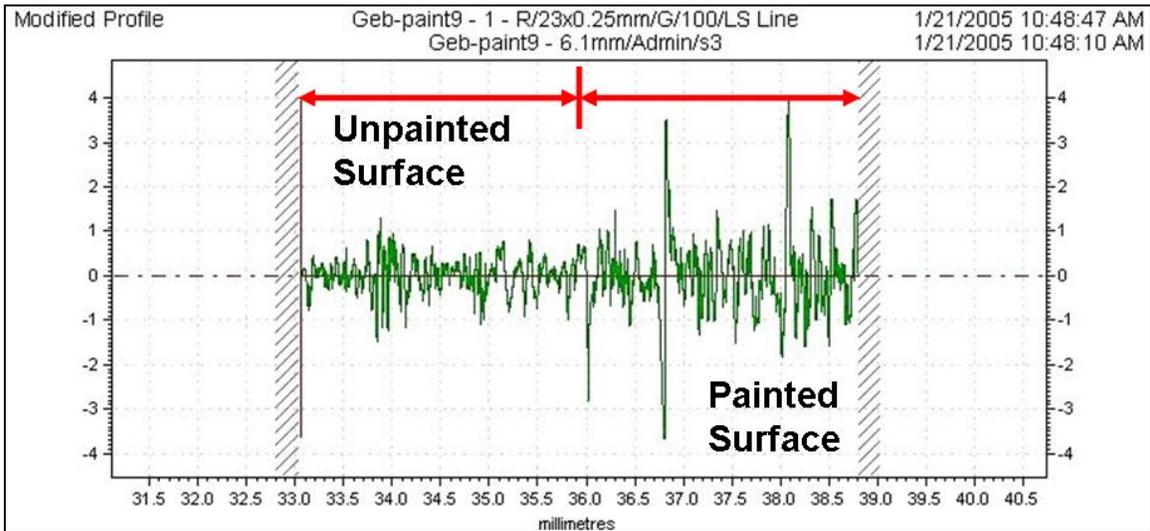
Figure 66: Unpainted surface to painted surface transition roughness measurement.

The roughness information in Figure 66 above illustrates a measurement that was taken across a metal-to-paint transition and effectively illustrates the increase in roughness from the metal to the paint. The overall results of the roughness measurements are best illustrated when compared to the reference studies using measured roughness as used by Schairer et al. and admissible roughness as defined by Schlichting in terms unit Reynolds numbers. This comparison is outlined in

Table **3** below, including the measured values of rms roughness and peak roughness height, Ra and Rt, respectively. This table shows that the admissible roughness guideline, using the relation $k_s = 6.2*Ra$ described by Schairer et al., worked well for his own experiments, in addition to those performed by Miklosovic et al at low Reynolds number. They found that a measured roughness below the admissible level did not affect the boundary layer transition. The remaining studies found effects at roughness values nearly two orders of magnitude lower than the expected value, based on admissible roughness. The table distinctly shows that the results of the measurements performed in this study agree with the studies in Ref. 17, 22, and 29 that found roughness effects for micron-level surface roughness parameters.

Table 3: Related surface roughness study parameters and results.

| Author/Study | Application | Reynolds # | | Roughness, microns | | | | Does it |
		Chord	Unit (m^{-1}) (Schairer)	RMS Ra	Peak Rt	Measured $k_s = 6.2 \cdot Ra$	Admissible $k_s = 100/Re_u$	Matter?
Schairer	smooth paint	3.30E+06	9.35E+06	0.5	10	3.1	10.7	No
high lift wing - 35 deg sweep	rough paint	3.30E+06	9.35E+06	1.5	20	9.3	10.7	
Vanhoutte	clean	3.70E+05	1.61E+06	1.04	11.07	6.4	62.2	
30 degree swept wing	PSP 1	3.70E+05	1.61E+06	2.29	39.47	14.2	62.2	Yes
	PSP 3	3.70E+05	1.61E+06	4.81	70.11	29.8	62.2	
	PSP 3	3.70E+05	1.61E+06	5.69	71.23	35.3	62.2	
Miklosovic	smooth	1.06E+06	2.99E+06	2		12.4	33.5	Yes
sailboat centerboard	rough	1.06E+06	2.99E+06	4		24.8	33.5	
	smooth	5.60E+05	1.58E+06	2		12.4	63.4	No
	rough	5.60E+05	1.58E+06	9		55.8	63.4	
Radeztsky	painted surface	2.70E+06	1.48E+06	9		55.8	67.8	
	machine polished	2.70E+06	1.48E+06	0.5		3.1	67.8	Yes
	hand polished	2.70E+06	1.48E+06	0.25		1.6	67.8	
Strike Tanker	unpainted model	1.80E+05	5.44E+06	0.32	3.26	2.0	18.4	Yes
with 25 degree swept wing	painted model	1.80E+05	5.44E+06	0.66	6.81	4.1	18.4	
						Schairer	Schlichting	

Section 3 – Yaw Angle Sweeps

The following section presents various data in terms of unpainted and painted force and moment data as in previous sections, as well as pressure tap measurements and full view PSP data. All of the experiments performed were based on variations of negative yaw angle, or beta, β. This nomenclature is common in aerodynamics as it appropriately relates to angle of attack, alpha. Therefore, the data presented in the following section will be discussed in terms of beta, and how the aerodynamic characteristics are affected by changes in this value.

Section 3.1 – Force and Moment Data

Section 3.1.1 – Unpainted Model

The data collected for the unpainted strike tanker model was taken using alpha sweeps at varied beta. Therefore, the figures below characterize the yawing effects on the lift coefficients as well as the rolling moment and yawing moment coefficients as they change with a decrease in beta (increase in yaw angle). Identical experiments were performed at representative air speeds of 90 mph and 130 mph, which allowed the visualization of any increased stall effects due to increased air speed, as seen in the unpainted model alpha sweeps.

The rolling moment coefficient is the first of the aerodynamic properties to be examined. As seen in Figure 67 below, the roll moment coefficient increases as beta decreases for each alpha. As expected, the rolling moment is quite stable and constant at $\beta = 0°$, and as beta decreases, the slope of each successive test case is slightly larger, continuing to $\beta = 16°$.

Rolling Moment Coefficient Vs. Angle of Attack
Unpainted - 90 mph
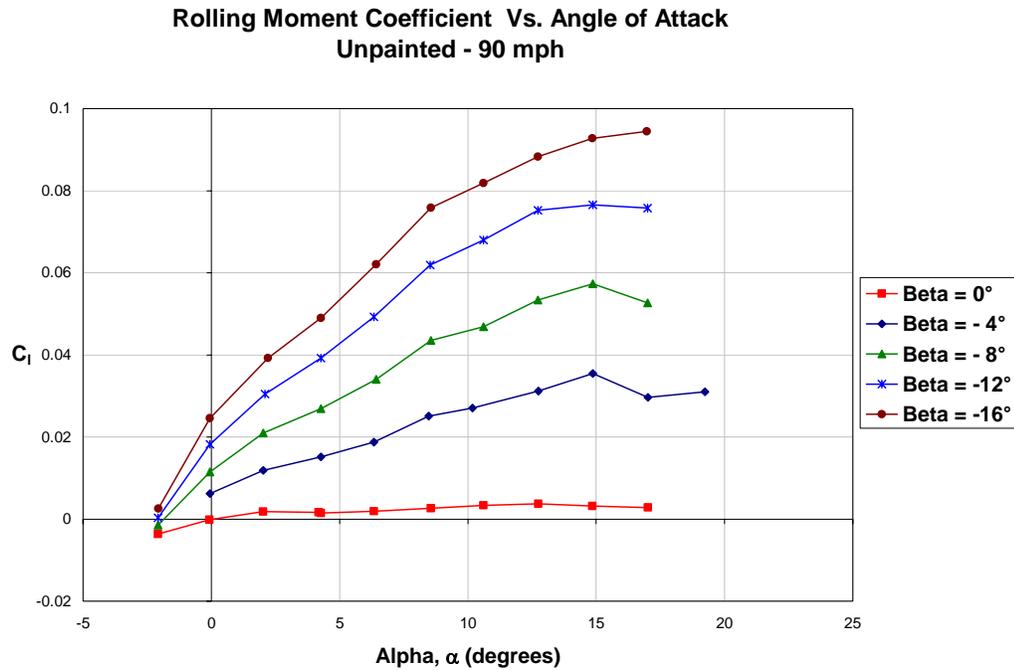
Figure 67: Unpainted model rolling moment comparison by beta at 90 mph.

In addition to the coefficient of rolling moment, the yawing moment coefficient is a vital parameter in indicating the directional stability of an aircraft, defined as a positive C_n versus β curve. Unlike the previous graph, Figure 68 below shows a number of issues associated with the yawing moment for the various betas as angle of attack is increased. At low alphas, the data resembles that of the graph above, with all of the different betas exhibiting similar trends. This is expected as C_n increases as β increases from -16° to 0°. However, the $\beta = 0°$ case shows a drop in C_n at 4 degrees, which is attributed to a spurious data point. The most important change in the data begins at $\alpha = 10°$ and continues through the range of data. The values for C_n begin to deviate from stable theory and exhibit abnormal behavior. As seen the values begin to cross over numerous times and the $\beta = -8°$, -12°, and -16° curves indicate a negative slope of Cn versus β. The

yaw moment coefficient is not well behaved at values of $\alpha > 6°$ and may be attributed to the abrupt stall event shown by the data in section 1.1.1.

Yawing Moment Coefficient Vs. Angle of Attack
Unpainted - 90 mph
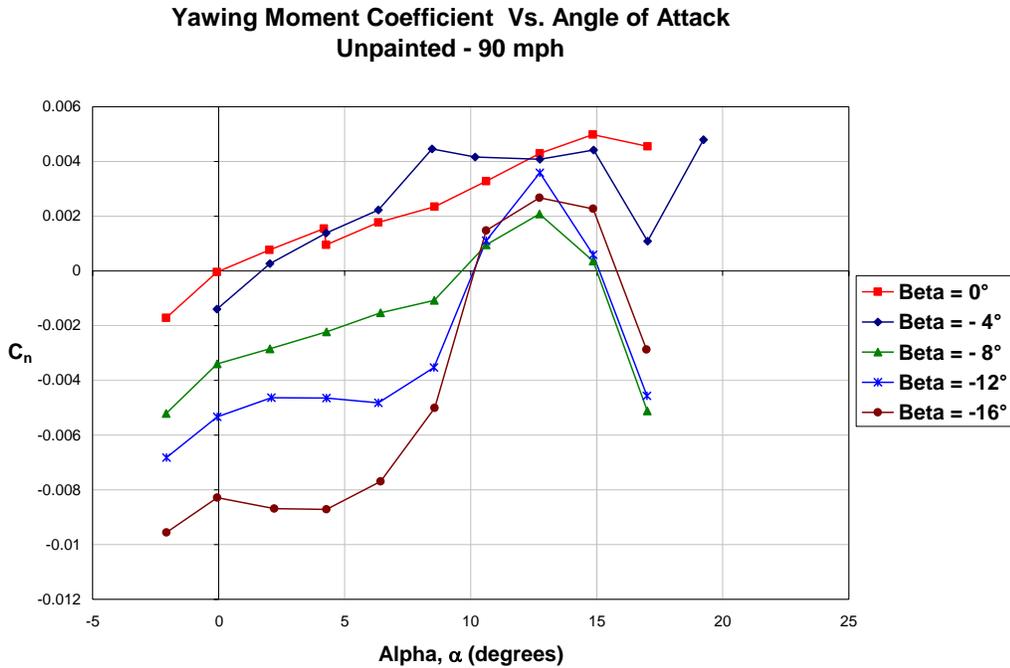
Figure 68: Unpainted model yawing moment comparison by beta at 90 mph.

The final beta run comparison focuses on the change in the coefficient of lift as angle of attack is varied for each of the beta angles. Figure 69 below shows the agreement of the measured lift curves and their slopes. With the exception of the angles of attack above 15 degrees, the coefficients of lift remain virtually equal and aligned for all the measured betas. This graph indicates that the overall coefficient of lift is in general, not a function of the negative yaw angle of the unpainted strike tanker model at 90 mph air speed.

Lift Coefficient Vs. Angle of Attack
Unpainted - 90 mph
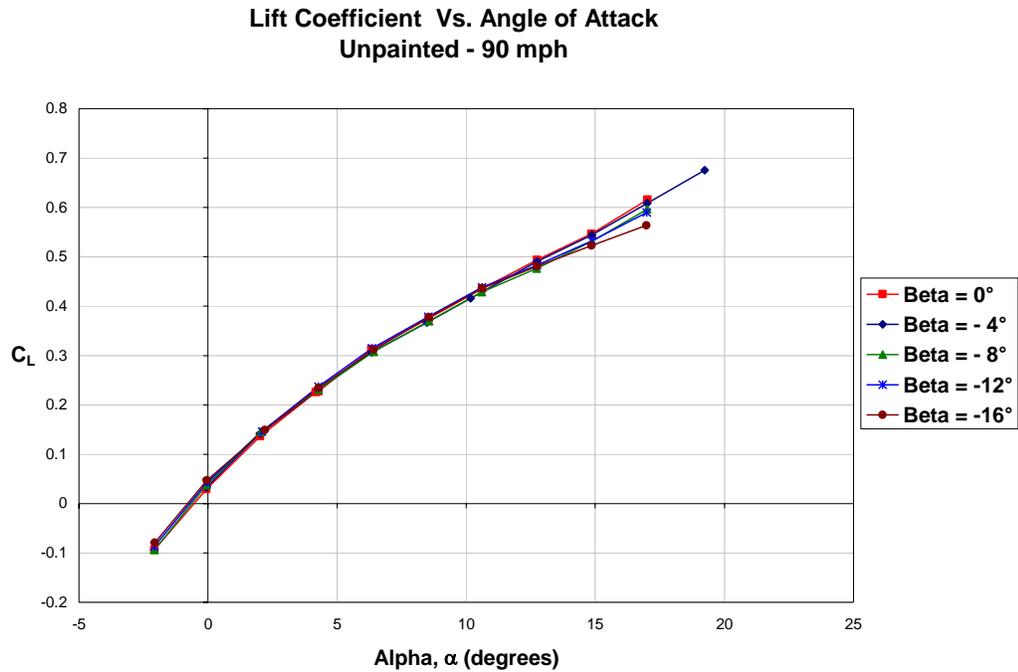
Figure 69: Unpainted model lift comparison by beta at 90 mph.

The same three methods used to describe the effects of beta on the rolling moment, yawing moment, and lift coefficients as they vary with angle of attack were used to evaluate the identical tests performed at 130 mph. As in the 90 mph case, rolling moment coefficient versus angle of attack data does not offer any striking information about the stability of the unpainted model. The main difference between the two data sets is shown in Figure 70 below in the form of an oscillatory pattern in seen for each of the beta angles. Although barely visible in the $\beta = 0°$ case, the concurrent pattern of the other beta runs suggests an underlying issue in the aircraft stability. Since the first shift in the slope occurs long before the stall event shown in the Section 1.1.1 data at this air speed, the moment oscillation cannot be attributed to that event and further investigation may be required.

Rolling Moment Coefficient Vs. Angle of Attack
Unpainted - 130 mph
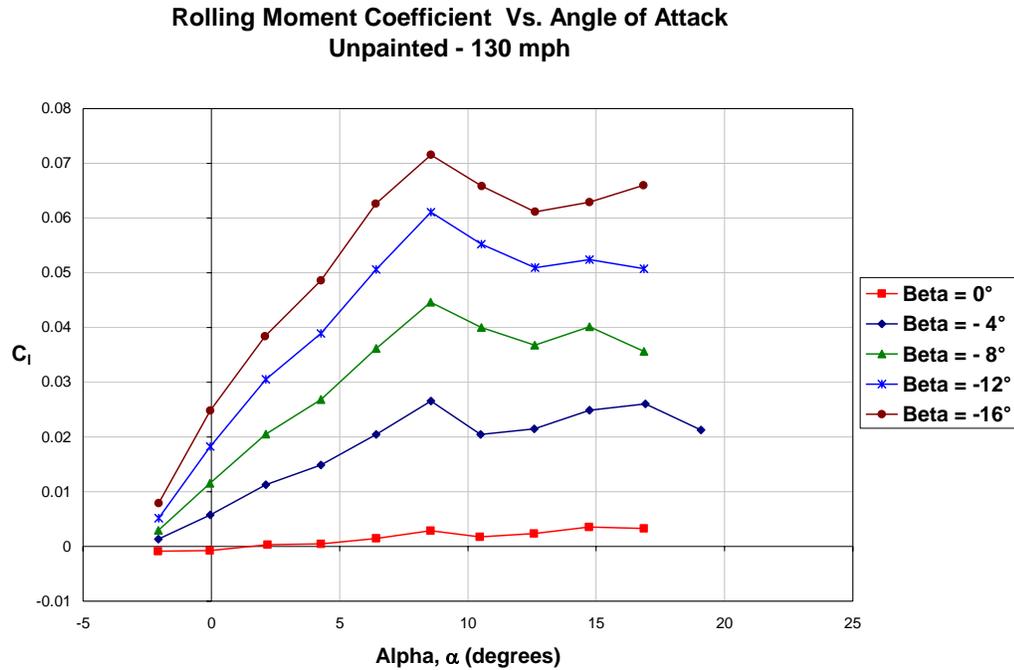
Figure 70: Unpainted model rolling moment comparison by beta angle at 130 mph.

Again, similar results are seen in the yawing moment coefficient versus angle of attack data as in the 90 mph case. Just as before, the low angle of attack values for all beta angles show good agreement with similar trends shown in the data slopes; however, for values of $\alpha > 5°$, there is once again evidence that the aircraft may experience problems with directional stability. Although the beta curves for the alphas less than 5 degrees show good directional stability, the same drastic change in the slope of Cn is seen in the 130 mph data that was seen in the 90 mph data. Again, the slope remains irregular after the high point at $\alpha = 11°$, which suggests that there may be an instability issue in the yawing moment and that the aircraft's natural aerodynamics. Unlike the 90 mph case, the confusion in this figure occurs very near the stall point as determined in Section 1.1.1. This contradicts some of the previous indications in this data in that the data for the 130

mph tests provide substantial evidence that the instabilities in the yawing moment occur

due to stall of the aircraft.
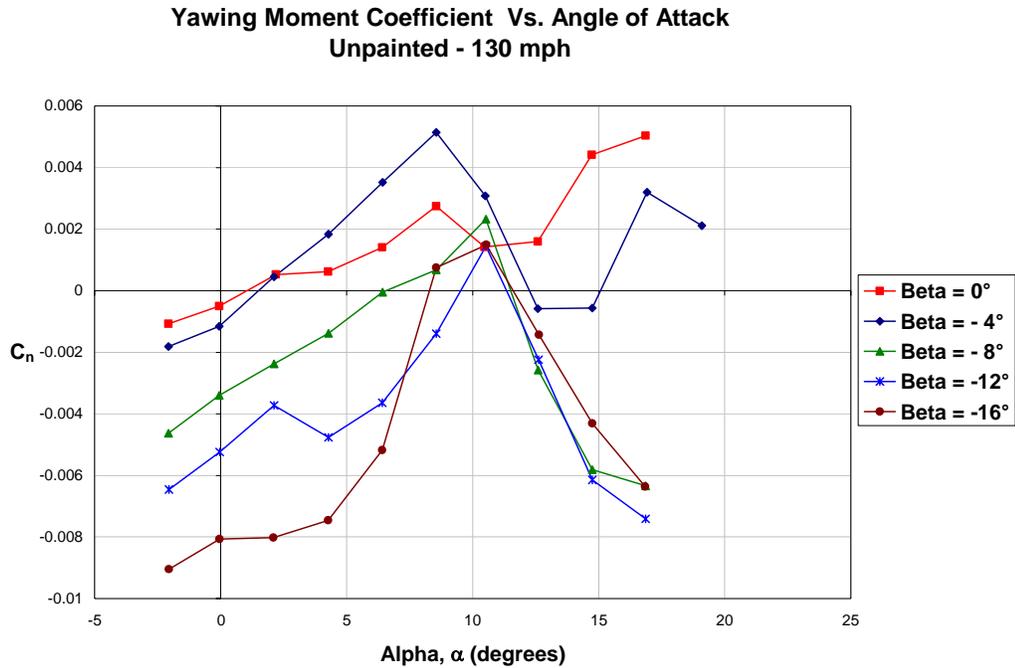
Figure 71: Unpainted model yawing moment comparison by beta angle at 130 mph.

The final graph of the beta run data is of the coefficient of lift versus angle of

attack data for the 130 mph test, plotted for varied beta. As in the above graph, Figure 72

below illustrates the effects of the unpainted model stall measured in the initial lift runs.

The lift curve slopes all line up with excellent agreement in for the angles of attack up to

9 degrees. At this point, it is apparent that the stall event occurs, quickly decreasing the

lift of the model, and then as before, the slope continues to increase with a slope similar

to that of the data before the abrupt stall. The data also clearly shows that the decrease in

lift at the stall event is much less for the β = -16° case than all other test cases. This

indicates that applying a yaw angle ($+\beta$) effectively counteracts the decrease in lift associated with the known stall event.

Lift Coefficient Vs. Angle of Attack
Unpainted - 130 mph
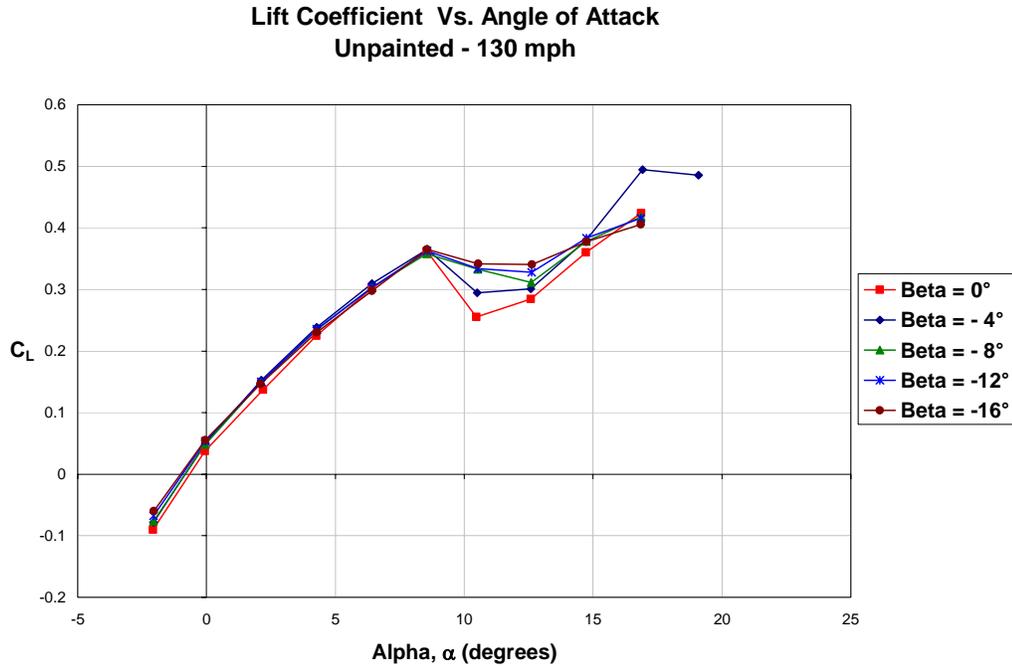
Figure 72: Unpainted model lift comparison by beta angle at 130 mph.

Section 3.1.2 – Painted Model

Lift and drag coefficient data for the one beta sweep performed with the painted strike tanker model is presented below in Figure 73. As expected, the lift values are consistently higher than the drag values, and symmetry exists across the beta range for both cases. Figure 74 presents the rolling and yawing moment coefficient data versus angle of attack. The data shows a steady slope for both parameters, indicating good stability across the beta range, with no abnormal increases or decreases in the data.

Lift & Drag Coefficients Vs. Yaw Angle
110 mph - AOA 8°
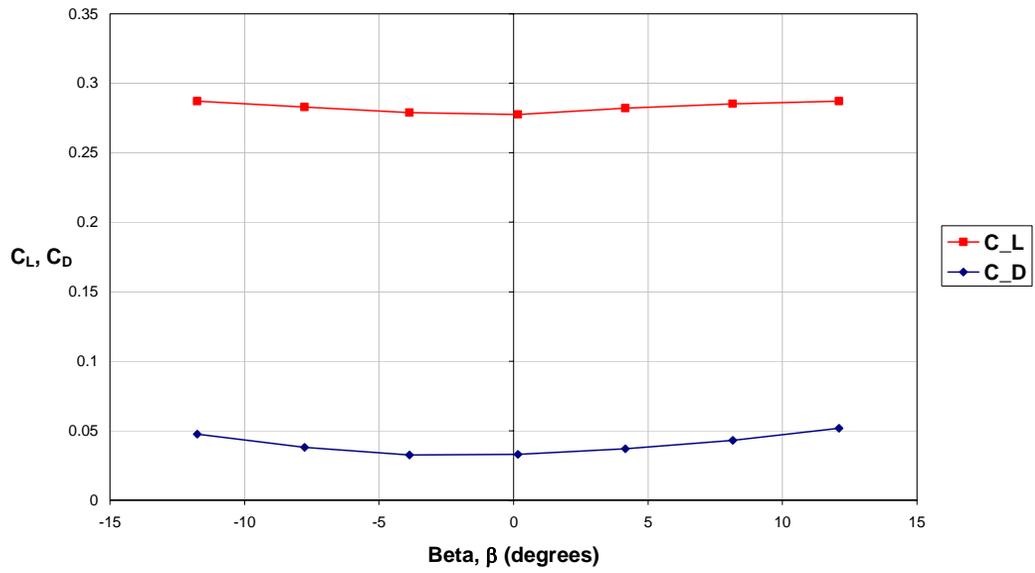
Figure 73: Painted model lift and drag coefficient versus beta at 110 mph.

Rolling & Yawing Moment Coefficients Vs. Yaw Angle
110 mph - AOA 8°
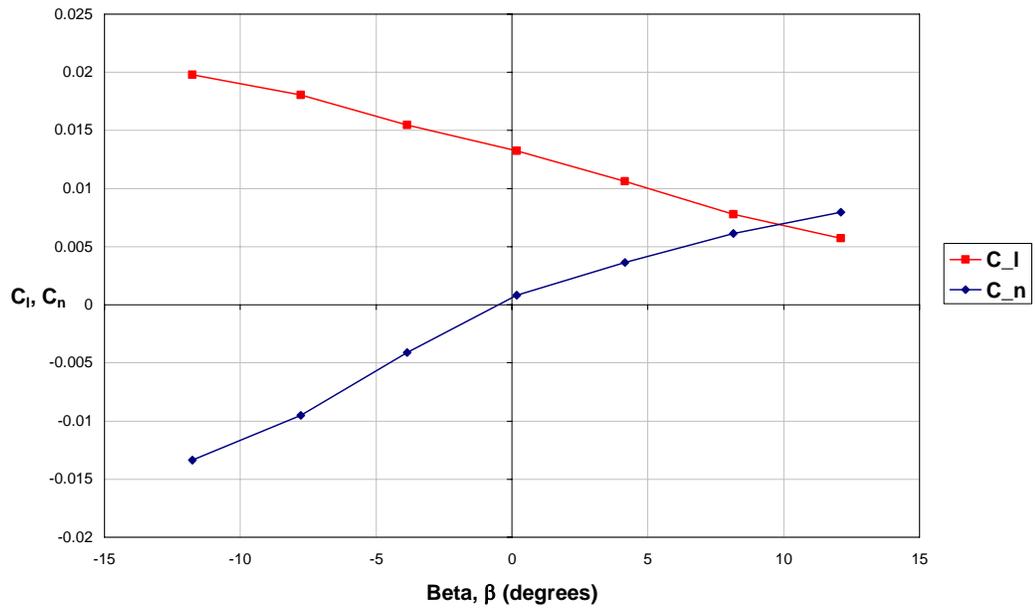
Figure 74: Painted model rolling and yawing moment versus beta at 110 mph.

Section 3.2 – Pressure Data

The following presentation of PSP data is shown in the form of a series of images for a beta sweep from -12 degrees to +12 degrees at an angle of attack of 8 degrees. Also accompanying the pressure distribution images are the pressure tap measurements and the associated corrections applied to the data images below. The methods used to process and filter the PSP data were identical to those used above; however, the figures exhibit streaks and discolorations caused by a combination of background and alignment issues.

Section 3.2.1 – Pressure Sensitive Paint Images
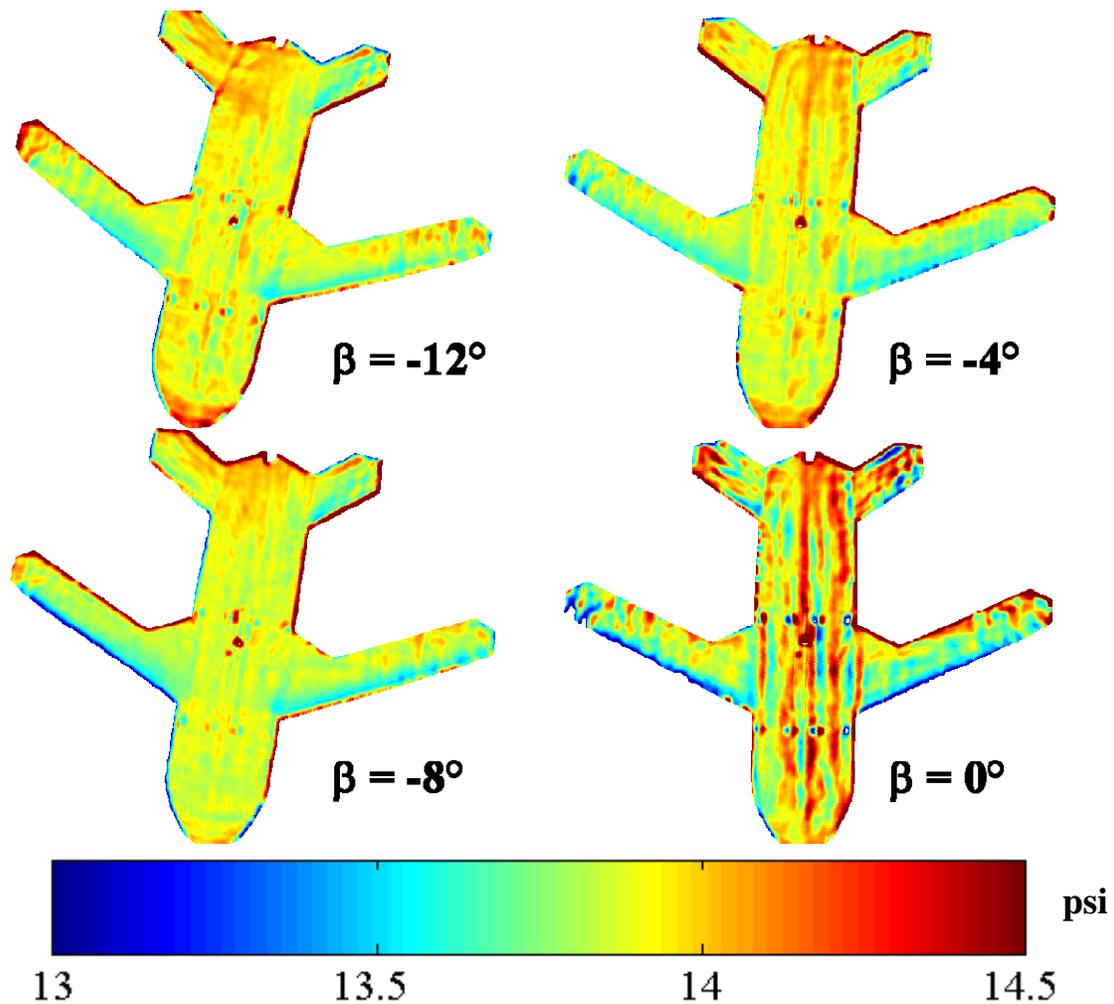
Figure 75: Full view PSP images for β = -12° to 0 ° at 110 mph.

A study of yaw variations for a single angle of attack was performed at $\alpha = 8°$, and β was varied from -12 to +12 degrees in 4 degree increments at 110 mph. The PSP images from -12 to 0 degrees are shown above in Figure 75 and Figure 76 below shows the images for the beta range of 0 to +12 degrees. The data shown was taken with the same setup as the full view PSP data, but after the wing view PSP data. This required the realignment of all of the lights and the camera and lens. This is one potential contributor to the fluctuations in image intensities, as well as alignment and background interference issues. However, further investigation is required to determine the exact cause for the streaky images. One result seen in this data is the differences in pressure distributions on the right and left wings of the $\beta = -12°$ case. It is likely that the pressure changes on the right wing are due to the effect of the nose of the model disrupting the oncoming flow before it reaches the wing.
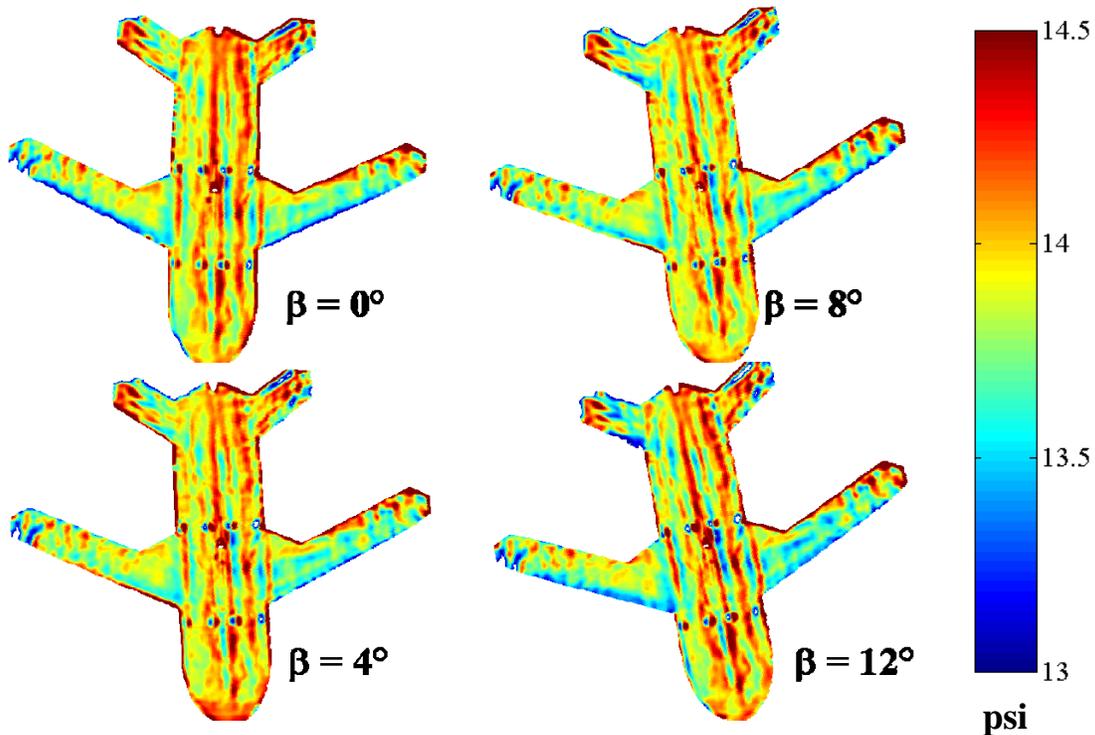
Figure 76: Full view PSP images for $\beta = 0°$ to $+12°$ at 110 mph.

Section 3.2.2 – Pressure Tap Data and Comparisons

The pressure tap system used in the study was again used to determine and apply the correction to the PSP images for the yaw data. As seen in Figure 77 below, the variation in the pressure tap readings was less than 0.05 psi as the yaw angle is varied. Nevertheless, a trend still exists as shown by the tap of a common side. The tap readings located on the right side of the model effectively increase as yaw angle decreases, and the tap readings from the left side effectively decrease over the same range.
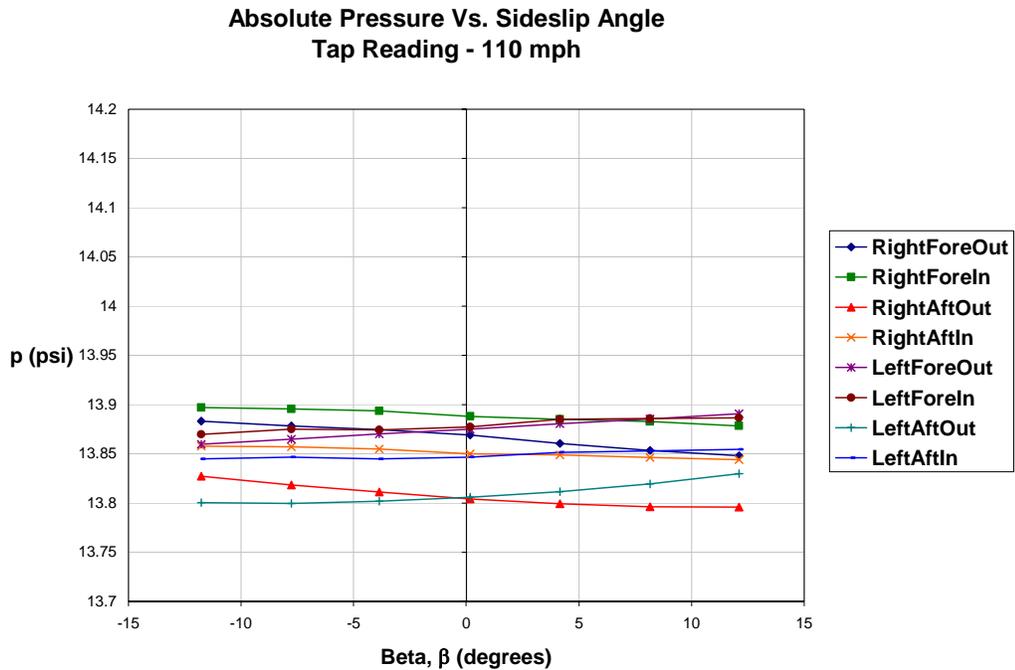
Figure 77: Tap pressure readings for beta sweep at 110 mph.

Due to the variation of the PSP image data as shown in Figure 78, the correction process was expanded to average the pressure reading difference between the tap and PSP data for the RightForeIn and LeftForeOut taps, and the LeftForeIn and LeftForeOut taps. The two shifts were averaged to produce the final shift shown in Figure 79 below.

100
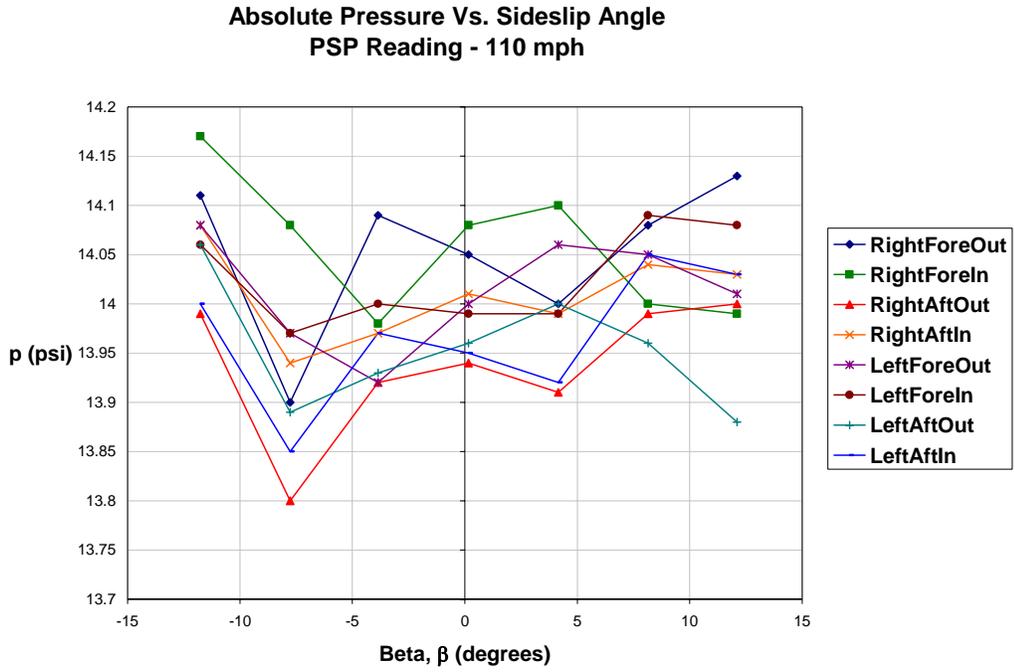
Figure 78: PSP pressure readings for beta sweep at 110 mph.
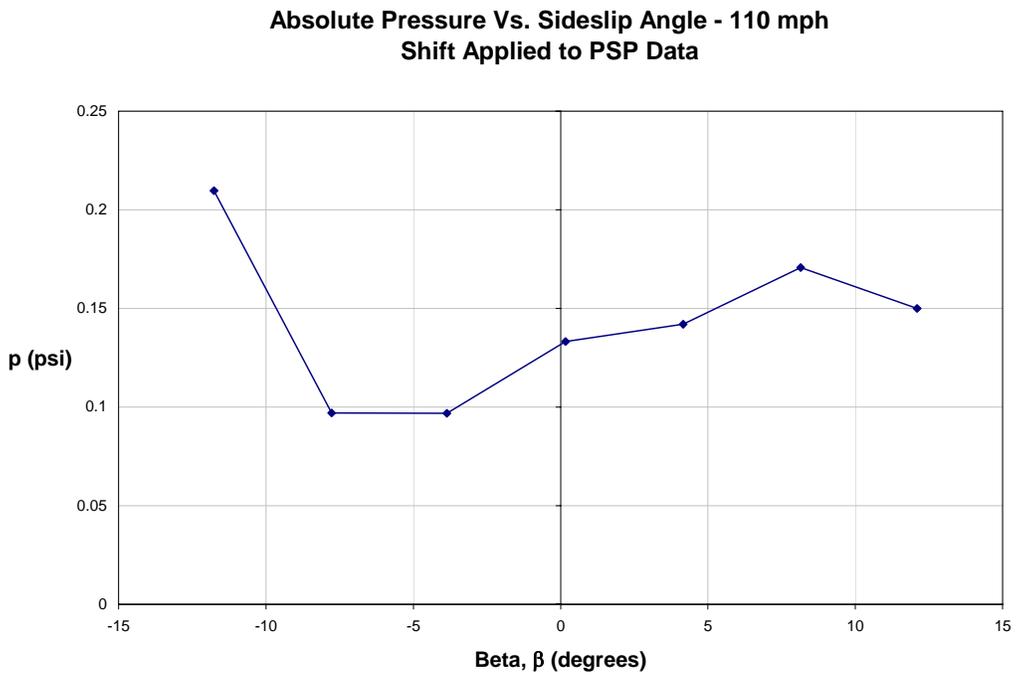
Figure 79: Pressure shift applied to correct PSP beta sweep images.

101

V. Conclusions

Section 1 - Summary

An experimental test program was undertaken as a part of a project focused on rapid design and assessment of aircraft. The plan for the tests performed on the 20:1 scaled down blended wing body, strike tanker model in the AFIT low-speed wind tunnel consisted of the following elements: acquire force and moment data using a six-component balance; compare the data to CFD simulations of the model under identical conditions; and use a global measurement technique (PSP) to discern reasons for any differences between the experiment and computation. The various rapid technologies included over the course of this study have proven to be valuable resources in terms of aircraft design evaluation. The comparisons of results between the balance measurements, CFD simulations, and PSP data imaging showed varying levels of correlation. These relationships provided insight into the best methods for data collection, and the most efficient ways to evaluate all of the data to determine the overall characteristics of the strike tanker design. The study also showed the feasibility of the rapid technology over a period of 18 months, and determined that the time needed to complete the process could be dramatically decreased. The limiting factor in this type of study in terms of data collection and comparison is the CFD analysis, due to the required setup times, in addition to the run time of precise simulations. The time constraints of this study were due to the limited availability of the equipment and facilities; however, an industrial air framer with all of the capabilities under one roof would be quite capable of completing the process in a short period of time.

The testing covered air speeds ranging from 60 mph to 145 mph as described in previous chapters with a focus on the 110 mph and 145 mph test speeds, which correspond to Mach numbers of 0.15 and 0.19, and Reynolds numbers of 1.35×10^5 and 1.79×10^5, respectively. The full experimental test matrix is shown as Table 5 in Appendix E: Experimental Test Matrix. The initial measurements conducted for the model prior to the application of PSP showed substantial differences between the balance measured and CFD computed lift slopes. Moreover, an unexpected stall event was measured, which curiously had a strong dependence on air speed, despite the limited range of Reynolds numbers in the test. It appeared as though the application of PSP would provide an excellent opportunity to learn more about the flow around the aircraft.

Subsequently, PSP was applied to the model to enable global pressure measurements. Force and moment data was taken along with the PSP, but – based on the literature – the effect of the paint was expected to be minimal. However, upon inspection of the results of this thesis study, *dramatic* differences were seen in the measured force and moment data before and after paint had been applied to the model. The evidence of the change in the flight characteristics is prominent in all of the lift and drag coefficient comparisons, as well as the pitching moment stability for both the 110 mph and 145 mph test cases. The test conditions between the unpainted and painted model test were constant with the exception of the application of the paint to the model. The repeatability of the experiments was affirmed two days separated by several months is shown and verified by the lift and drag data in Figure 32 and Figure 33 above for the 90 mph and 130 mph tests, respectively. At this point, a portion of this project was refocused on the reason why the paint would have such a profound effect. This led to the determination

that the variation seen between the data for the unpainted and painted model was likely an effect of the strike tanker model surface roughness. A profilometer was used to characterize the surface roughness of the model, and it was found that the Ra increased from 0.32μm to 0.66μm, effectively doubling.

The research of surface roughness changes and their effects on aerodynamic performance and associated data is quite extensive; however, there have been a limited number of studies that focus on the effects caused by PSP. A majority of studies have also been conducted for high Reynolds number applications of wings that fall under the flat plate simulation. In the case of this swept wing model tested at low Reynolds numbers on the order of 10^5, the general two dimensional boundary layer theories as defined in Ref. 24 do not apply directly without some modification due to the crossflow effects on boundary layer transition generally found in swept wing flows. As shown in

Table **3**, current studies performed in this very active research area have generally shown that boundary layer effects are seen for surface roughnesses that do not meet the admissible roughness criteria, which is based on a 2-D flat-plate analogy.

The conclusion that the measured micron-sized surface roughness increase as illustrated in Figure 63 through Figure 65 was the cause of the changes in the aerodynamic performance of the model is best supported by the experiments of Radeztsky et al., which determined that micron sized roughness effects in swept wing applications had an effect on boundary layer transition. Sustaining data is also shown in the study performed by Miklosovic et al. at the United States Naval Academy on the surface finish of a swept sailboat centerboard. Their results showed that aerodynamic performance decreased as the surface finish of the stabilizer was improved. The results

presented by these two studies reinforces that the effective doubling of the surface roughness from painting the model changed the aerodynamic characteristics.

Although the blended wing body configuration effects of the strike tanker model do not provide an additional explanation for the change in aircraft performance, their importance is seen in the unpainted model force and moment data. These configuration effects are also quite evident in the full view PSP images for both the 110 and 145 mph tests. An important aspect of a blended-wing body aircraft is the lifting ability of its fuselage. In the design process the body is designed based on the most efficient overall contribution to the aerodynamic lift characteristics in conjunction with those of the aircraft's wings. The data shown in all of the unpainted model lift plots indicate a region where an abrupt stall, which can be best described as the point at which wing lift decreases dramatically, occurs at a certain angle attack based on air speed. Although the wing stall is quite evident in the lift curves of the unpainted model shown in Figure 26, the graph also shows that in each case, the overall lift coefficient has a positive slope after the wing stall point.

However, in the painted model tests, the lift curve slope was shown to steadily increase through the entire angle of attack range, with a slight break in the slope seen only in the unpainted model stall region. This result is strongly supported by the study performed by Katz et al., which indicates that this continuation of a positive lift curve slope is due to the lift created by the fuselage of the blended-wing body strike tanker. In order to further examine the changes in the model that led to the above conclusions, the images produced from the PSP data were thoroughly examined.

Upon inspection of the full view PSP data, evidence of this lifting phenomenon was found at the angles of attack near the wing stall. In the 110 mph images as shown in Figure 50 and Figure 51, starting at 10 degrees, and continuing through 20 degrees, an area of low pressure forms and becomes more pronounced and defined in the area at the wing-body junction. This region of low pressure adjacent to the higher wing pressure indicates that the entire wing is not completely stalled and agrees with the continuing increase in lift coefficient seen in the painted model force data. This same effect is shown with more detail and intensity for the 145 mph case as shown in Figure 53 and Figure 54. The areas of low pressure seen in the PSP images account for the continuing lift exhibited by the force data and show that the lift mechanism the model relies on has drifted away from that of a typical wing and towards one typically found on delta wings. In addition, the previous conclusions show that this lift mechanism is strongly affected by surface finish.

The final piece of information gained from this experimental study is the aerodynamic stability of the strike tanker model. This information is best described using the graphs of the pitching moment and yawing moment coefficients. These figures showed that for the unpainted model pitching moment instability issues exist in the angle of attack region of the abrupt stall. As shown in Figure 31 the angle of attack increases the pitching moment is held at a constant rate until this stall event, at which point the pitching moment increases drastically, which would cause the aircraft to pitch up without notice and be difficult to control. The instabilities of the yawing moment in the stall region are evident in Figure 68 and Figure 71 for the unpainted model 90 mph and 130 mph tests, respectively. In each figure the stall region is accompanied by large

discrepancies in the slope of the yawing moment versus beta curves. The indicated problems do not follow any particular pattern, and drastically deviate from the low angle of attack trends for each different air speed. This fluctuation in would typically cause instability in the directional heading of the aircraft when the stall angle of attack is reached, therefore causing a control difficulty similar to that seen with the pitching moment. The improvement trends of the pitching moment stability between the unpainted and painted models are likely to continue for the yawing moment; however, to date, no data is available to support this assumption.

Finally, upon evaluation of all of the experimental data taken throughout this research, a number of potential error sources were uncovered. As shown in Figure 30, the error in the balance measurements was larger at low angles of attack. However, the error in the balance measurements was not of great concern due to the repeatability shown between the various tests performed before and after painting with the model removed and re-installed in the process. Another main source of error is that of the PSP data images. The primary causes of error in this data are due to image alignment, background image noise, and the reflected light into the camera from the test section's plexiglass top. The alignment issues are seen in the beta sweep images and the image noise is seen in terms of the circular discolored region in the 110 mph wing data in Figure 52 and the discolored lines in the 110 mph beta sweep data in Figure 76. A potential error in the PSP data is the reflection of the light off the model surface through the paint, due to the fact that a base coat was not applied prior to the PSP. Sedimentation and photo-degradation are also known PSP errors; however, the testing time was determined to be short enough that these effects were negligible.

Section 2 - Future Considerations

There is a large amount of experimental potential at the AFIT low-speed wind tunnel for future PSP testing. The wind tunnel system and its setup allow for numerous configurations of lights and cameras for acquiring the PSP images. In this sense the idea of acquiring PSP data from both the top and bottom of an aerodynamic vehicle or wing using a plexiglass sting platform becomes a viable option for testing. This method would then allow the calculation of lift data from the PSP images for comparison with the balance measured values.

The use of the rapid prototyping process could potentially expand studies of different model configurations. For instance, the strike tanker had removable wings, and another completely different wing design could be tested and compared for aerodynamic characteristics such as lift and drag, and any determined stall occurrences.

CFD is another powerful tool used in the process of aircraft and automobile design characterization. Joint studies involving the combination of CFD simulations and experimental verification using the PSP system will further broaden the capabilities of the AFIT facilities, as well as offer additional methods for verifying and determining errors in the results of the PSP measurements

Figure 80: CFD/PSP Comparison - NOTE: Different test conditions and scales.

Appendix B: Additional CFD Solutions for Rapid Prototyping
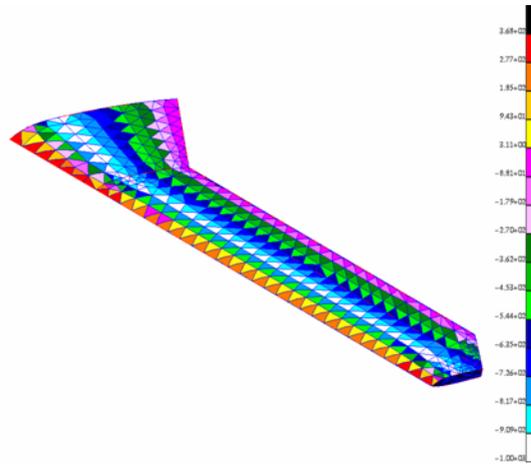
Figure 81: Finite element pressure distribution (28).
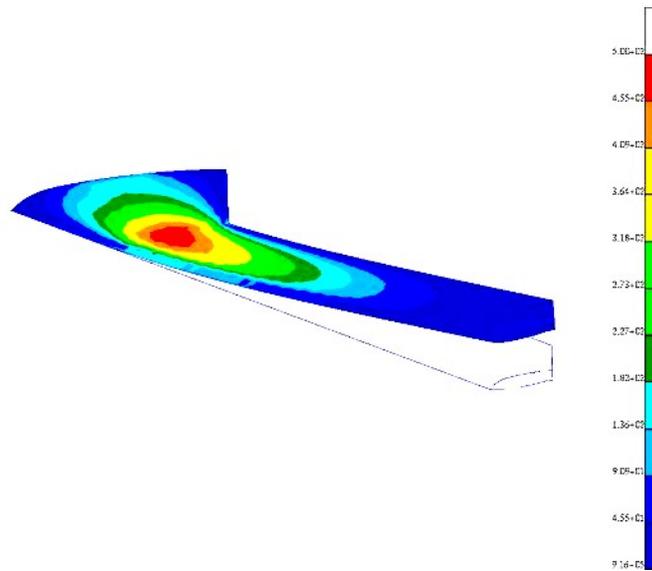
Figure 82: Finite element stress analysis (28).

Appendix C: Roughness Applications (Schlichting)
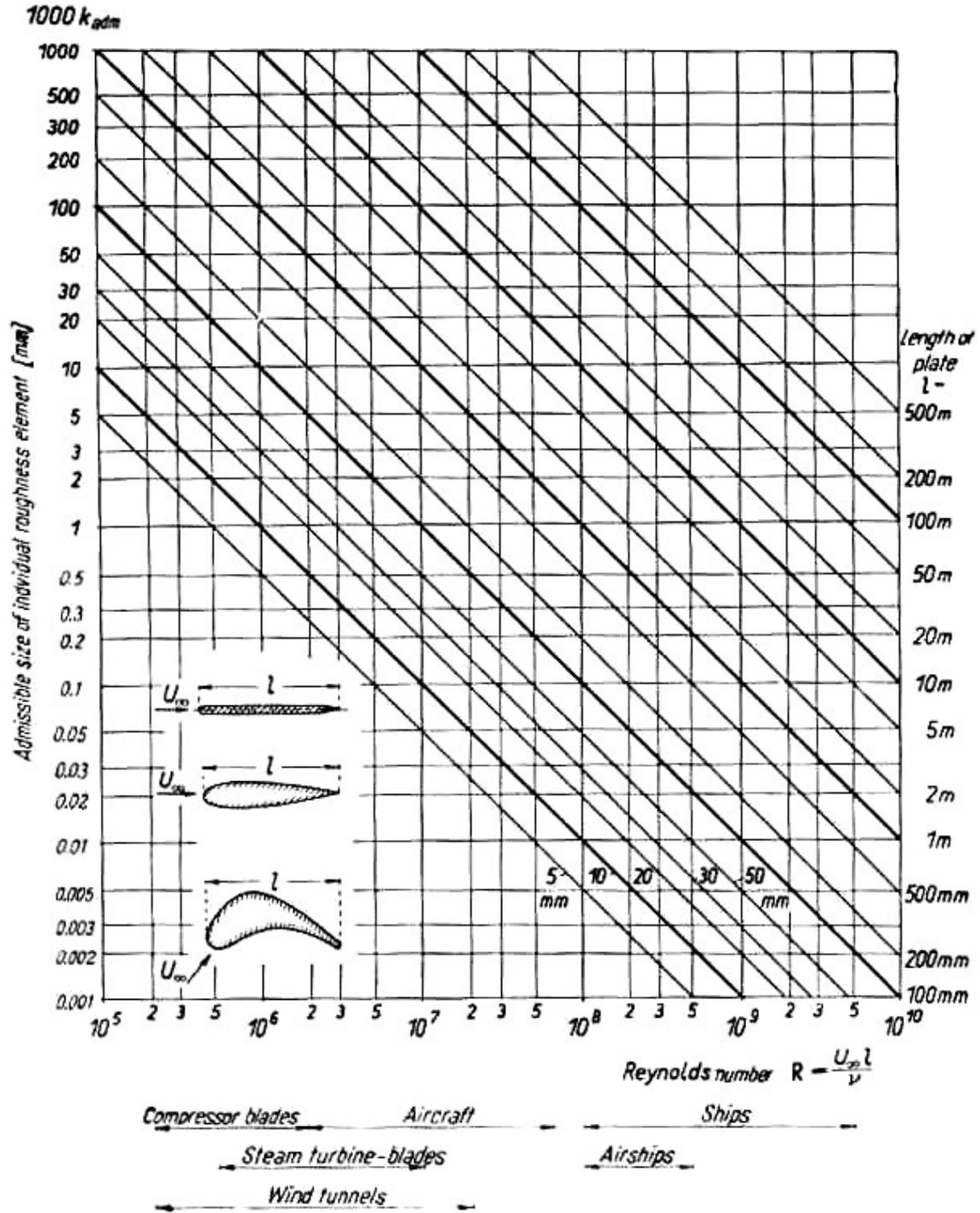
Figure 83: Admissible roughness k_{adm} for rough plates at zero incidence (24).

111

Table 4: Admissible roughness calculations for various applications (24).

Table 21.3. Examples on the calculation of admissible roughness from Fig. 21.16

Item	Description	Length l m (ft)	Velocity w km/h	m/sec	ft/sec	Kinematic viscosity $10^6 \times \nu$ m²/sec	ft²/sec	$R = \dfrac{w\,l}{\nu}$	Admissible roughness k_{adm} mm	in
Ship's hull	large fast	250 (820)	56 30 knots	15	49	1·0	10	4×10^9	0·007	0·00028
	small slow	50 (165)	18 10 knots	5	165	1·0	10	3×10^8	0·02	0·0008
Airship	—	250 (820)	120	33	1100	15	150	5×10^8	0·05	0·002
Aeroplane (wing)	large fast	4† (13)	600	166	545	15	150	5×10^7	0·01	0·0004
	small slow	2 (6·5)	200	55	180	15	150	8×10^6	0·025	0·001
Compressor blades	slow	0·1 (0·33)	—	150	490	15	150	1×10^6	0·01	0·0004
Model wings	small	0·2 (0·65)	144	40	130	15	150	5×10^5	0·05	0·002
Steam turbine blades	high pressure $t = 300\,C\,(\sim 550\,F)$	10 mm (0·4 in)	—	200	650	0·4	4	5×10^6	0·0002	0·000008
	high pressure $t = 500\,C\,(\sim 950\,F)$	10 mm (0·4 in)	—	200	650	0·8	8	$2·5 \times 10^6$	0·0005	0·00002
	low pressure	100 mm	—	400	1300	8	80	5×10^6	0·002	0·00008

† Chord.

112

Appendix D: MATLAB Code for Balance Data Reduction

```
%*********************************************************************
%*********************************************************************
%**********    Lt. Dave Gebbie & Capt Anthony DeLuca    ******************
%**********                                             ******************
%**********     Calculation of Lift, Drag, Moments      ******************
%**********  AFRL Project: Strike Tanker, 11 May 2004   ******************
%*********************************************************************
%*********************************************************************


%This Code will transfer measured Forces and Moments on the balance to Wind
%(earth) centered frame of reference by correctiing for tare effects, balance
%interactions, and wind tunnel irregularities, then plot lift and drag
%coefficients in as functions of AoA, beta, Prop speed, and elevon
%deflection angle.

clear; clc; format short g;


%*************************************************************************************

%**********************Room Conditions and Model Specifics : *********************
%********************* UNITS are in Ft, Sec, lbm, Psf, Rankine, fps *****************


Mass = 15.36;                                    %lbm (Strike Tanker)
Gas_Const = 1716;                                %ft-lbf/Slug-R
T_room = mean([71,85]) + 459.67;                 %deg R  ****Changed for each day of testing****
P_barro = mean([28.7825,28.7621,28.7765]) * 0.4911541:   %Psi  ****Changed for each day of testing****
Density = (P_barro * 144)/(1716 * T_room);       %lbm/ft^3 or lbf-s^2/ft^4
Wing_Area = 147.34 / 144;                        %ft^2  for CFD comparison (Tyler, 5-11-04)
Root_Chord = 1.6875 * (1/12);                    %ft (S.T.)
Span = 20.125 / 12;                              %ft
Aspect_Ratio = Span^2 / Wing_Area;
Kinematic_Viscosity = .372e-6;                   %slug/ft-s
Speed_of_Sound = sqrt(1.4 * T_room * Gas_Const); %fps

%Distances between sensors (inches) to calculate moments

D1 = (2.10 / 2); D2 = D1; D3 = (1.7 / 2); D4 = D3;           %inches

%Offset distances from the Mounting Block to the Model C.G. (inches)

Y_cg = 0.0;                              %changed May 11 2004 >> Strike Tanker
X_cg = 4.4475;                           %inches (from origin @ balance center w/ + right)
Z_cg = 0.0;                              %inches (from origin @ balance center w/ + down)


%*********************************************************************
%************************ Tunnel Correction Data  *********************
%*********************************************************************
K_1 = 0.97;                              % 0.97 13 Sept 04 - May 11, 2004 (Strike Tanker)
K_3 = 0.92;                              % "
delta = 0.125;
Tau_1 = 0.85;
X_Section = (32/12)*(41/12)  ;           %ft^2
Wing_Volume = Wing_Area * (.15/12)  ;                %ft^3
```

```matlab
Body_Volume = (79.6-Wing_Volume*12^3) / 12^3 ;          %ft^3

    %****  Solid body blockage corrections due to wing and fuselage ***

Epsilon_sb_w = (K_1*Tau_1*Wing_Volume) / X_Section^(3/2);
Epsilon_sb_b = (K_3*Tau_1*Body_Volume) / X_Section^(3/2);
Epsilon_tot = Epsilon_sb_w + Epsilon_sb_b;

%*************************************************************************
%************************** Tunnel Correction Data  **********************
%*************************************************************************

%Balance Interactions with off axis elements for the 8 lb balance
%Using average of the 8 lb calibration runs for N1 & N2 and the
%6 lb calibration for S1, S2 & A then normalizing by the actual
%sensor (N1, N2,...) in question.  The sensor sequence in each row vector is:
%[N1 N2 S1 S2 A L]

N1_I = ([7.806 -.701 .447 .060 -.142 .043] + [7.803 -.702 .442 .057 -.140 .041])/2;
    N11 = N1_I(1,1)/100;

N2_I = ([.183 -7.486 -.05 -.052 .047 0] + [.182 -7.485 -.053 -.056 .044 0])/2;
    N22 = N2_I(1,2)/-100;

S1_I = ([.039 0 7.917 -.408 -.024 -.025] + [.036 0 7.915 -.410 -.026 -.022])/2;
    S11 = S1_I(1,3)/50;

S2_I = ([0 .013 -.124 8.16 -.067 -.017] + [0 .012 -.122 8.158 -.065 -.015])/2;
    S22 = S2_I(1,4)/50;

A_I = ([.012 .008 -.025 .041 6.981 0.09] + [.012 .007 -.025 .033 7.003 .081])/2;
    A11 = A_I(1,5)/50;

L_I = ([-.082 -.061 -.023 .096 .262 8.607] + [-.09 -.072 -.009 .104 .276 8.604])/2;
    L11 = L_I(1,6)/40;

N1_normalized = (N1_I/100)  .* [N11 N22 S11 S22 A11 L11].^(-1);
N2_normalized = (N2_I/-100) .* [N11 N22 S11 S22 A11 L11].^(-1);
S1_normalized = (S1_I/50)  .* [N11 N22 S11 S22 A11 L11].^(-1);
S2_normalized = (S2_I/50)  .* [N11 N22 S11 S22 A11 L11].^(-1);
A_normalized = (A_I/50)    .* [N11 N22 S11 S22 A11 L11].^(-1);
L_normalized = (L_I/40)    .* [N11 N22 S11 S22 A11 L11].^(-1);

Interactions_Kij = [N1_normalized' N2_normalized' S1_normalized' S2_normalized' A_normalized' L_normalized'];

%Load the static tare data for the alpha sweep w/o the wind , separate each
%force from the file, and fit a 4th order poly as an x-y plot (AoA vs.
%Force) for each of the 6 force sensors.

%***********************Code inserted May 11, 2004**************************

load M0A5to9Y035Lights          % Raw data file to be read in.
FILE=M0A5to9Y035Lights(:,:);

j=1;
```

```matlab
k=1;
L=length(FILE);

for i=1:L                               %Run for all data points # of rows
    if i~=L                             %if current row is not last row, go to next
        NEXT=i+1;                       %set next equal to the value of the next row
        VALUE2=FILE(NEXT,1);            %set value2 as next row column 1
    else if i==L                        %unless the it is the last value
        VALUE2=50;                      %value2 set to 50 to end the sequence
    end
    end
    A(j,:)=FILE(i,:);                    %set row j of A equal to row i of FILE
    VALUE1=FILE(i,1);                    %set value1 equal to row i column 1 of FILE
    if VALUE1==VALUE2                    %if value1 equals value2, go to next row
        j=j+1;
    else if VALUE1~=VALUE2              %if value1 and value2 are different check
        if length(A(:,1))<20           %if less than 20 values, ignored due to angle change
            j=1;
            clear A;
        else if length(A(:,1))>20       %if more than 20 values
            C=length(A(:,1));           %find length of A
            for m=1:19                  %Average all rows of the like values in A
                B(k,m)=mean(A(11:C,m)); %disregarding first 10 for vibrations
            end
            j=1;
            k=k+1;
            clear A
        end
        end

    end
    end
end

if B(k-1,1)<B((k-2),1)
    B=B(1:(k-2),:)
end

tare=[B]

%*****************************End of Inserted Code***************************

[row,col] = size(tare);

for k = 1:row

theta_tare(k,:,:)  = tare(k,1).* (pi/180);
N1_tare(k,:,:)     = tare(k,4);
N2_tare(k,:,:)     = tare(k,5);
S1_tare(k,:,:)     = tare(k,7);
S2_tare(k,:,:)     = tare(k,8);
A_tare(k,:,:)      = tare(k,6);         %changed 13Jan05 misnamed column
L_tare(k,:,:)      = tare(k,9);

end
```

```matlab
N1_poly = polyfit(theta_tare,N1_tare,4);
N2_poly = polyfit(theta_tare,N2_tare,4);
S1_poly = polyfit(theta_tare,S1_tare,4);
S2_poly = polyfit(theta_tare,S2_tare,4);
A_poly  = polyfit(theta_tare,A_tare,4) ;
L_poly  = polyfit(theta_tare,L_tare,4) ;

clear ('B','C','D','L')

%Load the specific test run files, subtract the effect of the static
%weight with the tare polynominals above, and correct for cross diagonal
%sensor interactions.

%*************************Code inserted May 11, 2004**************************
                                              %modified January 11, 2005
load M145A5to9Y035                            % Raw data file to be read in.
FILE=M145A5to9Y035(:,:);

j=1;
k=1;
L=length(FILE);

for i=1:L                                  %Run for all data points # of rows
  if i~=L                                  %if current row is not last row, go to next
    NEXT=i+1;                              %set next equal to the value of the next row
    VALUE2=FILE(NEXT,1);                   %set value2 as next row column 1
  else if i==L                            %unless the it is the last value
    VALUE2=50;                            %value2 set to 50 to end the sequence
  end
  end
  A(j,:)=FILE(i,:);                        %set row j of A equal to row i of FILE
  VALUE1=FILE(i,1);                        %set value1 equal to row i column 1 of FILE
  if VALUE1==VALUE2                        %if value1 equals value2, go to next row
    j=j+1;
  else if VALUE1~=VALUE2                   %if value1 and value2 are different check
    if length(A(:,1))<20                   %if less than 20 values, ignored due to angle change
      j=1;
      clear A;
    else if length(A(:,1))>20              %if more than 20 values
      C=length(A(:,1));                    %find length of A
      for m=1:19                           %Average all rows of the like values in A
        B(k,m)=mean(A(11:C,m));            %disregarding first 10 for vibrations
      end
      j=1;
      k=k+1;
      clear A
    end
    end
  end
  end
end

if B(k-1,1)<B((k-2),1)
  B=B(1:(k-2),:)
```

116

```matlab
end

sample_data=[B]

%****************************End of Inserted Code****************************

[row2,col2] = size(sample_data);

for i = 1:row2

%Angles of the model during test runs (Roll, Pitch {AoA}, Yaw {Beta}):

phi            = 0;
theta(i,:)     = sample_data(i,1) .* (pi/180);                    %radians
si(i,:)        = sample_data(i,2) .* (pi/180);                    %radians
Wind_Speed(i,:)  = sample_data(i,3) .* (5280/3600);              %fps
pressure(i,:)   = sample_data(i,(12:19)) - tare(i,12:19);

%Flight Parameters (Re#, Ma#, Dynamic Pressure):

q = (.5 * Density) .* Wind_Speed.^2;                             %lbf/ft^2
q_Corrected = q .* (1 + Epsilon_tot)^2;                         %lbf/ft^2
Wind_Speed_Corrected = Wind_Speed .* (1 + Epsilon_tot);        %fps
Mach_Number = Wind_Speed_Corrected ./ Speed_of_Sound;
Reynolds_Number = ((Density * Root_Chord) .* Wind_Speed_Corrected) ./ Kinematic_Viscosity;
Flight_Parameters = [Mach_Number Reynolds_Number q_Corrected];

%individual forces for each sensor:

N1_test(i,:,:)     = sample_data(i,4);
N2_test(i,:,:)     = sample_data(i,5);
S1_test(i,:,:)     = sample_data(i,7);
S2_test(i,:,:)     = sample_data(i,8);
A_test(i,:,:)      = sample_data(i,6);      %changed 13Jan05 misnamed column
L_test(i,:,:)      = sample_data(i,9);

%Evaluating the actual test theta angle (AoA) in the tare polynominal to
%determine the tare values for the angles tested in each run.

N1_eval = polyval(N1_poly,theta);
N2_eval = polyval(N2_poly,theta);
S1_eval = polyval(S1_poly,theta);
S2_eval = polyval(S2_poly,theta);
A_eval  = polyval(A_poly,theta);
L_eval  = polyval(L_poly,theta);

%The Time-Averaged (raw) forces N1, N2, S1, S2, A, L measurd in the wind
%tunnel (body axis) with the tare effect of the weight subtracted off.

N1_resolved = N1_test - (N1_eval);
N2_resolved = N2_test - (N2_eval);
S1_resolved = S1_test - (S1_eval);
S2_resolved = S2_test - (S2_eval);
A_resolved  = A_test -  (A_eval);
L_resolved  = L_test -  (L_eval);
```

117

```matlab
Forces_minus_tare = [N1_resolved N2_resolved S1_resolved S2_resolved A_resolved L_resolved]';

%Forces N1, N2, S1, S2, A, & L corrected for the balance interactions (body axis)

Corrected_Data = (inv(Interactions_Kij) * Forces_minus_tare);

%Calculation of the Axial, Side, & Normal Forces from the corrected balance
%forces in the Body Axis reference frame

Forces_b(:,i) = [Corrected_Data(5,i); Corrected_Data(3,i) + Corrected_Data(4,i); Corrected_Data(1,i) +
Corrected_Data(2,i)];

%Calculation of the Drag, Side, & Lift Forces in the Wind Axis reference
%frame

Forces_w = [Forces_b(1,:).*cos(theta').*cos(si')+Forces_b(2,:).*sin(si')+Forces_b(3,:).*sin(theta').*cos(si');
        -Forces_b(1,:).*sin(si').*cos(theta')+Forces_b(2,:).*cos(si')-Forces_b(3,:).*sin(theta').*sin(si');
        -Forces_b(1,:).*sin(theta')+Forces_b(3,:).*cos(theta')];

%First entry is the moments calculated by the balance or direct calculation
%in the Body Reference Frame.  Balance measures Roll (l), Yaw is about the
%z-axis (n), and Pitch is about the y-axis (m).  Distances from strain
%gages to C.G. are in INCHES.  Moments are in-lbf

m = Corrected_Data(1,i) * D1 - Corrected_Data(2,i) * D2;
n = Corrected_Data(3,i) * D3 - Corrected_Data(4,i) * D4;
Moments_b(:,i) = [Corrected_Data(6,i); m; n];

%Second entry is the conversion from the "Balance Centeric" moments to the
%Wind Reference monments with respect to the Balance Center (bc)

Moments_w_bc = [Moments_b(1,:).*cos(theta').*cos(si')-
Moments_b(2,:).*sin(si')+Moments_b(3,:).*sin(theta').*cos(si');
        Moments_b(1,:).*sin(si').*cos(theta')+Moments_b(2,:).*cos(si')+Moments_b(3,:).*sin(theta').*sin(si');
        -Moments_b(1,:).*sin(theta')+Moments_b(3,:).*cos(theta')];

%Finally, the balance centered moments are converted to moments about the
%Model's Center of Mass (cm) or Center of Gravity (CG)

cgdist=sqrt((X_cg)^2+(Z_cg)^2); %Obtaining the direct distance between the
                    %center of the balance and the center of mass
w=atan(-Z_cg/X_cg);  %Obtaining the angle between cgdist and the x axes at zero angle of attack

X_cm(i,:)= cos(theta(i,:)+w)*cos(si(i,:))*(cgdist);
Y_cm(i,:) = Y_cg + X_cm(i,:)*tan(si(i,:));         % appropriate for very small y_cmb and reasonable si
Z_cm(i,:)= -sin(theta(i,:)+w)*(cgdist);

Moments_w_cg_u = [Moments_w_bc(1,:) + Z_cm(i,:)*Forces_w(2,:) + Forces_w(3,:)* Y_cm(i,:);
        Moments_w_bc(2,:) - X_cm(i,:)*Forces_w(3,:) + Forces_w(1,:)* Z_cm(i,:);
        Moments_w_bc(3,:) - Y_cm(i,:)*Forces_w(1,:) - Forces_w(2,:)* X_cm(i,:)];

%Calculation of the actual Lift and Drage nondimensional Coefficients, uncorrected for tunnel effects, (Cl
%and Cd)
```

```matlab
C_L_u = Forces_w(3,:) ./ (q_Corrected' .* Wing_Area);          %Keuthe & Chow pg 178
C_D_u = Forces_w(1,:) ./ (q_Corrected' .* Wing_Area);
Coefficients = [C_L_u; C_D_u]';
% Ave_Cl = mean(Coefficients(:,1));
% Ave_Cd = mean(Coefficients(:,2));

end

%*****************************************************************************
%************************** Tunnel Correction Data  **************************
%*****************************************************************************

        %***************** Drag Coefficient Correction **************
C_D_o = min(Coefficients(:,2));
C_L_u_sqrd = Coefficients(:,1).^2;
Delta_C_D_w = ((delta * Wing_Area) / X_Section) .* C_L_u_sqrd;
C_D_Corrected = C_D_u' + Delta_C_D_w;

        %************* Angle of Attack due to upwash Correction *********

alpha = sample_data(:,1);
Delta_alpha_w = ((delta * Wing_Area) / X_Section) .* (57.3 * C_L_u);
alpha_Corrected = alpha + Delta_alpha_w';

        %************* Pitching Moment Correction *******************

tau2 = 0.3;
l_t = 5.16/12;                              % ft = length from tail MAC to aircraft CG
Span_t = 9 / 12 ;                           % ft = Projected horizontal span of V-tail
Tail_Area = ((2.15*3.5*cos(.7))*2) / 144;   % ft^2 = Projected horizontal tail area
c_bar = 1.6875 / 12;                         % 1.6875 13 Sept 04 Changed ft = Mean Chord of wing
V_bar = (Tail_Area * l_t) / (Wing_Area * c_bar);   %  Horizontal tail volume ratio
eta_t = 1.0;
epsilon_o = 0;
i_t = .7;                                   % radians
i_w = 0;
Aspect_Ratio_t = Span_t^2 / Tail_Area;

D_epslion_D_alpha = ((2 .* C_L_u) ./ (pi* Aspect_Ratio))';
epsilon = epsilon_o + (D_epslion_D_alpha .* alpha_Corrected );
alpha_t = alpha_Corrected - i_w - epsilon + i_t;
C_L_alpha_t = ((0.1* Aspect_Ratio) / (Aspect_Ratio_t +2)) * 0.8;
D_Cm_cg_t_D_alpha_t = -C_L_alpha_t* V_bar * eta_t;
Delta_C_m_cg_t = ((D_Cm_cg_t_D_alpha_t) * (delta*tau2) * (Wing_Area / X_Section) .* (C_L_u * 57.3))';
Cl_w_cg =   Moments_w_cg_u(1,:) ./ (q_Corrected' .* (Wing_Area * c_bar*12));
Cm_w_cg_u = Moments_w_cg_u(2,:) ./ (q_Corrected' .* (Wing_Area * c_bar*12));
Cn_w_cg =   Moments_w_cg_u(3,:) ./ (q_Corrected' .* (Wing_Area * c_bar*12));
Cm_w_cg_corrected = Cm_w_cg_u - Delta_C_m_cg_t';
Corrected_Moment_Coefficients = [Cl_w_cg' Cm_w_cg_corrected' Cn_w_cg'];




%*****************************************************************************
```

119

```matlab
%************************* Tunnel Correction Data  *************************
%*************************************************************************

alpha = sample_data(:,1);

fprintf('   Mach Number Reynolds Number Dynamic Pressure(Psf)\r')
Flight_Parameters
fprintf(' \r');
fprintf(' Loads are in lbf and arranged [D S L] across the top and increments of alpha down the side \r')
Forces_w'
fprintf(' \r')
fprintf(' Moments are in in-lbf and arranged [L M N] down the side and increments of alpha along the top \r')
Moments_w_cg_u
fprintf(' \r')
fprintf('      Cl_u        Cd_u \r');
Coefficients
fprintf(' \r')
fprintf('   Del_CD_w      CD_u     CD_Corrected \r');
Compare_CD = [Delta_C_D_w C_D_u' C_D_Corrected]
fprintf(' \r')
fprintf('   Del_alpha_w    alpha_g    alpha_Corrected \r');
Compare_alpha = [Delta_alpha_w' alpha alpha_Corrected ]
fprintf(' \r')
fprintf('   Cl_cg_wind    Cm_cg_corrected_w    Cn_cg_wind \r');
Corrected_Moment_Coefficients
fprintf(' \r')
fprintf('      M#        Re#        q_c       Uoo      alpha_c     C_L     C_D_c     Cl_cg_w      Cm_cg_c_w
Cn_cg_w \r');
YY=[Flight_Parameters (Wind_Speed_Corrected .* (3600/5280)) alpha_Corrected C_L_u' C_D_Corrected
Corrected_Moment_Coefficients pressure]
%XX=['M#' 'Re#' 'q_c'  'Uoo' 'alpha_c' 'C_L' 'C_D_c' 'Cl_cg_w' 'Cm_cg_c_w' 'Cn_cg_w \r'];

%ZZ=[XX; YY];
wk1write('output.xls',YY,2,1)
```

Appendix E: Experimental Test Matrix

Date	Test speed (mph)	Type	Range (deg)	Increment	Reason
2/28/2004	60,90,110,130,145	alpha sweep	- 10 to +25	1	Initial test for functionality and abnormalities
2/28/2004	110	alpha sweep @beta = -10 deg	- 10 to +25	1	Initial test for yaw functionality
2/28/2004	110	alpha sweep @beta = -20 deg	- 10 to +25	1	Initial test for yaw functionality
5/29/2004	90	alpha sweep w/ varying beta	alpha:-2 to +16; beta: 0 to -16	2	Addition of pressure taps, further stability insight
6/3/2004	130	alpha sweep w/ varying beta	alpha:-2 to +16; beta: 0 to -16	2	Addition of pressure taps, further stability insight
12/9/2004	110,145	alpha sweep w/PSP - full view	0 to 20	2	PSP characterization, investigation of stall event
12/9/2004	110,145	alpha sweep w/PSP - half view	0 to 20	2	PSP characterization, investigation of stall event
12/13/2004	110,145	alpha sweepw/PSP - wing view	110: 14 to 18; 145: 5 to 9	1	Focused stall event examination
12/13/2004	110	beta sweep @ AOA 8 deg	12 to -12	4	Stability w/PSP and symmetrical analysis

Appendix F: Wind Tunnel Balance Raw Data

Table 6: Unpainted model - 60 mph alpha sweep, beta = 0°.

Mach #	Reynolds #	q_c	Uinf	Alpha_c	C_L	C_D_c	L/D	Cl_cg_w	Cm_cg_c_w	Cn_cg_w/r
0.07814999	74057.9992	8.700252843	60.55891267	-10.6606639	-0.38871053	0.075150026	-5.17246033	-0.0095484	0.68030477	-0.01837988
0.07813153	74040.50585	8.69614313	60.54460797	-9.85617307	-0.36199263	0.06324956	-5.72324348	-0.01235951	0.634100855	-0.02030309
0.078116145	74025.92582	8.692718584	60.53268554	-8.79052959	-0.33384178	0.05104558	-6.54007223	-0.01062984	0.591718914	-0.01944985
0.078127561	74036.74478	8.695259668	60.54153245	-7.72861532	-0.31157037	0.042372118	-7.35319327	-0.00917389	0.557946904	-0.01874129
0.078106529	74016.81403	8.690578756	60.52523462	-6.6652754	-0.28628334	0.032302819	-8.86248794	-0.00944464	0.520364726	-0.01747336
0.078089386	74000.56854	8.686764293	60.51195032	-5.58617151	-0.24264143	0.022734956	-10.6726148	-0.00715172	0.449915407	-0.01217436
0.078083627	73995.11062	8.685482953	60.50748725	-4.50904814	-0.20021853	0.01757402	-11.3928703	-0.00674573	0.371751734	-0.01150556
0.078056214	73969.13299	8.679385561	60.48624475	-3.43285333	-0.16019324	0.011886681	-13.4767004	-0.00598066	0.298793142	-0.01199942
0.078065782	73978.20038	8.681513588	60.49365936	-2.3568748	-0.11919362	0.007878218	-15.1295153	-0.00410578	0.221633134	-0.00906607
0.078101334	74011.89077	8.68942268	60.52120876	-1.25384206	-0.04580285	0.003166992	-14.462572	-0.00313177	0.079489357	-0.00640285
0.078099293	74009.95664	8.688968529	60.51962718	-0.17088074	0.003877934	0.005319256	0.72903686	7.95639E-05	-0.01694562	-0.00070843
0.078092315	74003.34415	8.687415951	60.51422	0.941542473	0.088943145	0.004965902	17.91077214	0.000166977	-0.184634	-0.00018397
0.078144268	74052.57626	8.698978728	60.55447821	1.938464771	0.139818629	0.008452399	16.54188707	0.001175851	-0.28403951	0.002941709
0.078214323	74118.96352	8.714582781	60.60876458	3.016941521	0.182680868	0.010186792	17.93311106	0.002967921	-0.36906617	0.007992812
0.078266848	74168.73792	8.726291224	60.64946625	4.096734729	0.228422977	0.013468744	16.95948605	0.003891447	-0.4627797	0.011248106
0.078313176	74212.64039	8.736624934	60.6853663	5.17419043	0.270015826	0.018583143	14.53014861	0.005448505	-0.54264084	0.014771046
0.078346705	74244.41414	8.744107616	60.71134842	6.251897371	0.313164244	0.024318821	12.87744375	0.004982611	-0.62744835	0.014720116
0.078388599	74284.11417	8.753461428	60.74381204	7.235061742	0.345692333	0.030768165	11.23539049	0.006085971	-0.68548276	0.015961846
0.078441877	74334.60266	8.765364357	60.78509763	8.304015658	0.377958821	0.037659093	10.0363231	0.011484559	-0.75099768	0.024416436
0.078473287	74364.36827	8.772385544	60.80943764	9.369282219	0.405641091	0.045232375	8.967936995	0.011541431	-0.80785461	0.023755866
0.07849076	74380.92639	8.776292535	60.8229776	10.43404087	0.431448901	0.057594813	7.491103242	0.013372684	-0.86216602	0.024412481
0.078500622	74390.27188	8.778498043	60.83061961	11.51257607	0.475626819	0.076205185	6.241397042	0.013772828	-0.96236753	0.028668377
0.07846667	74358.09758	8.770906163	60.80430995	12.48588366	0.495900772	0.095409519	5.197602673	0.011519374	-1.01341186	0.022073264
0.078439293	74332.1536	8.764786789	60.78309497	13.53864899	0.508041236	0.113831458	4.463100483	0.016014152	-1.04421689	0.030885658
0.078450856	74343.11161	8.767371181	60.79205558	14.60169218	0.531716144	0.132745551	4.005528921	0.013082111	-1.10136549	0.024618764
0.078444334	74336.93063	8.765913381	60.78700125	15.66946678	0.562516454	0.153371219	3.667679363	0.015057558	-1.17676125	0.032568303
0.078346619	74244.33251	8.744088386	60.71128166	16.73153163	0.584975068	0.176156033	3.320777928	0.014810285	-1.22038935	0.031383916
0.078278287	74179.57796	8.728842172	60.6583304	17.80069465	0.617501495	0.196418652	3.143802662	0.016257344	-1.29076935	0.033237147
0.078296138	74196.49403	8.732823713	60.67216305	18.87795302	0.658849027	0.222965472	2.954937467	0.015918652	-1.39182743	0.031897642
0.078292281	74192.83927	8.731963413	60.66917447	19.938537	0.680709808	0.244206662	2.787433401	0.015552653	-1.43508794	0.037216086
0.078256895	74159.30587	8.724071916	60.64175344	21.09572656	0.715569187	0.265320038	2.697003938	0.018102465	-1.51903116	0.044333914
0.078207692	74112.67937	8.713105119	60.60362589	22.15518057	0.733725207	0.291944258	2.513237326	0.015014329	-1.5608385	0.037073078
0.078172604	74079.42855	8.705288565	60.57643594	23.30285718	0.754457928	0.312572829	2.413702845	0.014405311	-1.60822222	0.036518534
0.078157282	74064.90907	8.701876447	60.56456303	24.36164002	0.774079506	0.339217518	2.281956165	0.016341989	-1.65991374	0.038911499
0.078106806	74017.07625	8.690640333	60.52544905	25.51003764	0.795708601	0.362125829	2.197326281	0.015891398	-1.71387759	0.040257357

Table 7: Unpainted model - 90 mph alpha sweep, beta = 0°.

Mach #	Reynolds #	q_c	Uinf	Alpha_c	C_L	C_D_c	L/D	Cl_cg_w	Cm_cg_c_w	Cn_cg_w/r
0.116387525	110293.3886	19.29687059	90.18941584	-10.6324347	-0.35362028	0.068749852	-5.7969099	-0.01155334	0.550457126	-0.01839151
0.116448515	110351.1849	19.31709991	90.2366772	-9.83887286	-0.34048465	0.061001514	-6.61755023	-0.00894575	0.543169388	-0.01507888
0.116471528	110372.9932	19.32473583	90.25451041	-8.776861	-0.31684869	0.051451766	-7.51163713	-0.01001057	0.515040365	-0.01658942
0.116445519	110348.3456	19.31610588	90.23435544	-7.71550722	-0.2952741	0.042181043	-8.81373914	-0.01170732	0.486248461	-0.01781497
0.116379106	110285.4099	19.2940788	90.1828915	-6.65590271	-0.27463101	0.03350157	-11.3056256	-0.00851579	0.464366487	-0.01550132
0.116317194	110226.7399	19.27355601	90.13491571	-5.58357887	-0.23941821	0.024291536	-13.1128183	-0.00834831	0.422657682	-0.01380112
0.116288567	110199.6117	19.26407026	90.1127324	-4.50745257	-0.19823487	0.018258333	-14.8321457	-0.00649326	0.352414963	-0.01153173
0.116304491	110214.7018	19.26934642	90.12507187	-3.43113989	-0.15806305	0.013365219	-13.6772741	-0.00602583	0.281415254	-0.01077781
0.116327787	110236.7784	19.2770667	90.14312441	-2.43850047	-0.11251661	0.01155662	-15.0145607	-0.00464185	0.195129178	-0.0074684
0.116336171	110244.7233	19.27984544	90.14962113	-1.25995918	-0.05340778	0.007493833	-7.17464288	-0.00237593	0.085228367	-0.00316542
0.116335782	110244.3543	19.2797164	90.14931945	-0.15331917	0.02571086	0.007443963	3.086605665	-0.00037999	-0.06166113	-0.0006495
0.116367014	110273.9517	19.29006988	90.17352191	0.940590426	0.08775295	0.008329817	7.622159632	0.000855984	-0.17728577	0.000559473
0.116448203	110350.8888	19.31699627	90.23643512	1.928104939	0.126939062	0.011513737	9.563128846	0.002456431	-0.24722928	0.004033958
0.116467486	110369.1626	19.32339448	90.25137804	3.006520379	0.169725079	0.0132738	9.969963933	0.003651976	-0.32720651	0.007268884
0.116493926	110394.2185	19.33216902	90.27186679	4.084510959	0.213226122	0.01702364	10.31740014	0.003835294	-0.40937069	0.009586745
0.116579488	110475.3002	19.36057739	90.33816911	5.166758032	0.260775709	0.020666652	12.61625983	0.005059054	-0.50118914	0.012274173
0.116689048	110579.1232	19.39698405	90.42306756	6.237245884	0.294949199	0.025541132	9.159900152	0.004556222	-0.55549898	0.00992963
0.11677121	110656.9832	19.42430892	90.48673543	7.217361005	0.323686416	0.032200045	8.552396459	0.007493724	-0.60870095	0.014358902
0.116791827	110676.5208	19.43116864	90.50271177	8.284169641	0.353285083	0.037847452	7.505819848	0.009088496	-0.66753786	0.018270853
0.116827014	110709.8658	19.44287899	90.52997875	9.345189284	0.375688234	0.047068154	6.305247642	0.011173467	-0.71138344	0.019313186
0.116884723	110764.5527	19.46209197	90.57469747	10.41182331	0.403827349	0.059583422	5.108753263	0.013080865	-0.76815229	0.02147233
0.116901226	110780.1917	19.46758814	90.58748588	11.48403343	0.440141995	0.079046164	4.571858207	0.011071445	-0.84732464	0.021636265
0.116865155	110746.0097	19.45557627	90.55953448	12.45946029	0.463050669	0.096272014	4.011668504	0.012273068	-0.90146778	0.021908084
0.116829435	110712.1601	19.44368486	90.53185487	13.51921702	0.483882987	0.115425955	3.629328687	0.013292442	-0.95353886	0.024257611
0.116805445	110689.4255	19.4357002	90.51326425	14.5854269	0.511494795	0.133325755	3.319084637	0.013300381	-1.01533418	0.026368102
0.116774134	110659.7541	19.42528172	90.48900126	15.65293678	0.541966002	0.154107187	3.053839926	0.013922808	-1.08476047	0.028074446
0.116734199	110621.9099	19.41199761	90.45805519	16.72251974	0.573771288	0.177470337	2.862564723	0.016540184	-1.15787842	0.037541796
0.116662409	110553.8789	19.38812874	90.40242476	17.79074683	0.605134154	0.200439586	2.698367102	0.016933614	-1.23151975	0.040526262
0.116565291	110461.8462	19.35586212	90.32716749	18.86169642	0.638638466	0.224259388	2.570650652	0.019297631	-1.30911177	0.04847983
0.116479016	110380.0893	19.32722073	90.26031298	20.0146468	0.667170871	0.248434561	2.446521625	0.023211968	-1.37760114	0.055470922
0.116402746	110307.8123	19.30191806	90.20121047	21.07819803	0.691477389	0.272701808	2.554567351	0.028380473	-1.43391548	0.065299157
0.116353651	110261.2885	19.28563981	90.16316689	22.08164135	0.642299672	0.270682779	3.25692819	0.031398137	-1.22286109	0.070561624
0.116330851	110239.6823	19.27808232	90.14549899	23.04651737	0.435770756	0.197210265	2.107908211	0.00756865	-0.41702794	0.016581309
0.116267423	110179.5751	19.25706567	90.09634801	24.08783015	0.433673161	0.206731372	1.985417901	0.004169107	-0.3724788	0.008818745
0.116159564	110077.3634	19.22135335	90.01276719	25.23279324	0.451032383	0.218429158	1.929590308	0.003307259	-0.40858125	0.010564939
0.116035149	109959.4635	19.18020077	89.91635769	26.36639598	0.455511389	0.233745154	1.948752229	0.004373578	-0.44048163	0.009536203

122

Table 8: Unpainted model - 110 mph alpha sweep, beta = 0°.

Mach #	Reynolds #	q_c	Uinf	Alpha_c	C_L	C_D_c	L/D	Cl_cg_w	Cm_cg_c_w	Cn_cg_w/r
0.143051971	135561.6643	29.15155387	110.8518604	-10.6170967	-0.33454684	0.064279324	-5.2045794	-0.01011093	0.46939773	-0.01450436
0.143057688	135567.082	29.15388396	110.8562906	-8.77180155	-0.31055867	0.049525957	-6.27062433	-0.00950856	0.459868852	-0.01304995
0.143040474	135550.7691	29.14686818	110.8429512	-6.6396003	-0.2543635	0.031287217	-8.12994966	-0.00886681	0.400770971	-0.01393761
0.143023874	135535.0385	29.14010363	110.8300879	-4.50048021	-0.18956668	0.017265112	-10.9797538	-0.0058167	0.323903655	-0.01046773
0.142982921	135496.2302	29.12341841	110.7983535	-2.34371125	-0.102903	0.009475517	-10.8598831	-0.00319581	0.171629428	-0.00579477
0.143021787	135533.0605	29.13925306	110.8284704	-0.14375107	0.037606127	0.006955243	5.406874249	-0.00060142	-0.09238096	-0.0002355
0.14315347	135657.8486	29.192936	110.9305125	1.9301325	0.12945977	0.010841376	11.94126773	0.002850869	-0.25755939	0.00569906
0.143290464	135787.6694	29.2488364	111.0366699	4.087270465	0.2166568	0.016159109	13.40771911	0.002713516	-0.41765972	0.00675993
0.143460536	135948.837	29.318309	111.1684603	6.237295496	0.295010878	0.024966872	11.81609307	0.006295928	-0.55648446	0.013000758
0.143606667	136087.3161	29.37806739	111.2816979	8.280451728	0.348663636	0.038371253	9.086584495	0.009049173	-0.65755952	0.016178512
0.14371742	136192.2703	29.4233992	111.3675213	10.413714	0.406177892	0.061812706	6.5711068	0.013134443	-0.7750957	0.024847784
0.14370094	136176.6527	29.41665141	111.3547504	12.45837944	0.461706934	0.099281967	4.65046118	0.015614732	-0.9083238	0.029846912
0.143566291	136049.0545	29.36155015	111.2504105	14.58449724	0.510339015	0.14042426	3.634265303	0.02261773	-1.02109277	0.049401355
0.143378229	135870.8388	29.28467698	111.1046795	16.61719627	0.334670604	0.11136597	3.005142463	0.004591353	-0.29086678	0.006522356
0.143243462	135743.1286	29.22965128	111.0002479	18.66659451	0.396083565	0.144239854	2.746006424	0.004784428	-0.40309639	0.011915781
0.143247782	135747.2221	29.23141419	111.0035952	20.91466698	0.488172062	0.192651752	2.533961184	0.01456723	-0.65387804	0.034022587
0.143105659	135612.5408	29.17343921	110.8934633	23.15974803	0.576541546	0.245071847	2.352540912	0.025379137	-0.91423232	0.05945347
0.142879571	135398.291	29.08133172	110.7182664	25.38502426	0.640289268	0.295285601	2.168372807	0.031610833	-1.11676186	0.074787127

Table 9: Unpainted model - 130 mph alpha sweep, beta = 0°.

Mach #	Reynolds #	q_c	Uinf	Alpha_c	C_L	C_D_c	L/D	Cl_cg_w	Cm_cg_c_w	Cn_cg_w/r
0.168687891	159855.2688	40.53608809	130.7172942	-10.595292	-0.30743874	0.059621274	-5.15652746	-0.00698316	0.451669572	-0.01271584
0.168717281	159883.1202	40.55021441	130.7400688	-8.83132546	-0.2763998	0.046330107	-5.96587886	-0.00632111	0.424037448	-0.01088893
0.168635547	159805.6655	40.51093516	130.6767324	-6.63581097	-0.24965253	0.030220821	-8.26094466	-0.00620964	0.402545004	-0.01015753
0.168582475	159755.3721	40.48544031	130.6356063	-4.49508327	-0.18285709	0.016405355	-11.1461827	-0.0037346	0.320291331	-0.00874666
0.168495067	159672.5411	40.44346889	130.5678735	-2.42924411	-0.10100442	0.010624837	-9.50644491	-0.00152079	0.180507761	-0.00503317
0.168622348	159793.1577	40.50459395	130.6665045	-0.14845021	0.03176405	0.00660554	4.808698262	-0.00078541	-0.07635097	0.000963407
0.168865585	160023.6583	40.62153346	130.8549901	1.927948151	0.12674414	0.010376228	12.21485687	0.001741997	-0.2573815	0.005954509
0.168988685	160140.3132	40.68078005	130.9503814	4.084726548	0.213494148	0.01615427	13.2159575	0.003081458	-0.42060724	0.010848061
0.16909443	160240.5209	40.73170794	131.0323236	6.234636607	0.29170529	0.024258844	12.02469868	0.005514163	-0.56528772	0.01598211
0.169253456	160391.2203	40.80835682	131.1555539	8.277897679	0.345488387	0.03660677	9.437827541	0.009336676	-0.67082229	0.024056443
0.169347528	160480.3664	40.85373233	131.2284507	10.29608153	0.259934667	0.042693833	6.088341649	0.005183999	-0.28148536	0.008239407
0.169342931	160476.0105	40.85151461	131.2248888	11.34967476	0.2731044	0.054923697	4.972432905	0.00601361	-0.28665462	0.006701413
0.169338289	160471.611	40.84927469	131.2212912	12.31638782	0.28517988	0.066015736	4.319877333	0.005820159	-0.29763454	0.005752029
0.16918203	160323.5342	40.77392131	131.1002054	13.37230126	0.301234152	0.077950773	3.864415186	0.006003607	-0.31580913	0.008174148
0.168989418	160141.0071	40.6811326	130.9509489	14.4474818	0.339998477	0.094372333	3.602734665	0.008159147	-0.40462064	0.018725284
0.16898174	160133.7313	40.6774361	130.9449993	15.5364603	0.397159929	0.114181808	3.478311786	0.012156692	-0.55579668	0.03279084
0.168977443	160129.6598	40.67536759	130.9416699	16.72033025	0.462888995	0.13974944	3.312277988	0.015146938	-0.73637112	0.045406287
0.168927583	160082.4102	40.65136694	130.9030328	17.7269106	0.525771577	0.167556988	3.137867205	0.017919767	-0.91048704	0.060039024
0.168803348	159964.68	40.59159604	130.8067622	18.90437472	0.583536778	0.194181026	3.005117388	0.020456488	-1.06807447	0.064505429

Table 10: Unpainted model - 145 mph alpha sweep, beta = 0°.

Mach #	Reynolds #	q_c	Uinf	Alpha_c	C_L	C_D_c	L/D	Cl_cg_w	Cm_cg_c_w	Cn_cg_w/r
0.18857141	178697.6717	50.65539576	146.1251561	-10.5897186	-0.30050978	0.05893853	-5.09869826	-0.00799652	0.373956202	-0.01135785
0.188638098	178760.8679	50.69123051	146.1768331	-9.79563825	-0.28673444	0.052383901	-5.47371304	-0.00985901	0.36519221	-0.01140514
0.188558326	178685.2733	50.64836686	146.1150177	-8.82477651	-0.26825802	0.045556309	-5.88849327	-0.00933953	0.351743228	-0.01059851
0.188457734	178589.948	50.59434134	146.037068	-7.76833732	-0.25279034	0.038220751	-6.61403396	-0.00877603	0.342285443	-0.01004854
0.18843348	178566.9644	50.58131973	146.0182738	-6.62512004	-0.23636134	0.02997558	-7.88512984	-0.00852629	0.330147349	-0.01041323
0.18840154	178536.6965	50.56417362	145.993523	-5.55758294	-0.2070995	0.021357154	-9.69696125	-0.00646555	0.299636294	-0.00911879
0.188262091	178404.5488	50.48934907	145.8854629	-4.48961015	-0.17605279	0.015953735	-11.0352086	-0.00565178	0.268159102	-0.007829
0.188173539	178320.6342	50.44186376	145.816844	-3.42164994	-0.14626438	0.013027393	-11.2274489	-0.0047286	0.231029038	-0.00675713
0.188214387	178359.3431	50.46376543	145.8484971	-2.42716317	-0.09841736	0.011272083	-8.73107169	-0.00265921	0.156918777	-0.00473319
0.188251107	178394.1403	50.48345791	145.8769516	-1.33529743	-0.03890964	0.007961664	-4.88712428	-0.00289245	0.053756441	-0.00292456
0.188309856	178449.8128	50.5149722	145.9224763	-0.23876225	0.027646445	0.007196445	3.841696855	-0.0012055	-0.06784995	-0.00030865
0.188375588	178512.1037	50.55024455	145.973413	0.850016766	0.083316688	0.006716563	12.40466177	-0.00106276	-0.16638861	9.16077E-05
0.188479005	178610.1057	50.6057633	146.0535514	1.926842985	0.125370174	0.00744857	16.8314413	0.000673502	-0.23719387	0.002082541
0.18862509	178748.5409	50.68423963	146.166753	3.006176089	0.16929705	0.010511993	16.1051328	0.001381234	-0.3160603	0.003460421
0.188701329	178820.7884	50.72521955	146.2258315	4.084320443	0.212989269	0.013713242	15.53164982	0.002195325	-0.3923672	0.005759212
0.188760339	178876.7088	50.75694985	146.2715589	5.163601514	0.256851458	0.016830684	15.26090421	0.00421774	-0.47012157	0.010513798
0.188899558	179008.6378	50.83184817	146.3794042	6.234773352	0.291875294	0.025967442	11.24004802	0.008269473	-0.53930206	0.018330868
0.189006121	179109.6215	50.88921565	146.4620169	7.197510805	0.299008219	0.031963018	9.35481818	0.010529783	-0.52244101	0.021725877
0.189090254	179189.3493	50.93453073	146.5272121	8.191642682	0.238254314	0.026824968	8.881811796	0.006648849	-0.27108372	0.006967202
0.189162508	179257.8196	50.97346354	146.5832018	9.245426719	0.251661262	0.034067572	7.387120633	0.00764317	-0.27544294	0.007572923
0.189123938	179221.2695	50.95267897	146.5533139	10.30664749	0.273070641	0.046811923	5.833353463	0.005930268	-0.30091582	0.008554974
0.189026008	179128.4673	50.89992522	146.4774275	11.37730982	0.307460897	0.06111398	5.030942143	0.00962872	-0.3844903	0.016638546
0.188946723	179053.3333	50.85723509	146.4159887	12.36167225	0.341478458	0.074094872	4.608665215	0.013748319	-0.47220298	0.024190093
0.188786183	178901.1995	50.77084945	146.2915855	13.44404531	0.390427659	0.091136901	4.283969012	0.018839186	-0.60195584	0.038623572
0.188613697	178737.7446	50.67811722	146.1579246	14.53248685	0.445678584	0.113881183	3.913540175	0.024097972	-0.75153194	0.052417442
0.188547585	178675.0944	50.64259657	146.1066941	15.62190302	0.50338417	0.137194933	3.669116341	0.023827663	-0.90507249	0.052316213
0.188461815	178593.8159	50.59653289	146.0402309	16.78883069	0.561570251	0.163478337	3.435135579	0.023758647	-1.06076416	0.054166299
0.18839775	178533.1045	50.56213905	145.9905858	17.80312179	0.620518966	0.191656049	3.237669616	0.020092224	-1.22148346	0.047283758
0.188273944	178415.7816	50.49570711	145.8946481	18.89242726	0.676843704	0.221315748	3.058271764	0.014704286	-1.37878803	0.033141747
0.18813664	178285.6669	50.4220832	145.7882504	20.06272905	0.726947758	0.249715103	2.911108493	0.012163625	-1.52050692	0.030755555
0.18799856	178154.8167	50.34809721	145.6812512	21.14249156	0.771408486	0.272754371	2.828033477	0.004921318	-1.64450795	0.014751689
0.187816607	177982.3906	50.25068615	145.5402545	22.22208528	0.816902589	0.287212936	2.844240235	-0.00741526	-1.76400535	-0.0139256
0.187686979	177859.5505	50.18134592	145.4398053	23.3856036	0.857330071	0.295054355	2.905668245	-0.01387025	-1.86201191	-0.02600519
0.187537265	177717.6751	50.10132032	145.3237906	24.44837902	0.881915296	0.325364743	2.710543517	-0.02266084	-1.9486586	-0.04343849
0.187332782	177523.8992	49.99212312	145.1653356	25.57730753	0.879339977	0.368249462	2.387892087	-0.0285567	-1.9891427	-0.05460172

Table 11: Painted model - 110 mph full view alpha sweep, beta = 0°.

Mach #	Reynolds #	q_c	Uinf	Alpha_c	C_L	C_D_c	L/D	Cl_cg_w	Cm_cg_c_w	Cn_cg_w/r
0.142399666	134943.5145	28.88630272	110.3463852	0.027447515	0.034123343	0.011067665	3.083156497	-0.00419743	-0.0677572	-0.00429076
0.14246752	135007.8159	28.91383828	110.398966	2.08616571	0.107123068	0.013869721	7.723520166	-0.00329393	-0.1809157	-0.00345627
0.142632186	135163.8597	28.98071491	110.5265666	4.226780634	0.173778298	0.017736947	9.797531461	-0.00593488	-0.27760952	-0.00505742
0.142703479	135231.4192	29.00969325	110.5818115	6.276057378	0.235040209	0.023319559	10.07910166	-0.00572034	-0.36198545	-0.00605067
0.142734718	135261.0232	29.02239587	110.6060194	8.395136924	0.274922193	0.031139568	8.828709419	-0.00585143	-0.41258224	-0.00658173
0.142666143	135196.0382	28.99451542	110.5528796	10.42056525	0.306535231	0.048898927	6.268751729	-0.00622779	-0.43560068	-0.00526996
0.142473914	135013.8745	28.91643339	110.4039202	12.62097586	0.339369471	0.07650091	4.436149469	-0.00752788	-0.47825243	-0.00329337
0.142379323	134924.2368	28.87805005	110.3306214	14.6464634	0.371056141	0.105159913	3.528494161	-0.01289879	-0.51024904	0.001590858
0.142285598	134835.419	28.84004294	110.2579931	16.76432355	0.409422144	0.132099721	3.099341474	-0.008904	-0.5403468	0.011326587
0.142167178	134723.2001	28.79205776	110.1662291	18.98277193	0.464681317	0.166053566	2.79838204	-0.00885421	-0.63301242	0.004134999
0.141975801	134541.8436	28.71459357	110.0179298	21.10866467	0.513033613	0.201223198	2.549574891	-0.00674598	-0.72433257	-0.00324891

	alpha_c	RightForeOut	RightForeIn	RightAftOut	RightAftIn	LeftForeOut	LeftForeIn	LeftAftOut	LeftAftIn	
	0.027447515	-0.21819369	-0.21045064	-0.28023605	-0.25969077	-0.22216738	-0.22808496	-0.27451073	-0.25060944	
	2.08616571	-0.22827125	-0.22027586	-0.2941092	-0.26592911	-0.23047126	-0.2369023	-0.2902931	-0.25951149	
	4.226780634	-0.23462297	-0.2296213	-0.30915976	-0.27247337	-0.23881065	-0.24700184	-0.30475148	-0.26698225	
	6.276057378	-0.24447774	-0.23549944	-0.32091656	-0.28125437	-0.24826028	-0.25347337	-0.31594675	-0.2770355	
	8.395136924	-0.25361851	-0.24126901	-0.32990488	-0.28654044	-0.25840213	-0.25844635	-0.32448538	-0.28269591	
	10.42056525	-0.26717203	-0.24749141	-0.34019978	-0.29254406	-0.27028159	-0.2646213	-0.33472189	-0.28866272	
	12.62097586	-0.28155366	-0.25262424	-0.35353939	-0.30075758	-0.28209715	-0.27002047	-0.34950303	-0.29709091	
	14.6464634	-0.30073508	-0.26381437	-0.37442515	-0.31029577	-0.30042515	-0.27663473	-0.36637126	-0.30643916	
	16.76432355	-0.32782424	-0.27650909	-0.40614545	-0.3218	-0.32506667	-0.28945455	-0.39325455	-0.31874545	
	18.98277193	-0.36106526	-0.28986743	-0.44184337	-0.3336506	-0.35660843	-0.30208434	-0.4243494	-0.33089157	
	21.10866467	-0.39830458	-0.30290964	-0.47566265	-0.34428313	-0.39113855	-0.31581949	-0.45446988	-0.34331325	

Table 12: Painted model - 110 mph wing view alpha sweep, beta = 0°.

Mach #	Reynolds #	q_c	Uinf	Alpha_c	C_L	C_D_c	L/D	Cl_cg_w	Cm_cg_c_w	Cn_cg_w/r
0.142226879	134779.7748	28.81624431	110.2124916	14.64685016	0.371536966	0.105263872	3.529577243	-0.01399361	-0.51141342	-0.00330948
0.14202014	134583.8608	28.73253143	110.0522883	15.70589118	0.391479507	0.118863241	3.29352879	-0.01061252	-0.53292584	0.002888372
0.1418464	134419.218	28.66227467	109.917656	16.77055491	0.417169097	0.134140859	3.109933096	-0.01067938	-0.56671035	0.006062176
0.141685077	134266.3416	28.59711592	109.7926455	17.92151337	0.443225113	0.15073301	2.940464819	-0.01115432	-0.60563614	0.004801347
0.141501325	134092.2114	28.52298874	109.6502553	18.98665924	0.469514113	0.167585863	2.801633171	-0.00959247	-0.64905964	0.002779249

	alpha_c	RightForeOut	RightForeIn	RightAftOut	RightAftIn	LeftForeOut	LeftForeIn	LeftAftOut	LeftAftIn	
	14.64685016	-0.30817482	-0.26329205	-0.37113097	-0.30612219	-0.29780428	-0.27295917	-0.3639052	-0.30500306	
	15.70589118	-0.31909811	-0.26848631	-0.38438012	-0.30960112	-0.30803033	-0.27643646	-0.37554589	-0.31031562	
	16.77055491	-0.33440657	-0.27515994	-0.40150565	-0.31511018	-0.32018362	-0.28147402	-0.38914863	-0.31585299	
	17.92151337	-0.35066762	-0.28157164	-0.41826119	-0.31960389	-0.33441791	-0.2857806	-0.40368358	-0.32108806	
	18.98665924	-0.36859352	-0.28785417	-0.43539423	-0.32400962	-0.34977244	-0.29153332	-0.41839583	-0.32673077	

Table 13: Painted model - 145 mph full view alpha sweep, beta = 0°.

Mach #	Reynolds #	q_c	Uinf	Alpha_c	C_L	C_D_c	L/D	Cl_cg_w	Cm_cg_c_w	Cn_cg_w/r
0.188693301	178813.1807	50.72090358	146.2196105	0.023764907	0.029545044	0.009551007	3.093395591	-0.00288712	-0.05456497	-0.00338813
0.188706784	178825.9579	50.72815239	146.2300587	2.088107894	0.109537634	0.013517421	8.103441648	-0.00431709	-0.18352552	-0.0031939
0.188800058	178914.3482	50.77831271	146.3023374	4.231988323	0.18025261	0.017286203	10.42754238	-0.00627043	-0.2839061	-0.00545363
0.18883339	178945.9344	50.79624349	146.3281662	6.279177114	0.238918732	0.022418829	10.65705657	-0.00589826	-0.3601765	-0.00652629
0.188701091	178820.5627	50.72509151	146.2256469	8.388077505	0.266145771	0.025630453	10.38396652	-0.00626407	-0.36266363	0.007497303
0.188467801	178599.4879	50.59974674	146.044869	10.50655861	0.305283753	0.050663829	6.025674711	-0.00551475	-0.4113505	-0.00151237
0.188187163	178333.5443	50.44916781	145.8274008	12.62276523	0.341594055	0.077560767	4.404211925	-0.00533526	-0.46855762	0.00058764
0.187927506	178087.4832	50.31004633	145.6261911	14.67445782	0.405859405	0.104356011	3.889180897	-0.00444805	-0.6016574	0.018614416
0.187717082	177888.0776	50.19744451	145.4631326	16.92982941	0.507022322	0.147565842	3.435905738	-0.00033785	-0.85292131	0.028224241
0.187450845	177635.7806	50.05515635	145.2568236	19.09693847	0.606615628	0.202090849	3.001697662	0.002568057	-1.11437978	0.025966866
0.187165514	177365.39	49.90288812	145.035719	21.24510826	0.682663228	0.240061829	2.843697524	-0.00267687	-1.30552814	-0.00359706

	alpha_c	RightForeOut	RightForeIn	RightAftOut	RightAftIn	LeftForeOut	LeftForeIn	LeftAftOut	LeftAftIn	
	0.023764907	-0.38302422	-0.36883553	-0.48870395	-0.44452542	-0.37899342	-0.38691089	-0.48236842	-0.43923684	
	2.088107894	-0.39596604	-0.38214118	-0.51563529	-0.45806974	-0.39753529	-0.39825882	-0.50929412	-0.45469412	
	4.231988323	-0.41916143	-0.39872189	-0.54298225	-0.46981065	-0.41513609	-0.414848	-0.53602367	-0.46849112	
	6.279177114	-0.43843985	-0.41457435	-0.56384618	-0.48059043	-0.4332688	-0.43339181	-0.55535673	-0.4805848	
	8.388077505	-0.45777654	-0.425	-0.58018816	-0.48944784	-0.45220007	-0.44072388	-0.57058824	-0.49061765	
	10.50655861	-0.48214164	-0.43188249	-0.59903042	-0.50523636	-0.47137228	-0.45087654	-0.59245679	-0.50614198	
	12.62276523	-0.50985968	-0.44801807	-0.62260241	-0.5195	-0.49366302	-0.45818528	-0.61377711	-0.52231325	
	14.67445782	-0.54646459	-0.46766272	-0.66349112	-0.53630644	-0.52807692	-0.47671598	-0.64847337	-0.53903952	
	16.92982941	-0.59645281	-0.49088312	-0.7265974	-0.56022944	-0.57491558	-0.49835065	-0.6997987	-0.56278528	
	19.09693847	-0.65989494	-0.51525447	-0.79011515	-0.58050303	-0.63271515	-0.52158788	-0.75384242	-0.5850303	
	21.24510826	-0.72834305	-0.53960234	-0.85190643	-0.6008538	-0.69521637	-0.5321108	-0.80917544	-0.60778947	

Table 14: Painted model - 145 mph wing view alpha sweep, beta =0°.

Mach #	Reynolds #	q_c	Uinf	Alpha_c	C_L	C_D_c	L/D	Cl_cg_w	Cm_cg_c_w	Cn_cg_w/r
0.19044016	180468.5724	51.66436432	147.5732619	5.218302595	0.217939966	0.020199885	10.78916881	-0.00436855	-0.3625292	-0.00694876
0.189899601	179956.3182	51.37148537	147.1543801	6.283821079	0.24469221	0.023095376	10.59485718	-0.0032879	-0.39928139	-0.00758173
0.189443374	179523.9795	51.12494553	146.8008469	7.343055286	0.264874926	0.026543656	9.97884114	-0.00248591	-0.42319516	-0.00647735
0.189019528	179122.3266	50.8964355	146.4724061	8.398790963	0.279464973	0.031625747	8.836628332	-0.00166795	-0.43445825	-0.00451123
0.188628721	178751.9818	50.686191	146.1695668	9.453305085	0.293779577	0.03967795	7.404101627	-0.00068577	-0.4384285	-0.00423771
	alpha_c	RightForeOut	RightForeIn	RightAftOut	RightAftIn	LeftForeOut	LeftForeIn	LeftAftOut	LeftAftIn	
	5.218302595	-0.43238819	-0.41589524	-0.56412698	-0.48802572	-0.43314984	-0.43861585	-0.55725873	-0.4829381	
	6.283821079	-0.44145107	-0.42093398	-0.57117552	-0.48842279	-0.43954267	-0.44131079	-0.56376329	-0.48741546	
	7.343055286	-0.45149396	-0.42510703	-0.57694091	-0.48974333	-0.44625879	-0.44194337	-0.5688115	-0.4912508	
	8.398790963	-0.4628413	-0.42875279	-0.58118099	-0.49020574	-0.45336364	-0.4410828	-0.57399841	-0.49390271	
	9.453305085	-0.47597038	-0.42671985	-0.5848744	-0.49313618	-0.45938318	-0.43656309	-0.58110556	-0.49885346	

Table 15: CFD - 110 mph turbulent and lamniar alpha sweeps, beta = 0°.

Angle	CL (Turb)	CD (Turb)	CL (Lam)	CD (Lam)	LIFT	DRAG	L/D Turb
6	0.197195	0.033912			6.02746263	1.03655424	5.81490328
8	0.241463	0.046488			7.38055838	1.42095227	5.1940931
10.087	0.284069	0.060538			8.68285343	1.85040459	4.69240807
12.087	0.31789	0.075419			9.71662616	2.30525725	4.21498561
14.174	0.349576	0.092774	0.346557	0.091307	10.6851405	2.83573021	3.76803846
16.261	0.394727	0.117023	0.383408	0.114004	12.065226	3.57692517	3.37307196
18.348	0.43849	0.143323	0.428128	0.141114	13.4028859	4.38081101	3.05945312
20.522	0.4832	0.173168			14.7694918	5.29305332	2.79035388
22.696	0.524638	0.204949			16.0360858	6.26447141	2.5598466

Table 16: Unpainted model - 90 mph alpha sweep, beta = 0°.

Mach #	Reynolds #	q_c	Uinf	Alpha_c	C_L	C_D_c	L/D	Cl_cg_w	Cm_cg_c_w	Cn_cg_w/r
0.11732844	111185.038	19.6101368	90.918538	-2.0750334	-0.0932831	0.00350948	-26.580306	-0.0036205	0.19301834	-0.0017217
0.11732715	111183.814	19.6097048	90.9175366	-0.0636218	0.02906431	-0.0037663	-7.7170132	-0.0001055	-0.0578098	-4.167E-05
0.11739943	111252.311	19.6338743	90.9735485	2.02281373	0.1365228	-0.0011496	-118.76114	0.00181756	-0.2819623	0.00076865
0.11747298	111322.007	19.6584821	91.0305409	4.1818605	0.2260929	0.00203394	111.160018	0.0016951	-0.4565366	0.00153722
0.11753987	111385.392	19.6808747	91.0823716	4.27007774	0.22760619	0.00593653	38.339911	0.0014498	-0.4625336	0.0009533
0.11767139	111510.032	19.7249451	91.1842926	6.33796495	0.31200504	0.01447229	21.5587823	0.00196612	-0.6285281	0.00177155
0.11783356	111663.711	19.779351	91.3099595	8.5634799	0.37604954	0.02739873	13.7250741	0.00263202	-0.7609897	0.00234296
0.11787528	111703.246	19.7933594	91.3422881	10.6110068	0.43513605	0.05291573	8.22318879	0.00332859	-0.8812079	0.00327049
0.11785968	111688.464	19.7881211	91.3302007	12.7449665	0.49351736	0.08942661	5.51868577	0.00370559	-1.0098826	0.00429772
0.11779417	111626.383	19.7661291	91.2794354	14.8475891	0.54621973	0.13055194	4.18392666	0.00314878	-1.1338711	0.00497383
0.11763469	111475.253	19.712643	91.1558531	17.0175436	0.61607048	0.18120982	3.99976322	0.00280355	-1.3006872	0.00454567
	alpha_c	RightForeOut	RightForeIn	RightAftOut	RightAftIn	LeftForeOut	LeftForeIn	LeftAftOut	LeftAftIn	
	-2.0750334	-0.1493	-0.144	-0.1805	-0.1655625	-0.1439375	-0.1451875	-0.174375	-0.165625	
	-0.0636218	-0.1535714	-0.1495625	-0.189	-0.171	-0.148125	-0.1505	-0.1823125	-0.17025	
	2.02281373	-0.1603839	-0.15675	-0.20025	-0.1778125	-0.153625	-0.1594375	-0.1939375	-0.17725	
	4.1818605	-0.1666282	-0.1623333	-0.209	-0.1828333	-0.159	-0.1648333	-0.2033333	-0.1825	
	4.27007774	-0.1643452	-0.162	-0.2114286	-0.1834286	-0.16125	-0.1658571	-0.2048571	-0.1834286	
	6.33796495	-0.1737143	-0.1672143	-0.2193571	-0.1889286	-0.1681429	-0.1713571	-0.2126429	-0.1882143	
	8.5634799	-0.1813352	-0.1714286	-0.2261429	-0.1935	-0.1757857	-0.176	-0.2195	-0.1931429	
	10.6110068	-0.189478	-0.1767857	-0.2340714	-0.1982143	-0.182989	-0.1804286	-0.2262857	-0.1982857	
	12.7449665	-0.1994167	-0.1830714	-0.2457143	-0.2046429	-0.1927857	-0.1857143	-0.2370714	-0.2045714	
	14.8475891	-0.2116667	-0.1879231	-0.2583077	-0.2102308	-0.2034359	-0.1895385	-0.2473077	-0.2101538	
	17.0175436	-0.2260096	-0.1956875	-0.2784375	-0.2173125	-0.22	-0.19725	-0.262375	-0.2164375	

Table 17: Unpainted model - 90 mph alpha sweep, beta = -2°.

Mach #	Reynolds #	q_c	Uinf	Alpha_c	C_L	C_D_c	L/D	Cl_cg_w	Cm_cg_c_w	Cn_cg_w/r
0.11670318	110592.511	19.4016813	90.4340154	-2.0671729	-0.0835108	-0.0002159	386.829071	-0.0028586	0.15874898	-0.00232
0.1171582	111023.711	19.5532702	90.786617	-0.0538725	0.04118487	-0.0055928	-7.3638885	0.00318808	-0.0974754	-0.0008877
0.11723638	111097.801	19.5793762	90.8472022	2.03519423	0.15191451	-0.0043086	-35.258614	0.00694053	-0.3277684	-0.0002123
0.11730586	111163.634	19.6025874	90.9010356	2.12213205	0.1518372	-0.0046985	-32.315968	0.00706015	-0.3270955	1.8691E-05
0.11742118	111272.924	19.6411506	90.9904042	4.27916688	0.23890601	0.00426482	56.0177898	0.00832543	-0.4952547	0.00109779
0.11755714	111401.765	19.6866614	91.0957608	6.43066068	0.31908609	0.01323149	24.1156508	0.01031363	-0.6507768	0.0015212
0.11769179	111529.362	19.7317843	91.2000993	8.56711997	0.38057494	0.02789701	13.6421431	0.01362197	-0.7732221	0.00267652
0.11778713	111619.705	19.7637644	91.2739752	10.6157751	0.44106407	0.05096222	8.65472596	0.01554924	-0.8998896	0.00317543
0.11777375	111607.032	19.7592768	91.2636122	12.7530956	0.50362362	0.08648249	5.82341724	0.01750075	-1.041286	0.0031528
0.11765478	111494.288	19.7193756	91.1714184	14.8861516	0.56088143	0.12712185	4.41215585	0.01916701	-1.175639	0.00273826
0.11754965	111394.663	19.6841512	91.0899531	17.0258567	0.62640557	0.17236029	3.63428006	0.01619044	-1.329293	0.00123162
	alpha_c	RightForeOu	RightForeIn	RightAftOut	RightAftIn	LeftForeOut	LeftForeIn	LeftAftOut	LeftAftIn	
	-2.0671729	-0.1460667	-0.1442	-0.1789333	-0.165	-0.1439333	-0.1469333	-0.1753333	-0.1654667	
	-0.0538725	-0.1504048	-0.1486667	-0.1879333	-0.1712667	-0.1488	-0.1544667	-0.1856	-0.1710667	
	2.03519423	-0.1572857	-0.1538571	-0.1971429	-0.176	-0.1555714	-0.1611429	-0.197	-0.1774286	
	2.12213205	-0.1576282	-0.155	-0.1968333	-0.1768333	-0.1541667	-0.1616667	-0.1973333	-0.1783333	
	4.27916688	-0.1625	-0.1603333	-0.20875	-0.183	-0.1623333	-0.16825	-0.20725	-0.1841667	
	6.43066068	-0.1680714	-0.165	-0.2164667	-0.1876667	-0.1697048	-0.1720667	-0.2148667	-0.1897333	
	8.56711997	-0.1756923	-0.1709231	-0.2237692	-0.1923846	-0.1788462	-0.1770769	-0.2214615	-0.1940769	
	10.6157751	-0.1844701	-0.1755556	-0.2335556	-0.1967778	-0.1862906	-0.1815556	-0.2283333	-0.1987778	
	12.7530956	-0.1929881	-0.1807857	-0.2431429	-0.2026429	-0.1943571	-0.1856429	-0.2370714	-0.2043571	
	14.8861516	-0.2045952	-0.1861429	-0.2563571	-0.2092857	-0.2059524	-0.1910714	-0.2487857	-0.2102857	
	17.0258567	-0.2188552	-0.1938824	-0.274	-0.2167059	-0.222	-0.199	-0.2666471	-0.2168235	

Table 18: Unpainted model - 90 mph alpha sweep, beta = -4°.

Mach #	Reynolds #	q_c	Uinf	Alpha_c	C_L	C_D_c	L/D	Cl_cg_w	Cm_cg_c_w	Cn_cg_w/r
0.11717784	111042.324	19.5598269	90.8018372	-0.0609273	0.0324141	-0.0010731	-30.205571	0.00625684	-0.0675845	-0.0013926
0.1172588	111119.041	19.5868633	90.8645705	2.02657087	0.14119375	1.0189E-05	13858.1117	0.01189838	-0.2882419	0.00027483
0.11735379	111209.059	19.6186109	90.9381801	4.27259997	0.23074189	0.0083485	27.6387138	0.01515664	-0.459893	0.00138685
0.11746225	111311.84	19.6548914	91.0222268	6.33361704	0.30659962	0.01691117	18.1300023	0.01873994	-0.6020163	0.00223439
0.11757457	111418.279	19.6924983	91.1092644	8.46921037	0.3670119	0.02790013	13.1544862	0.02512787	-0.7189472	0.00446283
0.11769703	111534.324	19.7335403	91.2041574	10.1743143	0.41569213	0.0466665	8.9077212	0.02702692	-0.8209301	0.00416433
0.11772207	111558.051	19.7419369	91.2235591	12.7426751	0.49066858	0.08386113	5.85096558	0.03120185	-0.9857157	0.00408161
0.11759022	111433.113	19.6977424	91.1213948	14.8726456	0.5440904	0.1238744	4.39227474	0.0355248	-1.1089494	0.00442053
0.11750115	111348.702	19.6679114	91.0523698	17.0112986	0.60830659	0.17185306	3.53969011	0.02967041	-1.2682487	0.00108834
0.11745532	111305.272	19.652572	91.016856	19.239323	0.67547083	0.21942249	3.07840282	0.03096623	-1.4206574	0.00478787
	alpha_c	RightForeOu	RightForeIn	RightAftOut	RightAftIn	LeftForeOut	LeftForeIn	LeftAftOut	LeftAftIn	
	-0.0609273	-0.1496	-0.1487333	-0.1846	-0.1710667	-0.1488	-0.1556667	-0.1862	-0.1717333	
	2.02657087	-0.1541548	-0.15475	-0.1936667	-0.1765833	-0.1561667	-0.1625833	-0.1985	-0.1791667	
	4.27259997	-0.1597857	-0.1593571	-0.2053571	-0.182	-0.1635	-0.1691429	-0.209	-0.1837143	
	6.33361704	-0.1669161	-0.1633636	-0.2130909	-0.1864545	-0.1709091	-0.1737273	-0.216	-0.189	
	8.46921037	-0.1719167	-0.1685714	-0.2212857	-0.1911429	-0.1791071	-0.1788571	-0.2227143	-0.1942857	
	10.1743143	-0.1776504	-0.1719474	-0.2281053	-0.1942105	-0.1856241	-0.1823158	-0.2275789	-0.1978947	
	12.7426751	-0.187978	-0.1783571	-0.2401429	-0.2018571	-0.1957143	-0.1864286	-0.2375	-0.2046429	
	14.8726456	-0.2008256	-0.1844	-0.2529333	-0.2090667	-0.2086462	-0.1930667	-0.2498	-0.2096667	
	17.0112986	-0.2144167	-0.1931333	-0.2686667	-0.2168667	-0.226	-0.1998	-0.2690667	-0.2154667	
	19.239323	-0.2325556	-0.2026111	-0.2899444	-0.2263889	-0.2510556	-0.2081667	-0.2962778	-0.2236667	

Table 19: Unpainted model - 90 mph alpha sweep, beta = -6°.

Mach #	Reynolds #	q_c	Uinf	Alpha_c	C_L	C_D_c	L/D	Cl_cg_w	Cm_cg_c_w	Cn_cg_w/r
0.11712821	110995.29	19.5432607	90.7633766	-2.0747079	-0.0928785	0.00393895	-23.579515	-0.0019454	0.18276158	-0.0045233
0.11706821	110938.437	19.5232451	90.7168863	-0.0570024	0.03729367	-0.0024201	-15.409833	0.00887324	-0.0794235	-0.0031101
0.11709964	110968.219	19.5337289	90.74124	2.03067532	0.14629649	-0.0013908	-105.18515	0.01620569	-0.3028714	-0.0023542
0.11725244	111113.02	19.5847409	90.8596473	4.27404347	0.23253647	0.00502627	46.264202	0.02070165	-0.4649952	-0.0011967
0.11738752	111241.025	19.629891	90.9643196	6.42358583	0.31029049	0.01520018	20.4136072	0.02630173	-0.6153527	-2.534E-05
0.11753414	111379.969	19.6789584	91.0779371	8.56060792	0.37247903	0.02430646	15.3242814	0.03458855	-0.7346391	0.00187082
0.11765358	111493.151	19.7189734	91.1704886	10.610747	0.43481304	0.04846677	8.97136456	0.03629256	-0.861136	0.00175156
0.11760919	111451.086	19.7040968	91.1360913	12.7418465	0.48963846	0.07869724	6.22179991	0.04303533	-0.9790045	0.00316856
0.11745859	111308.374	19.6536675	91.0193927	14.8709099	0.54193259	0.11988181	4.52055736	0.04652802	-1.1013261	0.00051177
0.11736633	111220.942	19.622804	90.9478978	17.0100962	0.60681167	0.16761896	3.62018512	0.04131459	-1.2629028	-0.0027285
		alpha_c	RightForeOu	RightForeIn	RightAftOut	RightAftIn	LeftForeOut	LeftForeIn	LeftAftOut	LeftAftIn
		-2.0747079	-0.1438714	-0.1437143	-0.1757143	-0.1652857	-0.144	-0.1503571	-0.179	-0.1659286
		-0.0570024	-0.1461429	-0.1481429	-0.1833571	-0.1703571	-0.1497857	-0.1565714	-0.19	-0.1717143
		2.03067532	-0.1508214	-0.1540833	-0.1905	-0.176	-0.1570833	-0.1631667	-0.2011667	-0.1790833
		4.27404347	-0.1575385	-0.1582308	-0.2000769	-0.1811538	-0.1661538	-0.1696923	-0.212	-0.1848462
		6.42358583	-0.1629167	-0.1623333	-0.2103333	-0.1857333	-0.1735833	-0.1746	-0.2191333	-0.1898667
		8.56060792	-0.1689286	-0.1673571	-0.218	-0.1894286	-0.1817857	-0.1797857	-0.2230714	-0.1953571
		10.610747	-0.1756209	-0.1726429	-0.2273571	-0.1954286	-0.1894286	-0.1845	-0.2302857	-0.1995714
		12.7418465	-0.1832308	-0.1773077	-0.2373077	-0.201	-0.1995385	-0.1880769	-0.2381538	-0.2043846
		14.8709099	-0.1948833	-0.1833333	-0.2483333	-0.2075333	-0.2114667	-0.1934	-0.251	-0.2084
		17.0100962	-0.2080667	-0.1911333	-0.2628	-0.2156	-0.2298	-0.2003333	-0.2702667	-0.2146667

Table 20: Unpainted model - 90 mph alpha sweep, beta = -8°.

Mach #	Reynolds #	q_c	Uinf	Alpha_c	C_L	C_D_c	L/D	Cl_cg_w	Cm_cg_c_w	Cn_cg_w/r
0.11701476	110887.782	19.5054207	90.6754652	-2.0755622	-0.0939405	0.00327783	-28.659332	-0.0014471	0.18626183	-0.0052111
0.11696945	110844.847	19.4903188	90.6403561	-0.0574007	0.03679852	-0.0034675	-10.612281	0.01153012	-0.0741735	-0.0033969
0.11702631	110898.727	19.5092711	90.6844146	2.02972844	0.14511931	-0.0026091	-55.620845	0.02097606	-0.2924787	-0.0028402
0.11719356	111057.216	19.5650739	90.8140152	4.27306166	0.23131587	0.00255189	90.6449192	0.02687886	-0.4523559	-0.0022242
0.11739514	111248.244	19.6324388	90.9702227	6.42172424	0.30797612	0.01072189	28.72405	0.03409202	-0.5964209	-0.0015316
0.11756442	111408.658	19.6890974	91.1013968	8.55838945	0.36972098	0.02537498	14.5702956	0.0435582	-0.715161	-0.0010739
0.11758915	111432.099	19.6973837	91.1205652	10.6057753	0.42863211	0.04488319	9.54994792	0.04687934	-0.8282674	0.00095091
0.11748737	111335.64	19.6632974	91.041689	12.7310933	0.4762699	0.07344031	6.48512954	0.05338789	-0.9233984	0.0020806
0.11730856	111166.2	19.6034922	90.9031336	14.8625367	0.5315228	0.10813673	4.91528454	0.05728245	-1.0517264	0.00036583
0.1172488	111109.563	19.583522	90.85682	17.0016027	0.59625236	0.16095643	3.70443327	0.0526783	-1.2176749	-0.0051134
		alpha_c	RightForeOu	RightForeIn	RightAftOut	RightAftIn	LeftForeOut	LeftForeIn	LeftAftOut	LeftAftIn
		-2.0755622	-0.1426125	-0.144125	-0.17575	-0.1656875	-0.14425	-0.15125	-0.18025	-0.16625
		-0.0574007	-0.1439286	-0.1481429	-0.1812143	-0.1707857	-0.1507143	-0.1567857	-0.1930714	-0.1734286
		2.02972844	-0.1482987	-0.1523636	-0.1888182	-0.1759091	-0.1590909	-0.1635455	-0.2034545	-0.1802727
		4.27306166	-0.1536758	-0.1577143	-0.1967143	-0.1805714	-0.1675714	-0.1706429	-0.2135	-0.1863571
		6.42172424	-0.1590595	-0.1615	-0.2045	-0.185	-0.1758929	-0.1760714	-0.2208571	-0.1907143
		8.55838945	-0.1655	-0.1666429	-0.2150714	-0.1887857	-0.1839286	-0.1798571	-0.2250714	-0.1941429
		10.6057753	-0.1716923	-0.1711429	-0.2245	-0.1948571	-0.1906429	-0.1840714	-0.2299286	-0.1991429
		12.7310933	-0.179359	-0.1757333	-0.2321333	-0.1994667	-0.1983795	-0.1886667	-0.2373333	-0.2032667
		14.8625367	-0.1907738	-0.1815714	-0.2424286	-0.2062143	-0.2125	-0.1928571	-0.2524286	-0.2082857
		17.0016027	-0.2031373	-0.1892353	-0.2567059	-0.2147059	-0.2337255	-0.2002941	-0.2781765	-0.2135294

Table 21: Unpainted model - 90 mph alpha sweep, beta = -10°.

Mach #	Reynolds #	q_c	Uinf	Alpha_c	C_L	C_D_c	L/D	Cl_cg_w	Cm_cg_c_w	Cn_cg_w/r
0.11687848	110758.64	19.4600142	90.5698625	-2.0718681	-0.0893479	0.00574414	-15.554615	-0.0007522	0.17129001	-0.0060146
0.11679575	110680.235	19.4324728	90.5057488	-0.0525917	0.04277713	-0.0003515	-121.69639	0.01487631	-0.089046	-0.004634
0.11689063	110770.151	19.4640592	90.579275	2.03120943	0.14696052	-0.0023659	-62.116748	0.02591217	-0.2953364	-0.0034921
0.1171386	111005.132	19.5467267	90.7714249	3.82288486	0.21787866	0.00323712	67.3063036	0.03157152	-0.4285829	-0.0036576
0.11730026	111158.328	19.600716	90.8966965	6.42467746	0.31164763	0.01347624	23.1257051	0.0416851	-0.6029631	-0.0036143
0.11739717	111250.168	19.6331179	90.9717962	8.53746315	0.37460788	0.02543223	14.7296506	0.05280747	-0.7192226	-0.0025637
0.11743812	111288.976	19.6468179	91.0035306	10.6078796	0.43124819	0.04977541	8.66388078	0.05711431	-0.830226	-0.0004328
0.11732438	111181.186	19.608778	90.9153879	12.7322205	0.47767127	0.07508426	6.36180261	0.06448014	-0.9165616	0.00224418
0.11712239	110989.78	19.5413202	90.7588706	14.8627508	0.53178908	0.11373434	4.67571236	0.06617159	-1.0482814	-0.0010536
0.11696093	110836.765	19.4874767	90.6337473	16.9976376	0.59132296	0.16005812	3.69442649	0.06447582	-1.1975768	-0.0048875
		-2.0718681	-0.1418	-0.1442667	-0.1748	-0.1651333	-0.1447333	-0.1519333	-0.1836	-0.1666
		-0.0525917	-0.1437143	-0.1477857	-0.1806429	-0.1701429	-0.1525714	-0.158	-0.1947857	-0.1746429
		2.03120943	-0.1473214	-0.15225	-0.186625	-0.175375	-0.160625	-0.1645	-0.205375	-0.18125
		3.82288486	-0.1516194	-0.1554737	-0.1926316	-0.1801053	-0.1686316	-0.1707895	-0.2131053	-0.1867895
		6.42467746	-0.1561833	-0.1605333	-0.2016667	-0.1846667	-0.1775833	-0.1763333	-0.2210667	-0.1907333
		8.53746315	-0.1621429	-0.1647143	-0.2092857	-0.1885714	-0.1847143	-0.1797857	-0.2242857	-0.1943571
		10.6078796	-0.1685385	-0.17	-0.2199231	-0.1943846	-0.1919231	-0.1853077	-0.2289231	-0.1993077
		12.7322205	-0.1760256	-0.1742	-0.2280667	-0.1991333	-0.2006462	-0.1888667	-0.2376667	-0.2034
		14.8627508	-0.1839881	-0.1795714	-0.2362857	-0.2045714	-0.2139286	-0.1927143	-0.2537143	-0.2064286
		16.9976376	-0.1954	-0.1867333	-0.2492667	-0.2131333	-0.2371333	-0.1982667	-0.2827333	-0.2119333

Table 22: Unpainted model - 90 mph alpha sweep, beta = -12°.

Mach #	Reynolds #	q_c	Uinf	Alpha_c	C_L	C_D_c	L/D	Cl_cg_w	Cm_cg_c_w	Cn_cg_w/r
0.11683274	110715.291	19.4447847	90.5344154	-2.0699426	-0.0869542	0.00623807	-13.939274	0.00033632	0.16651129	-0.0068246
0.11671692	110605.538	19.4062522	90.4446677	-0.0526599	0.0426924	-0.0006302	-67.748621	0.01818767	-0.0833778	-0.0053272
0.1167792	110664.558	19.4269683	90.4929296	2.09075901	0.14611365	-0.001227	-119.08482	0.03051081	-0.2862714	-0.0046259
0.11697324	110848.439	19.491582	90.6432933	4.27745654	0.23677968	0.00685221	34.5552499	0.03920026	-0.461693	-0.0046412
0.11717251	111037.274	19.558048	90.7977079	6.34025726	0.31485489	0.01700685	18.5134142	0.04926341	-0.6095162	-0.0048255
0.11730754	111165.23	19.6031501	90.9023403	8.53395097	0.37866954	0.02700571	14.0218299	0.06189534	-0.7200591	-0.0035255
0.11731115	111168.649	19.604356	90.9051362	10.613458	0.4381834	0.04726659	9.27046861	0.06793907	-0.8322655	0.0011004
0.11723205	111093.69	19.5779272	90.8438406	12.7366743	0.48320827	0.06962086	6.94056726	0.07520732	-0.9141686	0.00358087
0.11705837	110929.11	19.5199628	90.7092601	14.8632443	0.5324026	0.10912359	4.87889573	0.07652029	-1.0332407	0.0005861
0.116915	110793.242	19.472175	90.5981572	16.9961941	0.58952836	0.15333227	3.84477677	0.07573996	-1.182775	-0.0045697
		alpha_c	RightForeOu	RightForeIn	RightAftOut	RightAftIn	LeftForeOut	LeftForeIn	LeftAftOut	LeftAftIn
		-2.0699426	-0.1438	-0.1453333	-0.175	-0.1654	-0.1472667	-0.1539333	-0.1864667	-0.168
		-0.0526599	-0.1451429	-0.1484286	-0.1807857	-0.1702857	-0.1545714	-0.1604286	-0.1973571	-0.1755714
		2.09075901	-0.1484176	-0.1519231	-0.1859231	-0.1757692	-0.1633077	-0.1670769	-0.2072308	-0.1818462
		4.27745654	-0.1521949	-0.1561333	-0.1912	-0.1802	-0.1713333	-0.1742	-0.2167333	-0.1865333
		6.34025726	-0.1555595	-0.1597143	-0.1982143	-0.1842857	-0.1794643	-0.1781429	-0.2213571	-0.1915
		8.53395097	-0.1598896	-0.1645455	-0.2063636	-0.1880909	-0.1865714	-0.1823636	-0.2234545	-0.1948182
		10.613458	-0.1661209	-0.1690714	-0.2151429	-0.1928571	-0.1928571	-0.1868571	-0.2278571	-0.1992143
		12.7366743	-0.1732637	-0.173	-0.2234286	-0.1976429	-0.2003462	-0.1904286	-0.2357143	-0.2036429
		14.8632443	-0.1807292	-0.1775625	-0.232125	-0.20325	-0.2148125	-0.19425	-0.2571875	-0.206375
		16.9961941	-0.1912381	-0.1846429	-0.2432857	-0.2104286	-0.2375952	-0.1985714	-0.2933571	-0.2105714

Table 23: Unpainted model - 90 mph alpha sweep, beta = -14°.

Mach #	Reynolds #	q_c	Uinf	Alpha_c	C_L	C_D_c	L/D	Cl_cg_w	Cm_cg_c_w	Cn_cg_w/r
0.11674381	110631.02	19.4151951	90.4655049	-2.0660573	-0.0821239	0.00780543	-10.521385	0.00098958	0.15507368	-0.0082186
0.11662625	110519.611	19.3761112	90.3744029	-0.0502742	0.04565835	0.00063692	71.6861152	0.02145508	-0.0850981	-0.0069168
0.11674507	110632.21	19.4156128	90.4664781	2.2086308	0.15121403	7.8186E-05	1934.03266	0.03563029	-0.2908579	-0.0061707
0.11689866	110777.76	19.4667335	90.5854975	4.27591302	0.23486074	0.00961	24.4391957	0.04404286	-0.4493223	-0.0070221
0.1169749	110850.008	19.4921336	90.644576	6.42715495	0.31472769	0.01627287	19.3406337	0.05590817	-0.5942112	-0.0070427
0.11707911	110948.758	19.5268779	90.7253261	8.56335464	0.37589381	0.02678408	14.0342256	0.06908204	-0.6927091	-0.0048174
0.11712876	110995.815	19.5434455	90.7638057	10.6107245	0.43478501	0.04843786	8.97613932	0.07512288	-0.8039344	0.00090409
0.11704359	110915.105	19.515034	90.6978074	12.737284	0.48396629	0.0689754	7.01650521	0.08207181	-0.8983443	0.00333
0.11690596	110784.682	19.4691662	90.5911574	14.8600295	0.52840581	0.10372331	5.09437871	0.08451865	-0.9996024	0.00086422
0.11673847	110625.962	19.4134196	90.4613684	16.9856462	0.57641492	0.14628706	3.94030003	0.08562989	-1.1263937	-0.0037027

alpha_c	RightForeOut	RightForeIn	RightAftOut	RightAftIn	LeftForeOut	LeftForeIn	LeftAftOut	LeftAftIn
-2.0660573	-0.1448952	-0.1484762	-0.1740476	-0.1658095	-0.1482857	-0.1558571	-0.1894286	-0.1694286
-0.0502742	-0.1439381	-0.1502	-0.1798667	-0.1713333	-0.1572	-0.1624667	-0.2	-0.1763333
2.2086308	-0.1459832	-0.1531176	-0.1855882	-0.1756471	-0.1668235	-0.1700588	-0.2101765	-0.1834118
4.27591302	-0.1493187	-0.1557143	-0.1891429	-0.1795714	-0.1738571	-0.1749286	-0.2163571	-0.1865714
6.42715495	-0.1530595	-0.1592143	-0.1955714	-0.1832143	-0.18125	-0.1795714	-0.2209286	-0.1923571
8.56335464	-0.1573571	-0.1638571	-0.2024286	-0.1872857	-0.1867857	-0.1835714	-0.2216429	-0.1959286
10.6107245	-0.1641209	-0.1680714	-0.2098571	-0.1922857	-0.1935714	-0.1885	-0.2256429	-0.1988571
12.737284	-0.1690673	-0.172125	-0.220125	-0.197125	-0.2014712	-0.193	-0.2365	-0.20275
14.8600295	-0.17555	-0.1768	-0.2289333	-0.2031333	-0.2170667	-0.1951333	-0.2662	-0.2051333
16.9856462	-0.1847292	-0.1828125	-0.23825	-0.2105	-0.2427292	-0.1989375	-0.3024375	-0.2113125

Table 24: Unpainted model - 90 mph alpha sweep, beta = -16°.

Mach #	Reynolds #	q_c	Uinf	Alpha_c	C_L	C_D_c	L/D	Cl_cg_w	Cm_cg_c_w	Cn_cg_w/r
0.11668139	110571.863	19.3944372	90.4171311	-2.0635734	-0.0790358	0.00970225	-8.1461312	0.00258772	0.1489723	-0.0095598
0.11656887	110465.241	19.357052	90.3299439	-0.0495035	0.04661644	0.00160173	29.1037472	0.02453945	-0.0823552	-0.0082813
0.11666717	110558.388	19.3897102	90.4061117	2.20712885	0.14934677	0.00532778	28.0317009	0.03927582	-0.2814211	-0.0086799
0.11681504	110698.515	19.4388924	90.5206972	4.27543216	0.23426293	0.01142331	20.5074467	0.04902582	-0.438596	-0.0087053
0.11686405	110744.96	19.4552075	90.5586762	6.42473732	0.31172204	0.01862875	16.733382	0.06208834	-0.5762658	-0.0076909
0.11694576	110822.397	19.4824247	90.6219984	8.56413006	0.37685783	0.02974426	12.669936	0.07581342	-0.6799876	-0.0050001
0.11693767	110814.724	19.4797267	90.6157234	10.6115018	0.4357514	0.04586102	9.50156383	0.08185233	-0.7864213	0.00147423
0.11687995	110760.028	19.4605019	90.5709973	12.7350462	0.48118413	0.06768055	7.10963667	0.08825857	-0.8700417	0.00266704
0.1167596	110645.983	19.4204472	90.4777402	14.8552047	0.52240751	0.09946299	5.25228036	0.09272505	-0.9628262	0.00226899
0.1166124	110506.493	19.3715119	90.3636762	16.9754953	0.56379516	0.14320582	3.93695715	0.09448126	-1.0740816	-0.0028764

alpha_c	RightForeOut	RightForeIn	RightAftOut	RightAftIn	LeftForeOut	LeftForeIn	LeftAftOut	LeftAftIn
-2.0635734	-0.1447286	-0.1507143	-0.1737143	-0.1656429	-0.151	-0.1582143	-0.1912857	-0.1699286
-0.0495035	-0.1450714	-0.1522857	-0.1777857	-0.1702143	-0.1585714	-0.1646429	-0.2015714	-0.1768571
2.20712885	-0.1450381	-0.1568667	-0.1842667	-0.1748667	-0.1682667	-0.1714	-0.2105333	-0.1842667
4.27543216	-0.1471044	-0.158	-0.1871429	-0.1786429	-0.176	-0.1755	-0.2161429	-0.188
6.42473732	-0.1497738	-0.1582143	-0.1909286	-0.1813571	-0.1821071	-0.1809286	-0.2177857	-0.1914286
8.56413006	-0.1538714	-0.1631333	-0.1986667	-0.1858667	-0.1869048	-0.1857333	-0.2194	-0.1949333
10.6115018	-0.1588923	-0.1666667	-0.2072	-0.1908	-0.1928	-0.1899333	-0.2228667	-0.1985333
12.7350462	-0.164759	-0.1710667	-0.2165333	-0.1963333	-0.2015795	-0.1924	-0.2382	-0.2011333
14.8552047	-0.1714833	-0.1758	-0.2245333	-0.2015333	-0.2202	-0.1946667	-0.2709333	-0.2042
16.9754953	-0.1801042	-0.1820625	-0.2330625	-0.2089375	-0.2486667	-0.1969375	-0.30525	-0.2178125

Table 25: Unpainted model - 130 mph alpha sweep, beta = 0°.

Mach #	Reynolds #	q_c	Uinf	Alpha_c	C_L	C_D_c	L/D	Cl_cg_w	Cm_cg_c_w	Cn_cg_w/r
0.168675716	159843.731	40.53023678	130.7078594	-2.0725517	-0.09019784	0.013425625	-6.71833477	-0.00088315	0.175014739	-0.00107786
0.168748429	159912.6373	40.56518829	130.7642056	-0.05712618	0.037139779	0.009501922	3.908659648	-0.00072607	-0.08542089	-0.00050705
0.16881081	159971.7513	40.59518488	130.8125446	2.197084472	0.13685939	0.01247873	10.96741306	0.000349972	-0.27901125	0.000527294
0.169009145	160159.7017	40.69063123	130.9662358	4.267610116	0.224538391	0.01805348	12.43740194	0.000437276	-0.44645096	0.000617629
0.16919719	160337.9006	40.78122904	131.1119531	6.417076893	0.302198435	0.026462293	11.41996416	0.001507962	-0.59740238	0.001409161
0.169382251	160513.2714	40.8704874	131.2553578	8.551751598	0.361468656	0.04361449	8.28781122	0.002896515	-0.7239664	0.00274529
0.169480968	160606.82	40.91814066	131.3318546	10.46630002	0.255233413	0.044674597	5.713166559	0.001737375	-0.2541749	0.001422317
0.169415756	160545.0218	40.88665782	131.2813209	12.57667387	0.284292292	0.068342857	4.159795274	0.002356266	-0.28296859	0.001600111
0.169244263	160382.5086	40.80392391	131.1484301	14.72490535	0.360416578	0.103189339	3.492769512	0.003535715	-0.46497722	0.004414323
0.146060546	138412.7085	30.39064093	113.1832242	16.86295867	0.423887176	0.134661773	3.147791428	0.003301354	-0.70594604	0.005033495

alpha_c	RightForeOut	RightForeIn	RightAftOut	RightAftIn	LeftForeOut	LeftForeIn	LeftAftOut	LeftAftIn
-2.0725517	-0.30016471	-0.2937	-0.3713	-0.3353	-0.2893	-0.0073	-0.359	-0.3381
-0.05712618	-0.30809048	-0.30585714	-0.3925	-0.3485	-0.29942857	-0.008	-0.37771429	-0.35107143
2.197084472	-0.32146154	-0.31653846	-0.41730769	-0.36184615	-0.31515385	-0.00853846	-0.40153846	-0.36461538
4.267610116	-0.34042857	-0.33266667	-0.4398	-0.37266667	-0.32853333	-0.009	-0.42293333	-0.37526667
6.417076893	-0.35537619	-0.34464286	-0.45942857	-0.38242857	-0.34414286	-0.01	-0.44007143	-0.38542857
8.551751598	-0.37105952	-0.35414286	-0.47378571	-0.39278571	-0.35842857	-0.01	-0.45207143	-0.39428571
10.46630002	-0.39077619	-0.36273333	-0.4914	-0.40626667	-0.37733333	-0.01	-0.47126667	-0.40746667
12.57667387	-0.41037912	-0.3735	-0.51407143	-0.418	-0.39564286	-0.01	-0.49114286	-0.42128571
14.72490535	-0.4385	-0.39014286	-0.54707143	-0.43221429	-0.42292857	-0.01092857	-0.5165	-0.43392857
16.86295867	-0.31821894	-0.27344565	-0.397	-0.30117391	-0.30825	-0.00906522	-0.3703587	-0.30267391

Table 26: Unpainted model - 130 mph alpha sweep, beta = -2°.

Mach #	Reynolds #	q_c	Uinf	Alpha_c	C_L	C_D_c	L/D	Cl_cg_w	Cm_cg_c_w	Cn_cg_w/r
0.168518973	159695.195	40.45494571	130.5863981	-2.06872074	-0.0854351	0.009725963	-8.78423047	0.000335948	0.161674596	-0.00108317
0.168531433	159707.003	40.46092848	130.5960538	-0.05279172	0.042528466	0.005205508	8.169896836	0.002494001	-0.10004455	-0.00065878
0.1686782	159846.0848	40.53143047	130.7097842	2.154435584	0.143926415	0.007236154	19.8899061	0.005881545	-0.29990708	0.000816764
0.168861702	160019.9792	40.6196656	130.8519815	4.272075783	0.230090204	0.014098718	16.31993768	0.007654986	-0.45965091	0.001747429
0.169073755	160220.9284	40.72174804	131.0163023	6.419482722	0.305189414	0.023837007	12.80317683	0.011095202	-0.6056413	0.003218303
0.169223311	160362.6537	40.79382169	131.1321943	8.554310305	0.364649697	0.04036839	9.033050259	0.015421892	-0.72889101	0.005733005
0.169316555	160451.0152	40.83878977	131.2044496	10.46970513	0.25946672	0.040764795	6.364970547	0.010067258	-0.2640542	0.001882192
0.169301766	160437.0004	40.83165581	131.1929893	12.58116826	0.289879808	0.064296531	4.508482862	0.0120021	-0.29480508	0.000551796
0.16913738	160281.2221	40.75240232	131.0656059	14.73219705	0.369481786	0.097302523	3.797247731	0.014443658	-0.48699557	0.002234973
0.15984999	151480.1263	36.39982047	123.8687493	16.8544586	0.413319701	0.124294362	3.325329428	0.012110295	-0.64952606	0.003782736

alpha_c	RightForeOut	RightForeIn	RightAftOut	RightAftIn	LeftForeOut	LeftForeIn	LeftAftOut	LeftAftIn
-2.06872074	-0.30090756	-0.294	-0.36828571	-0.33428571	-0.28942857	-0.008	-0.36142857	-0.33785714
-0.05279172	-0.30601905	-0.30442857	-0.38614286	-0.34635714	-0.30242857	-0.00814286	-0.38071429	-0.35071429
2.154435584	-0.31607692	-0.31644444	-0.41077778	-0.36	-0.31744444	-0.009	-0.40888889	-0.365
4.272075783	-0.33542857	-0.32730769	-0.43476923	-0.37215385	-0.333	-0.01	-0.42892308	-0.37638462
6.419482722	-0.34633333	-0.33793333	-0.45466667	-0.38086667	-0.3466	-0.01	-0.44473333	-0.3884
8.554310305	-0.36241667	-0.34814286	-0.4695	-0.38828571	-0.36264286	-0.01	-0.45528571	-0.39542857
10.46970513	-0.38241209	-0.36046154	-0.49076923	-0.40230769	-0.38023077	-0.01	-0.47307692	-0.40876923
12.58116826	-0.40152198	-0.37178571	-0.50957143	-0.41592857	-0.4	-0.01	-0.49214286	-0.42214286
14.73219705	-0.42885714	-0.38735714	-0.54178571	-0.43107143	-0.42757143	-0.011	-0.52371429	-0.43492857
16.8544586	-0.37543947	-0.32940678	-0.47332203	-0.36477966	-0.37955932	-0.00969492	-0.45461017	-0.36611864

Table 27: Unpainted model - 130 mph alpha sweep, beta = -4°.

Mach #	Reynolds #	q_c	Uinf	Alpha_c	C_L	C_D_c	L/D	Cl_cg_w	Cm_cg_c_w	Cn_cg_w/r
0.16831536	159502.2434	40.35724544	130.4286172	-2.063176321	-0.078542164	0.007730117	-10.16053969	0.001329713	0.136731349	-0.001818801
0.168452517	159632.2189	40.42304506	130.5349012	-0.046829767	0.0499405	0.003152008	15.84402634	0.005800291	-0.119521526	-0.001164729
0.168581321	159754.2788	40.48488616	130.6347123	2.122949098	0.15285297	0.004997252	30.58740715	0.011287517	-0.319202942	0.000450961
0.168716778	159882.6429	40.54997233	130.7396786	4.278913219	0.238590653	0.011108811	21.47760391	0.01487431	-0.47448416	0.001832729
0.168919951	160075.1774	40.64769361	130.8971184	6.423064379	0.309642207	0.019866609	15.58606275	0.020444929	-0.606061588	0.003515994
0.169108106	160253.4806	40.73829666	131.042921	8.554778253	0.36523146	0.03364739	10.8546744	0.026547019	-0.713480996	0.00514564
0.16917753	160319.2702	40.77175247	131.0967186	10.49791095	0.294532797	0.042240357	6.972781952	0.020492145	-0.376946584	0.003079941
0.169107418	160252.8291	40.73796541	131.0423882	12.58997174	0.300824488	0.063009285	4.774288229	0.021509782	-0.324105149	-0.000582982
0.168945858	160099.7286	40.6601631	130.9171945	14.74121224	0.380689658	0.094399838	4.032736364	0.024929063	-0.515370473	-0.00055666
0.168819131	159979.6368	40.59918708	130.8189927	16.919443	0.494109703	0.135959647	3.634237904	0.026062261	-0.820848364	0.003196729
0.16204517	153560.3655	37.40642457	125.5698083	19.08668084	0.48570285	0.156830467	3.09699295	0.02125739	-0.808360502	0.002105065

alpha_c	RightForeOut	RightForeIn	RightAftOut	RightAftIn	LeftForeOut	LeftForeIn	LeftAftOut	LeftAftIn
-2.063176321	-0.30005042	-0.294857143	-0.365857143	-0.334571429	-0.293428571	-0.008	-0.364	-0.34
-0.046829767	-0.307804762	-0.305642857	-0.384357143	-0.346357143	-0.304428571	-0.008285714	-0.3885	-0.352
2.122949098	-0.316951923	-0.316625	-0.405	-0.35875	-0.321375	-0.009	-0.412125	-0.36675
4.278913219	-0.334351648	-0.326923077	-0.429923077	-0.368923077	-0.336538462	-0.01	-0.434230769	-0.379230769
6.423064379	-0.344964103	-0.336846154	-0.450615385	-0.379538462	-0.353615385	-0.01	-0.451230769	-0.389384615
8.554778253	-0.360333333	-0.346583333	-0.465083333	-0.465083333	-0.38825	-0.01	-0.46	-0.39725
10.49791095	-0.374214286	-0.358357143	-0.485142857	-0.399428571	-0.381714286	-0.01	-0.474285714	-0.409714286
12.58997174	-0.396461538	-0.369230769	-0.505846154	-0.413	-0.402	-0.010230769	-0.495307692	-0.422461538
14.74121224	-0.422071429	-0.385071429	-0.533571429	-0.429285714	-0.434285714	-0.011	-0.526571429	-0.434428571
16.919443	-0.453428571	-0.403428571	-0.570571429	-0.447714286	-0.478214286	-0.011	-0.5715	-0.450142857
19.08668084	-0.41709478	-0.357839286	-0.519160714	-0.394785714	-0.448875	-0.010125	-0.527857143	-0.393

Table 28: Unpainted model - 130 mph alpha sweep, beta = -6°.

Mach #	Reynolds #	q_c	Uinf	Alpha_c	C_L	C_D_c	L/D	Cl_cg_w	Cm_cg_c_w	Cn_cg_w/r
0.168104824	159302.7317	40.25634775	130.265472	-0.04632947	0.050562476	0.006530516	7.742493516	0.008733689	-0.12054455	-0.00265236
0.16816565	159360.3723	40.28548497	130.312606	2.122492698	0.152285563	0.007258664	20.97983498	0.015959093	-0.31776366	-0.00133776
0.168349993	159535.0636	40.37385548	130.455455	4.276468157	0.235550898	0.012620467	18.66419783	0.020726995	-0.46633967	-0.00022041
0.168582382	159755.2846	40.48539598	130.6355348	6.420789282	0.306813757	0.019869854	15.44116852	0.028348442	-0.59773128	0.00175217
0.168786809	159949.0075	40.58364255	130.7939464	8.551755532	0.361473547	0.034320721	10.53222483	0.03551662	-0.70275306	0.002449956
0.168850722	160009.5738	40.61438313	130.8434728	10.51734558	0.318694347	0.048201312	6.611735869	0.030110248	-0.46466228	0.002704747
0.168691481	159858.6703	40.53781321	130.7200756	12.594828	0.306861898	0.06710904	4.572586607	0.029167286	-0.34192086	-0.00220865
0.16847633	159654.7853	40.43447468	130.5533542	14.74320999	0.3831733	0.095587957	4.008593878	0.033189937	-0.52040209	-0.00428812
0.162608594	154094.2884	37.66699789	126.0064092	16.86140322	0.421953403	0.121135178	3.483326721	0.028628601	-0.66190833	-0.00336387

alpha_c	RightForeOut	RightForeIn	RightAftOut	RightAftIn	LeftForeOut	LeftForeIn	LeftAftOut	LeftAftIn
-0.04632947	-0.30993137	-0.30483333	-0.37941667	-0.34516667	-0.30633333	-0.008	-0.3925	-0.353
2.122492698	-0.31530476	-0.31571429	-0.398	-0.35657143	-0.32142857	-0.009	-0.41585714	-0.36614286
4.276468157	-0.32892308	-0.325	-0.41815385	-0.36669231	-0.34030769	-0.00946154	-0.43669231	-0.38076923
6.420789282	-0.34035714	-0.33364286	-0.43971429	-0.37578571	-0.35285714	-0.01	-0.45057143	-0.38935714
8.551755532	-0.35473333	-0.34463636	-0.45572727	-0.38636364	-0.37036364	-0.01	-0.45990909	-0.39863636
10.51734558	-0.36981667	-0.35466667	-0.47766667	-0.39646667	-0.385	-0.01	-0.47386667	-0.40946667
12.594828	-0.38985714	-0.36735714	-0.497	-0.41042857	-0.40728571	-0.01085714	-0.49571429	-0.42128571
14.74320999	-0.41330769	-0.38366667	-0.5235	-0.42633333	-0.44055556	-0.011	-0.53066667	-0.43266667
16.86140322	-0.37902116	-0.34272222	-0.47822222	-0.38105556	-0.4142037	-0.01005556	-0.49812963	-0.3837963

Table 29: Unpainted model - 130 mph alpha sweep, beta = -8°.

Mach #	Reynolds #	q_c	Uinf	Alpha_c	C_L	C_D_c	L/D	Cl_cg_w	Cm_cg_c_w	Cn_cg_w/r
0.167674062	158894.5245	40.05030132	129.9316716	-2.0617188	-0.07673014	0.010911771	-7.03186845	0.002953721	0.136012601	-0.00463667
0.167858661	159069.4579	40.13853589	130.0747187	-0.04808887	0.048375161	0.005613881	8.617061723	0.011566117	-0.10979325	-0.00339897
0.167987881	159191.9114	40.20035786	130.1748516	2.120275457	0.149529042	0.006826364	21.90463858	0.020561884	-0.30245519	-0.00237939
0.168210635	159403.0023	40.30704111	130.3474655	4.275251528	0.234038359	0.010904757	21.46204299	0.026878304	-0.45353334	-0.00138697
0.168402973	159585.2695	40.3992709	130.4965095	6.418239568	0.303643898	0.017249039	17.60352593	0.036202867	-0.57767714	-5.2313E-05
0.168610718	159782.1369	40.49900701	130.6574925	8.548790567	0.357787439	0.033029761	10.8322744	0.044623459	-0.67747434	0.000683138
0.168595471	159767.6874	40.49168248	130.6456768	10.52876906	0.33289627	0.047311883	7.0362084	0.039989325	-0.50312783	0.0023215
0.168385769	159568.9659	40.39101677	130.4831777	12.59826317	0.311132571	0.066362836	4.688355584	0.036777068	-0.34948045	-0.00257712
0.168150974	159346.4651	40.27845393	130.3012338	14.73905386	0.378006314	0.092794389	4.073590229	0.040119173	-0.49767087	-0.0058168
0.161993463	153511.3659	37.38255637	125.5297403	16.85829248	0.418086069	0.119847928	3.488471391	0.035661381	-0.64909491	-0.00633496
	alpha_c	RightForeOut	RightForeIn	RightAftOut	RightAftIn	LeftForeOut	LeftForeIn	LeftAftOut	LeftAftIn	
	-2.0617188	-0.30147899	-0.29457143	-0.36185714	-0.33314286	-0.29442857	-0.00757143	-0.37114286	-0.34042857	
	-0.04808887	-0.30609048	-0.30378571	-0.37564286	-0.34342857	-0.30757143	-0.008	-0.39492857	-0.35257143	
	2.120275457	-0.31318803	-0.314	-0.39322222	-0.35566667	-0.32588889	-0.009	-0.42077778	-0.36977778	
	4.275251528	-0.32004396	-0.32476923	-0.40761538	-0.36669231	-0.34415385	-0.009	-0.43969231	-0.38292308	
	6.418239568	-0.3359641	-0.33261538	-0.42992308	-0.37438462	-0.35769231	-0.00992308	-0.45430769	-0.39169231	
	8.548790567	-0.34758333	-0.34116667	-0.44783333	-0.38375	-0.37408333	-0.01	-0.46116667	-0.39833333	
	10.52876906	-0.36084286	-0.35113333	-0.46933333	-0.39473333	-0.38846667	-0.01	-0.47433333	-0.41006667	
	12.59826317	-0.38139103	-0.36416667	-0.487	-0.40875	-0.41191667	-0.01	-0.49791667	-0.42075	
	14.73905386	-0.40192857	-0.37835714	-0.50742857	-0.42142857	-0.447	-0.01	-0.53642857	-0.43042857	
	16.85829248	-0.36520889	-0.33650943	-0.46083019	-0.37550943	-0.41973585	-0.00960377	-0.50620755	-0.37807547	

Table 30: Unpainted model - 130 mph alpha sweep, beta = -10°.

Mach #	Reynolds #	q_c	Uinf	Alpha_c	C_L	C_D_c	L/D	Cl_cg_w	Cm_cg_c_w	Cn_cg_w/r
0.168892037	160048.7252	40.63426079	130.8754879	-0.0446537	0.052645833	0.005396636	9.755306292	0.015066542	-0.1184251	-0.0043183
0.169172177	160314.1971	40.76917218	131.0925702	2.121673191	0.151266735	0.006589078	22.95719352	0.025601623	-0.30256187	-0.00327507
0.169401939	160531.9287	40.87998914	131.2706143	4.278060324	0.237530315	0.0108163	21.96040287	0.0333116	-0.45541208	-0.00274853
0.169595888	160715.7219	40.97364982	131.4209062	6.419009754	0.30460141	0.018310249	16.63556924	0.043743702	-0.57050991	-0.00223164
0.169755818	160867.2784	41.05096338	131.5448374	8.553469453	0.363604331	0.03436043	10.58212121	0.053715594	-0.6810559	-0.00065409
0.169759237	160870.5183	41.05261695	131.5474868	10.52660005	0.330199707	0.046550426	7.093376638	0.047764738	-0.47879932	0.001155462
0.16954441	160666.9395	40.94877996	131.3810157	12.60564365	0.32030814	0.066606002	4.808998162	0.04450598	-0.37004367	-0.00262974
0.169140734	160284.4001	40.75401836	131.0682045	14.74239653	0.382161993	0.094064359	4.062771441	0.046483373	-0.50955931	-0.00644156
0.164426834	155817.3235	38.51406909	127.4153743	16.88032065	0.44547196	0.120373333	3.700752882	0.046463108	-0.70503643	-0.0068598
	alpha_c	RightForeOut	RightForeIn	RightAftOut	RightAftIn	LeftForeOut	LeftForeIn	LeftAftOut	LeftAftIn	
	-0.0446537	-0.31158824	-0.30935294	-0.37782353	-0.34788235	-0.31417647	-0.00794118	-0.40623529	-0.35929412	
	2.121673191	-0.31935833	-0.319625	-0.39475	-0.359875	-0.334875	-0.008625	-0.43075	-0.379	
	4.278060324	-0.32576923	-0.32861538	-0.40976923	-0.37038462	-0.35161538	-0.009	-0.45046154	-0.38692308	
	6.419009754	-0.3367619	-0.3366	-0.4234	-0.37833333	-0.3672	-0.009	-0.46013333	-0.39673333	
	8.553469453	-0.3484	-0.34566667	-0.449	-0.38866667	-0.38333333	-0.00966667	-0.46716667	-0.40466667	
	10.52660005	-0.36347917	-0.3575	-0.4679375	-0.398625	-0.3991875	-0.01	-0.480625	-0.4170625	
	12.60564365	-0.37914286	-0.3655625	-0.479875	-0.4093125	-0.4189375	-0.01	-0.503	-0.4260625	
	14.74239653	-0.39886325	-0.37883333	-0.50294444	-0.42438889	-0.45383333	-0.01	-0.55303889	-0.43405556	
	16.88032065	-0.38272527	-0.356	-0.48003297	-0.39695604	-0.45667033	-0.00946154	-0.55791209	-0.40014286	

Table 31: Unpainted model - 130 mph alpha sweep, beta = -12°.

Mach #	Reynolds #	q_c	Uinf	Alpha_c	C_L	C_D_c	L/D	Cl_cg_w	Cm_cg_c_w	Cn_cg_w/r
0.168781657	159944.1253	40.58116506	130.7899541	-2.05436703	-0.06759026	0.012229766	-5.5267012	0.005183767	0.117277006	-0.00645456
0.168751891	159915.9173	40.56685239	130.7668878	-0.04392131	0.053556352	0.006402612	8.364765707	0.018263788	-0.11579234	-0.00523852
0.168927306	160082.1478	40.65123367	130.9028183	2.120837857	0.15022823	0.006382231	23.53851368	0.030524069	-0.29414416	-0.00372147
0.169109207	160254.5246	40.73882745	131.0437747	4.27662672	0.235748027	0.012730271	18.51869605	0.038920677	-0.44448946	-0.00475996
0.169304282	160439.3853	40.83286976	131.1949395	6.417474631	0.302692911	0.020082165	15.07272314	0.050612656	-0.55403443	-0.00363486
0.169481161	160607.0021	40.91823345	131.3320035	8.552646465	0.362581174	0.033723193	10.7516859	0.061092087	-0.65819493	-0.00140163
0.169536253	160659.2096	40.94483986	131.3746949	10.52957745	0.333901278	0.046921717	7.116135104	0.055220006	-0.47547852	0.001446152
0.169340276	160473.4946	40.85023368	131.2228314	12.61182721	0.327995682	0.066775096	4.91194622	0.050949246	-0.38336283	-0.00224458
0.168960067	160113.1934	40.6670026	130.9282049	14.74351743	0.383555526	0.092637374	4.140397225	0.052430291	-0.50565537	-0.00614292
0.162915858	154385.4638	37.80948293	126.24451	16.85639682	0.415729333	0.117370554	3.542024133	0.050721111	-0.63510141	-0.0074078
	alpha_c	RightForeOut	RightForeIn	RightAftOut	RightAftIn	LeftForeOut	LeftForeIn	LeftAftOut	LeftAftIn	
	-2.05436703	-0.30747899	-0.30157143	-0.36228571	-0.33871429	-0.30242857	-0.00771429	-0.38457143	-0.34685714	
	-0.04392131	-0.31117083	-0.310625	-0.3775	-0.3484375	-0.3184375	-0.008	-0.41025	-0.3658125	
	2.120837857	-0.31707692	-0.31816667	-0.3855	-0.35883333	-0.3375	-0.009	-0.43283333	-0.37766667	
	4.27662672	-0.32158242	-0.32723077	-0.40376923	-0.36853846	-0.35661538	-0.009	-0.45107692	-0.38930769	
	6.417474631	-0.32933333	-0.3352	-0.41626667	-0.3766	-0.36986667	-0.009	-0.46066667	-0.3964	
	8.552646465	-0.34433974	-0.34353846	-0.43392308	-0.38738462	-0.38476923	-0.01	-0.464	-0.406	
	10.52957745	-0.3535	-0.3535	-0.4513125	-0.3954375	-0.3975625	-0.01	-0.476125	-0.413625	
	12.61182721	-0.37442534	-0.36352941	-0.46964706	-0.40782353	-0.42111765	-0.01	-0.50129412	-0.42264706	
	14.74351743	-0.39236975	-0.37635294	-0.49158824	-0.42152941	-0.45623529	-0.01005882	-0.565	-0.43041176	
	16.85639682	-0.35699373	-0.33770175	-0.44808772	-0.37868421	-0.44331579	-0.00910526	-0.54373684	-0.38082456	

Table 32: Unpainted model - 130 mph alpha sweep, beta = -14°.

Mach #	Reynolds #	q_c	Uinf	Alpha_c	C_L	C_D_c	L/D	Cl_cg_w	Cm_cg_c_w	Cn_cg_w/r
0.168640439	159810.3012	40.51328553	130.6805231	-2.0568894	-0.07072613	0.013639983	-5.18520678	0.005640642	0.131100628	-0.00753922
0.168471506	159650.2138	40.43215909	130.5496159	-0.04847736	0.047892172	0.006709597	7.137860703	0.020889974	-0.09327809	-0.00607078
0.168602018	159773.8917	40.49482739	130.6507502	2.083044863	0.139296589	0.007162995	19.44669738	0.033604073	-0.25387425	-0.00595974
0.168735092	159899.9983	40.55877628	130.7538705	4.268484245	0.225625126	0.012552791	17.97410116	0.043038049	-0.40358311	-0.00607427
0.168859164	160017.574	40.61844458	130.8500148	6.409154497	0.292349141	0.021213819	13.78107048	0.055676251	-0.50788239	-0.00559785
0.169105394	160250.9109	40.73699019	131.0408197	8.547684516	0.356412373	0.033997092	10.4836135	0.065097923	-0.61773429	-0.00075283
0.169121308	160265.9912	40.74465762	131.0531512	10.52751322	0.331334986	0.045063089	7.352691373	0.060381605	-0.45014542	0.001999353
0.168948997	160102.7025	40.66167364	130.9196263	12.69898372	0.328190253	0.065128209	5.039141378	0.055632529	-0.37262578	-0.00202748
0.168689542	159856.8335	40.53688164	130.7185736	14.73305187	0.370544512	0.091477932	4.050643751	0.056233424	-0.45779142	-0.00580492
0.161773263	153302.6961	37.28099634	125.3591062	16.84528194	0.401911083	0.116992371	3.435361469	0.057627968	-0.59373225	-0.0074594
	alpha_c	RightForeOut	RightForeIn	RightAftOut	RightAftIn	LeftForeOut	LeftForeIn	LeftAftOut	LeftAftIn	
	-2.0568894	-0.30918576	-0.30268421	-0.36163158	-0.338	-0.30442105	-0.008	-0.38926316	-0.34963158	
	-0.04847736	-0.31133333	-0.30913333	-0.37306667	-0.3466	-0.3208	-0.008	-0.41153333	-0.36433333	
	2.083044863	-0.31407692	-0.3168	-0.38506667	-0.35573333	-0.34093333	-0.00853333	-0.43406667	-0.37606667	
	4.268484245	-0.3205119	-0.3245	-0.39675	-0.36441667	-0.35791667	-0.009	-0.45008333	-0.38783333	
	6.409154497	-0.3264	-0.333	-0.40893333	-0.37266667	-0.37266667	-0.009	-0.45546667	-0.3964	
	8.547684516	-0.33787121	-0.342	-0.42863636	-0.38490909	-0.385	-0.009	-0.45881818	-0.40627273	
	10.52751322	-0.34937619	-0.3494	-0.445	-0.39413333	-0.39846667	-0.009	-0.47066667	-0.41533333	
	12.69898372	-0.36609341	-0.36142857	-0.46257143	-0.407	-0.42385714	-0.00928571	-0.51185714	-0.4205	
	14.73305187	-0.38331092	-0.37264706	-0.48241176	-0.41841176	-0.46441176	-0.00952941	-0.57258824	-0.42576471	
	16.84528194	-0.34130952	-0.32940351	-0.4275614	-0.3695614	-0.44112281	-0.00857895	-0.53824561	-0.38157895	

Table 33: Unpainted model - 130 mph alpha sweep, beta = -16°.

Mach #	Reynolds #	q_c	Uinf	Alpha_c	C_L	C_D_c	L/D	Cl_cg_w	Cm_cg_c_w	Cn_cg_w/r
0.168390803	159573.7365	40.39343192	130.4870787	-2.04830201	-0.0600501	0.015275955	-3.93102111	0.007931349	0.10629597	-0.00904657
0.1682951	159483.0444	40.34753059	130.4129178	-0.04251181	0.055308683	0.00773809	7.147588735	0.024840698	-0.10740356	-0.00806733
0.168407155	159589.2319	40.40127714	130.4997497	2.088918364	0.146598652	0.00999356	14.66931169	0.038370587	-0.26911735	-0.00801922
0.168560793	159734.8254	40.47502701	130.6188048	4.272212615	0.230260317	0.016353406	14.08026628	0.048561061	-0.4091563	-0.00745817
0.168652149	159821.3985	40.51891227	130.6895977	6.413520186	0.297776661	0.017974834	16.5663094	0.062588973	-0.50516558	-0.005182
0.168777124	159939.8297	40.57898533	130.7864415	8.554540143	0.364935435	0.032080533	11.37560393	0.071552384	-0.62408527	0.000752182
0.168734166	159899.1208	40.55833108	130.7531529	10.53566545	0.341470011	0.044530019	7.668310419	0.065829295	-0.46671436	0.001490171
0.168538909	159714.0878	40.46451836	130.6018472	12.62174306	0.340323271	0.064958909	5.239054617	0.061160671	-0.40341673	-0.00143651
0.168295423	159483.3505	40.34768549	130.4131681	14.73842046	0.377218857	0.091334376	4.130086318	0.062886496	-0.47268751	-0.00430507
0.159925561	151551.741	36.43424582	123.9273103	16.84841047	0.40580054	0.114564628	3.542110219	0.065972587	-0.60797337	-0.00635503

alpha_c	RightForeOut	RightForeIn	RightAftOut	RightAftIn	LeftForeOut	LeftForeIn	LeftAftOut	LeftAftIn
-2.04830201	-0.30920221	-0.3021875	-0.362375	-0.3383125	-0.3086875	-0.008	-0.39375	-0.353625
-0.04251181	-0.31292083	-0.309	-0.370875	-0.346	-0.32475	-0.008	-0.41625	-0.3643125
2.088918364	-0.31367692	-0.31666667	-0.38113333	-0.35393333	-0.344	-0.008	-0.43473333	-0.37493333
4.272212615	-0.31933766	-0.32236364	-0.38709091	-0.36245455	-0.36109091	-0.009	-0.44745455	-0.38681818
6.413520186	-0.32329583	-0.331625	-0.4044375	-0.370875	-0.373625	-0.009	-0.452375	-0.39875
8.554540143	-0.33530556	-0.34288889	-0.41944444	-0.38122222	-0.38477778	-0.009	-0.45244444	-0.40555556
10.53566545	-0.34450952	-0.34753333	-0.43606667	-0.3908	-0.3968	-0.009	-0.46853333	-0.41133333
12.62174306	-0.35745055	-0.35792857	-0.45378571	-0.40135714	-0.422	-0.009	-0.51221429	-0.41385714
14.73842046	-0.37599107	-0.3684375	-0.4700625	-0.4148125	-0.4673125	-0.009	-0.5739375	-0.424875
16.84841047	-0.32476566	-0.31650877	-0.40647368	-0.35722807	-0.43359649	-0.00798246	-0.52314035	-0.39178947

Table 34: Painted model - 110 mph beta sweep, alpha = 8°.

Mach #	Reynolds #	q_c	Uinf	Alpha_c	Beta	C_L	C_D_c	L/D	Cl_cg_w	Cm_cg_c_w	Cn_cg_w/r
0.14314567	135650.4571	29.18975487	110.9244683	8.407063593	12.102	0.289749685	0.052259083	5.544484684	0.068807655	-0.43964006	0.095954658
0.143273935	135772.0058	29.24208888	111.0238615	8.405510998	8.153	0.287819465	0.043597242	6.601781535	0.093741206	-0.44553131	0.073782878
0.143347942	135842.138	29.27230633	111.0812102	8.40296095	4.161	0.284649191	0.037477662	7.595169312	0.127895762	-0.44583317	0.043600617
0.143344811	135839.1712	29.2710277	111.0787841	8.399354972	0.17	0.280166161	0.033286915	8.41670561	0.159563882	-0.43667538	0.009806992
0.143079763	135588.0013	29.16288212	110.8733968	8.40040619	-3.864	0.281473058	0.03279014	8.584076241	0.185993063	-0.4378771	-0.04927665
0.142825987	135347.5131	29.05952328	110.6767441	8.403758292	-7.771	0.285640463	0.038497012	7.419808592	0.21742995	-0.43885127	-0.11458941
0.142581002	135115.3554	28.95991884	110.4869034	8.407117986	-11.762	0.289817307	0.048140264	6.020268274	0.238352518	-0.43078761	-0.16091531

alpha_c	Beta	RightForeOut	RightForeIn	RightAftOut	RightAftIn	LeftForeOut	LeftForeIn	LeftAftOut	LeftAftIn
8.407063593	12.102	-0.28404413	-0.25350202	-0.33618219	-0.28799175	-0.24130117	-0.24556299	-0.30215385	-0.27737247
8.405510998	8.153	-0.2786474	-0.24931214	-0.33591329	-0.28568786	-0.2467052	-0.24620809	-0.31246821	-0.27884393
8.40296095	4.161	-0.27138827	-0.24710734	-0.33261017	-0.28306741	-0.25136996	-0.2470678	-0.32049153	-0.28057627
8.399354972	0.17	-0.26304707	-0.24383237	-0.32787283	-0.28213873	-0.25687036	-0.25458375	-0.32602312	-0.28531792
8.40040619	-3.864	-0.25726183	-0.23822093	-0.32097093	-0.27696512	-0.26203615	-0.2577516	-0.33027326	-0.28731977
8.403758292	-7.771	-0.25354016	-0.23653714	-0.31370857	-0.27508	-0.26696	-0.25713734	-0.33244	-0.28519429
8.407117986	-11.762	-0.24897143	-0.23514857	-0.30465143	-0.27425143	-0.27229143	-0.26208571	-0.33153143	-0.28736

Table 35: Paint removed from wing body junction - 110 mph alpha sweep, beta = 0°.

Mach #	Reynolds #	q_c	Uinf	Alpha_c	C_L	C_D_c	Cl_cg_w	Cm_cg_c_w	Cn_cg_w/r
0.14125657	133487.001	28.4503804	109.867001	0.03053027	0.0379559	0.00905022	-0.001862	-0.0754311	-0.0034558
0.14136306	133587.636	28.4932937	109.949829	2.18557283	0.12254787	0.00599041	0.00336583	-0.2220893	0.00789291
0.14143957	133659.938	28.5241452	110.009338	4.25228907	0.20549093	0.00958369	0.00051024	-0.372576	0.00198012
0.14162658	133836.666	28.5996253	110.154794	6.39040523	0.26903965	0.01709142	-0.0031075	-0.4666487	-0.0063589
0.14168906	133895.703	28.6248623	110.203385	7.45264889	0.29296378	0.02043349	-0.0037858	-0.5014899	-0.0080894
0.14175286	133955.996	28.6506476	110.25301	8.42517468	0.31226578	0.0268267	-0.0033647	-0.5302043	-0.0073297
0.14174878	133952.143	28.6489996	110.249839	9.48462103	0.33271224	0.03519678	-0.0016579	-0.5664331	-0.0037198
0.14169641	133902.652	28.6278337	110.209105	10.5574083	0.36850113	0.05225257	0.00062953	-0.6421499	0.00165634
0.14166609	133873.996	28.6155819	110.185519	11.6195229	0.39226492	0.06995308	0.00437656	-0.6852385	0.01137448
0.14162404	133834.261	28.5985978	110.152816	12.6667771	0.39631055	0.08228687	0.00924904	-0.6670999	0.02276403
0.14150051	133717.528	28.5487309	110.056738	13.7032351	0.38817742	0.0907301	0.01400421	-0.6034958	0.03550262
0.14147614	133694.494	28.5388961	110.037779	14.7286996	0.36513362	0.0991721	0.01845622	-0.4823069	0.0475307
0.14139374	133616.631	28.5056642	109.973694	15.7868566	0.38397718	0.11306492	0.02253748	-0.4991772	0.05763624
0.14134296	133568.643	28.4851923	109.934197	16.8512654	0.40934984	0.12831794	0.02444078	-0.5336329	0.0638064
0.14131414	133541.405	28.4735756	109.911779	17.919199	0.44034785	0.14543809	0.02409869	-0.5884681	0.06360076
0.14126495	133494.929	28.4537598	109.873526	18.9933761	0.47786472	0.16489999	0.02040391	-0.6710463	0.05479802
0.1411904	133424.476	28.4237345	109.81554	20.0724595	0.52272435	0.18642345	0.0125095	-0.7866693	0.03369307
0.14112245	133360.266	28.3963836	109.762692	21.2405659	0.56885585	0.21252404	-0.0025541	-0.9201346	-0.0062812

Table 36: Paint removed from entire wing - 110 mph alpha sweep, beta = 0°.

| Mach #	Reynolds #	q_c	Uinf	Alpha_c	C_L	C_D_c	Cl_cg_w	Cm_cg_c_w	Cn_cg_w/r
0.14169152	133605.878	28.5264625	110.062791	0.03434625	0.04269999	0.00838414	-0.0019064	-0.090324	-0.0034959
0.14169912	133613.045	28.5295232	110.068696	2.19040296	0.12855279	0.00367119	0.00333004	-0.2394759	0.00770227
0.14189307	133795.931	28.6076771	110.219354	4.25520903	0.2091211	0.00846522	0.00051229	-0.3828649	0.00181983
0.14198188	133879.674	28.6434995	110.28834	6.3953336	0.27516671	0.01369588	-0.0030195	-0.4826849	-0.0063318
0.14208895	133980.626	28.6867131	110.371503	8.43207711	0.32084702	0.02372208	-0.0033485	-0.5548022	-0.0074973
0.14214786	134036.181	28.7105079	110.417269	9.49002052	0.339425	0.03423631	-0.0016246	-0.5866152	-0.0038061
0.14220482	134089.884	28.7335189	110.461509	10.5611208	0.37311661	0.05259311	0.00073401	-0.6562187	0.00208086
0.14214135	134030.04	28.7078772	110.41221	11.6238411	0.3976333	0.07002865	0.00433237	-0.7029085	0.01105746
0.14201246	133908.501	28.6558362	110.312088	12.6708186	0.40133499	0.08477127	0.00925693	-0.6865083	0.02265939
0.14191848	133819.883	28.6179211	110.239086	13.7087796	0.39507042	0.09401687	0.01412697	-0.6278659	0.03536544
0.14191343	133815.123	28.615885	110.235164	14.729929	0.36666209	0.10088434	0.0185055	-0.4835579	0.04711622
0.14187739	133781.142	28.6013533	110.207171	15.7889721	0.38660722	0.11486537	0.0223972	-0.5029274	0.05716632
0.14184681	133752.307	28.5890253	110.183417	16.8539867	0.41273307	0.13031612	0.02430691	-0.538836	0.06334294
0.14177041	133680.264	28.558236	110.124069	18.9974909	0.48298023	0.16709414	0.02027243	-0.6842254	0.0545429
0.14166918	133584.814	28.5174683	110.045439	21.2461484	0.57579603	0.21346378	-0.00284	-0.9412665	-0.0067862
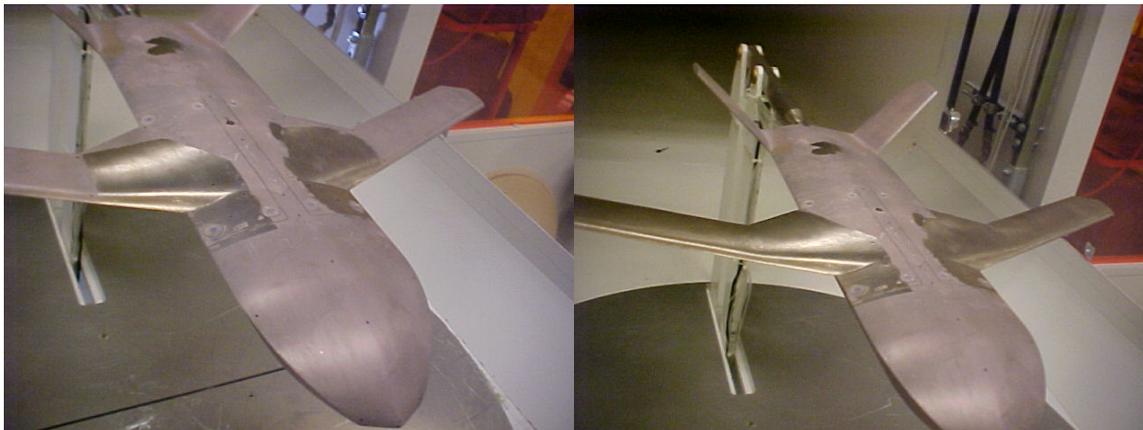
Figure 84: Strike Tanker w/paint removed from wing body junction and entire wing.

135

Table 37: Paint removed except tail section - 110 mph alpha sweep, beta = 0°.

Mach #	Reynolds #	q_c	Uinf	Alpha_c	C_L	C_D_c	Cl_cg_w	Cm_cg_c_w	Cn_cg_w/r
0.14139532	133326.578	28.4073192	109.832707	0.03362296	0.04180079	0.00847127	-0.001842	-0.0872066	-0.0034178
0.14151186	133436.474	28.4541688	109.923238	2.18964782	0.12761399	0.00464082	0.00334256	-0.2367136	0.00782996
0.14166433	133580.243	28.5155168	110.041674	4.25656322	0.21080465	0.00732565	0.00054435	-0.3860367	0.00195188
0.14182053	133727.524	28.5784317	110.163001	6.39467156	0.27434364	0.01489112	-0.0030645	-0.4813888	-0.006359
0.14193412	133834.635	28.6242309	110.251238	8.42999679	0.31826073	0.02480802	-0.003328	-0.5470922	-0.0074018
0.14203032	133925.348	28.6630468	110.325966	9.48981232	0.33916615	0.03248768	-0.0016205	-0.5836093	-0.0037548
0.14208235	133974.409	28.6840512	110.366382	10.5585566	0.36992884	0.05078185	0.00077154	-0.6448942	0.00196256
0.14198252	133880.274	28.6437565	110.288835	11.6217186	0.39499458	0.06964926	0.00429722	-0.6928611	0.01104054
0.14187876	133782.432	28.601905	110.208234	12.6678008	0.39758323	0.08366659	0.009267	-0.6732861	0.02255192
0.14184694	133752.428	28.589077	110.183517	13.7144912	0.40217128	0.0948812	0.01399476	-0.6512471	0.0348299
0.14173502	133646.894	28.54398	110.09658	14.7310042	0.36799875	0.10094615	0.01853273	-0.4835211	0.04728701
0.14166826	133583.944	28.5170968	110.044722	15.7896071	0.3873967	0.11464881	0.02209708	-0.5022841	0.05692643
0.14166979	133585.39	28.5177141	110.045913	16.8544298	0.41328384	0.12994607	0.0244747	-0.5373339	0.06360197
0.14166565	133581.487	28.5160479	110.042698	18.9978043	0.48336984	0.16645094	0.02054758	-0.684327	0.05447152
0.14150459	133429.611	28.4512419	109.917585	21.2459346	0.57553023	0.21005083	-0.0027009	-0.9366713	-0.0071351

Table 38: Paint removed from entire model - 110 mph alpha sweep, beta = 0°.

| Mach #	Reynolds #	q_c	Uinf	Alpha_c	C_L	C_D_c	Cl_cg_w	Cm_cg_c_w	Cn_cg_w/r
0.14127437	132903.926	28.3192157	109.840267	0.03111219	0.03867935	0.00936228	-0.000306	-0.0772898	-0.000123
0.1412813	132910.448	28.3219953	109.845658	2.18136303	0.11731415	0.00933829	-0.000151	-0.207859	0.00011488
0.14139387	133016.353	28.3671481	109.933184	4.24740418	0.19941793	0.01056734	-0.0002702	-0.353003	0.00017591
0.14149357	133110.14	28.4071643	110.010696	6.39157806	0.27049773	0.01584484	-0.0001303	-0.4684469	0.00036694
0.1416243	133233.13	28.4596832	110.112342	8.42846282	0.31635367	0.02329445	-4.051E-05	-0.538935	0.00035463
0.14176235	133362.994	28.5151902	110.21967	9.48707683	0.33576534	0.03269157	0.00014121	-0.572146	0.00059182
0.14170427	133308.359	28.4918315	110.174517	10.5599078	0.37160861	0.05045361	-0.0003421	-0.6472861	-0.0005161
0.14168552	133290.724	28.4842936	110.159942	11.6309952	0.4065275	0.06796637	-0.0004683	-0.729162	-0.0003413
0.14161939	133228.508	28.4577087	110.108523	12.6934532	0.42947488	0.08623655	-2.236E-05	-0.7817647	0.0006613
0.14156483	133177.178	28.4357848	110.0661	13.7271048	0.41785274	0.09619424	-0.0001763	-0.7051439	0.00113843
0.14152838	133142.887	28.421143	110.03776	14.7304351	0.36729131	0.10166271	-0.0004566	-0.4869557	0.00121613
0.14150592	133121.761	28.4121246	110.0203	15.7845055	0.38105421	0.11502136	-0.0003315	-0.4859439	0.00115137
0.14151518	133130.472	28.4158429	110.027499	16.8479009	0.40516707	0.13005285	-0.0005669	-0.5182001	0.0011323
0.14133558	132961.51	28.343761	109.887858	18.9900759	0.47376178	0.16530349	6.8327E-05	-0.6567569	0.00189015
0.14118194	132816.974	28.2821726	109.768405	21.2397786	0.56787699	0.20878706	0.00133144	-0.9094488	0.00371931
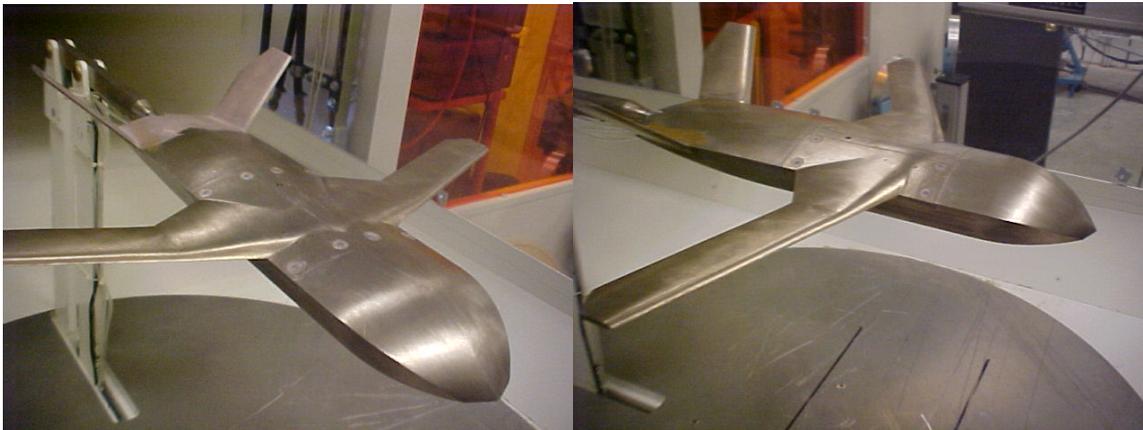
Figure 85: Strike Tanker w/paint removed from all but tail sections and entire body.

Bibliography

1. Amer, T.R., Obara C.J., Liu, T., "Quantifying the Effect of Pressure Sensitive Paint On Aerodynamic Data", *AIAA Paper* 2003-3951, June 2003.

2. "Aviation Occurrence Report, Arrow Air Inc., Douglas DC-8-63 N950JW, Gander International Airport, Newfoundland, 12 December 1985," *Canadian Aviation Safety Board Report Number 85-H50902*, published 28 October 1988.

3. Barlow, J.B., Rae, W.H., Pope, A., *Low-Speed Wing Tunnel Testing, Third Edition*, John Wiley and Sons, 1999.

4. Bell, J.H., "Applications of Pressure-Sensitive Paint to Testing at Very Low Flow Speeds", *AIAA Paper* 2004-0878, January 2004.

5. Bell, J.H., Schairer, E.T., Hand, L.A., and Mehta, R., "Surface Pressure Measurements Using Luminescent Coatings", *Annual Review of Fluid Mechanics*, 2001, Vol. 33, pp. 155-206.

6. Bjorge, Scott T., *Flow Around an Object Projected from a Cavity into a Supersonic Freestream*, MS Thesis, AFIT/GAE/ENY/04-M02, Department of Aeronautics and Astronautics, Air Force Institute of Technology (AU), Wright Patterson AFB, OH, March 2004.

7. Cooper, K.G., *Rapid Prototyping Technology: Selection and Application*, Marcel Dekker Inc., New York, 2001.

8. Crafton, Jim W., Innovative Scientific Solutions, Incorporated, Personal Correspondence.

9. Crites, R.C., "Measurement Techniques: Pressure Sensitive Paint Technique," *von Karman Institute for Fluid Dynamic,* Lecture Series 1995-01.

10. DeLuca, Anthony M., *Experimental Investigation into the Aerodynamic Performance of Both Rigid and Flexible Wing Structured Micro-Air-Vehicles*, MS Thesis, AFIT/GAE/ENY/04-M06, Department of Aeronautics and Astronautics, Air Force Institute of Technology (AU), Wright Patterson AFB, OH, March 2004.

11. Grismer, M.J., Strang, W.Z., Tomaro, R.F., Witzeman, F.C., "Cobalt: A Parallel, Implicit, Unstructured Euler/Navier-Stokes Solver", *Advances in Engineering Software*, Vol. 29, No. 3-6, 1998, pp.365-373.

12. Innovative Scientific Solutions Inc., "Binary Pressure Sensitive Paint", *Product Information Guide*, September 2004.

13. Katz, J., Byrne, S., "Stall Resistance Features of Lifting-Body Aircraft", AIAA Journal of Aircraft Vol. 36, No. 2, March-April 1999.

14. Kimberlin, Ralph D., *Flight Testing of Fixed Wing Aircraft,* American Institute of Aeronautics and Astronautics, Inc., 2003, p. 44.

15. Lakowicz, J., *Principles of Fluorescence Spectroscopy*, Plenum Press, New York, 1983.

16. Leibeck, R.H., "Blended Wing Body Design Challenges", *AIAA Paper* 2003-2659, July 2003.

17. Miklosovic, D.S., Schultz, M.P., Esquivel, C., "Effects of Surface Finish on Aerodynamic Performance of a Sailboat Centerboard", *AIAA Journal of Aircraft*, Vol. 41, No. 5, September-October 2004.

18. Nelson, Robert C., Flight *Stability and Automatic Control, Second Edition*, McGraw-Hill Companies, Inc., 1998, pp. 42-95.

19. "Bi-Luminophore," ISSI Company website, 27 January 2005 http://www.innssi.com/BiLuminophoe.htm.

20. "A More Detailed Description of PSP Technology," ISSI Company website, 27 January 2005, http://innssi.com/DetailedPSP.htm.

21. Qin, N., Vavalle, A., Le Moigne, A., Laban, M., Hackett, K., Weinerfelt, P., "Aerodynamic Studies for Blended Wing Body Aircraft", *AIAA Paper* 2002-5448, September 2002.

22. Radeztsky, R.H., Reibert, M.S., Saric, W.S., "Effect of Isolated Micron-Sized Roughness on Transition in Swept Wing Flows", *AIAA Journal*, Vol. 37, No. 11, November 1999, pp. 1370-1377.

23. Schairer, E.T., Metra, R.D., Olsen, M.E., "Effects of Pressure-Sensitive Paint on Experimentally Measured Wing Forces and Pressures", *AIAA Journal*, Vol 40, No. 9, September 2002.

24. Schlichting, Herman, *Boundary-Layer Theory, Seventh Edition*, McGraw-Hill Publishing, 1979, pp 657-665.

25. "Selective Laser Sintering", *Castle Island's Worldwide Guide to Rapid Prototyping*, September 28, 2004, http://home.att.net/~castleisland/sls.htm.

26. Tyler, Charles, "A Joint Computational Fluid Dynamics and Experimental Fluid Dynamics Test Program", *AIAA Paper* 2004-0877, January 2004.

27. Tyler, C., Reeder, M.F., Braisted, W., Higgins, J., Gebbie, D.A., "Rapid Technology Focused Experimental and Computational Aerodynamic Investigation of a Strike Tanker", *AIAA Paper* 2004-6870, November 2004.

28. Tyler, C., Braisted, W., Higgins, J., "Evaluation of Rapid Prototyping Technologies for Use in Wind Tunnel Testing", *AIAA Paper* 2005-1301, January 2005.

29. Vanhoutte, F.G., Ashill, P.R., Gary, K.P., "Intrusion Effects of Pressure Sensitive Paint in Wind-tunnel Tests on Wings", *AIAA Paper* 2000-2525, June 2000.

Vita

     David Alan Gebbie was born in Columbus, Ohio. He was raised in Nashport, Ohio and graduated from Tri-Valley High School in Dresden, Ohio in 1999. He then received an Air Force ROTC scholarship to attend Ohio Northern University in Ada, Ohio. He graduated with a Bachelor of Science in Mechanical Engineering with Distinction in 2003. Upon his commissioning into the Air Force David was assigned to the Graduate School of Engineering and Management, Air Force Institute of Technology, Wright-Patterson AFB, OH. David spends his free time playing sports, restoring old cars, and making furniture. He is also and Eagle Scout.

REPORT DOCUMENTATION PAGE

The public reporting burden for this collection of information is estimated to average 1 hour per response, including the time for reviewing instructions, searching existing data sources, gathering and maintaining the data needed, and completing and reviewing the collection of information. Send comments regarding this burden estimate or any other aspect of the collection of information, including suggestions for reducing this burden to Department of Defense, Washington Headquarters Services, Directorate for Information Operations and Reports (0704-0188), 1215 Jefferson Davis Highway, Suite 1204, Arlington, VA 22202-4302. Respondents should be aware that notwithstanding any other provision of law, no person shall be subject to an penalty for failing to comply with a collection of information if it does not display a currently valid OMB control number.
PLEASE DO NOT RETURN YOUR FORM TO THE ABOVE ADDRESS.

1. REPORT DATE (DD-MM-YYYY)	2. REPORT TYPE	3. DATES COVERED (From – To)
11-03-2005	Master's Thesis	August 2003– March 2005

4. TITLE AND SUBTITLE

EXPERIMENTAL STUDY OF THE SUBSONIC AERODYNAMICS OF A BLENDED WING BODY AIR VEHICLE WITH A FOCUS ON RAPID TECHNOLOGY ASSESSMENT

5a. CONTRACT NUMBER

5b. GRANT NUMBER

5c. PROGRAM ELEMENT NUMBER

6. AUTHOR(S)

Gebbie, David A., Second Lieutenant, USAF

5d. PROJECT NUMBER
2003-115

5e. TASK NUMBER

5f. WORK UNIT NUMBER

7. PERFORMING ORGANIZATION NAMES(S) AND ADDRESS(S)

Air Force Institute of Technology
Graduate School of Engineering and Management (AFIT/EN)
2950 Hobson Way, Building 640
WPAFB OH 45433-8865

8. PERFORMING ORGANIZATION REPORT NUMBER

AFIT/GAE/ENY/05-M09

9. SPONSORING/MONITORING AGENCY NAME(S) AND ADDRESS(ES)

Air Force Research Laboratory/Air Vehicles Directorate
Attn: Dr. Charles Tyler
2210 8th Street, Building 146
WPAFB, OH 45433

10. SPONSOR/MONITOR'S ACRONYM(S)
AFRL/VA

11. SPONSOR/MONITOR'S REPORT NUMBER(S)

12. DISTRIBUTION/AVAILABILITY STATEMENT

APPROVED FOR PUBLIC RELEASE; DISTRIBUTION UNLIMITED.

13. SUPPLEMENTARY NOTES

14. ABSTRACT

The subsonic aerodynamic performance of a blended wing body aircraft constructed using selective laser sintering was assessed in the AFIT low-speed wind tunnel. The scaled-down model of a strike tanker aircraft consisted of a shaped fuselage and sweptback wings. The Reynolds number, based on mean wing chord, during testing was on the order of 10^5 while the Mach number ranged from 0.10 to 0.20. The model evaluation and analysis process included force and moment measurements acquired from a wind tunnel balance, pressure data measured with 8 taps located on the model's upper surface, a comparison to computational fluid dynamics (CFD) solutions acquired in a parallel study conducted by AFRL/VAAC, and global pressure sensitive paint (PSP) measurements. Paint measurements were compared to pressure tap data to ensure their accuracy while lift and drag coefficients, as well as pitching and rolling moments were examined to determine performance characteristics, including stability attributes and aircraft stall.

One of the most interesting results was the striking difference in the force and moment measurements before and after the paint was applied to the surface. The average surface roughness, Ra, was measured with a profilometer and was found to have increased from approximately 0.3μm to 0.7μm when the paint was applied. When traditional 2-D boundary layer approaches to assessing the effect of roughness, the 0.7μm value falls well below the threshold at which one would anticipate roughness to have any effect. There is support in archival literature for the notion that roughness effects are more pronounced in a 3-D boundary layer, and the pitching moment data and the PSP data indicate that the for the painted model, there is a gradual onset of wing stall marching inward from the wingtips toward the body. By contrast, the force and, in particular, the pitching moment data suggests that the onset of wing stall is sudden across the entire wing for the unpainted case. Interestingly, the CFD data compared well with the data corresponding to the measurements of the rougher, painted model. Notably, the grid used in CFD would require at least an order of magnitude higher resolution in the boundary layer region to accurately depict the submicron roughness effects.

15. SUBJECT TERMS

Pressure Sensitive Paint, Rapid Prototyping, Surface Roughness, Blended Wing Body,

16. SECURITY CLASSIFICATION OF: UNCLASSIFIED			17. LIMITATION OF ABSTRACT	18. NUMBER OF PAGES	19a. NAME OF RESPONSIBLE PERSON
a. REPORT	b. ABSTRACT	c. THIS PAGE			Dr. Mark F. Reeder
U	U	U	UU	157	19b. TELEPHONE NUMBER (Include area code) (937) 255-3636, ext 4530 (mark.reeder@afit.edu)